Adjustment of RapidScat Backscatter Measurements for Improved Radar Images

Garrett Scott McDonald

A thesis submitted to the faculty of
Brigham Young University
in partial fulfillment of the requirements for the degree of

Master of Science

David G. Long, Chair
Brian A. Mazzeo
Cameron K. Peterson

Department of Electrical and Computer Engineering

Brigham Young University

ABSTRACT

Adjustment of RapidScat Backscatter Measurements for Improved Radar Images

Garrett Scott McDonald
Department of Electrical and Computer Engineering, BYU
Master of Science

RapidScat is a spaceborne wind scatterometer mounted on the International Space Station (ISS). The RapidScat mission lasted from September 2014 to November 2016. RapidScat enables the measurement of diurnal patterns of σ^0 measurements. This capability is possible because of the non-sun-synchronous orbit of the ISS, in which the local time of day (LTOD) of σ^0 measurements gradually shifts over time in any given location. The ISS platform is a relatively unstable platform for wind scatterometers. Because of the varying attitude of the ISS, RapidScat experiences a constant variation of its pointing vector. Variations of the pointing vector cause variations in the incidence angle of the measurement on the ground, which has a direct effect on σ^0 measurements.

In order to mitigate σ^0 variations caused by incidence angle and LTOD, the dependence of σ^0 on these parameters is modeled in order to enable a normalization procedure for σ^0. These models of σ^0 dependence are determined in part by comparing RapidScat data with other active Ku-band instruments. The normalization procedure is designed to adjust the mean value of σ^0 to be constant across the full range of significant parameter values to match the mean of σ^0 at a particular nominal parameter value.

The normalization procedure is tested both in simulation and with real σ^0 measurements. The simulated normalization procedure is effective at modeling and removing σ^0 dependence on incidence angle and LTOD over a homogeneous region. The variance in simulated images is reduced by the normalization procedure. The normalization procedure also reduces variance in real backscatter images of the Amazon and an arbitrary region in East Africa.

Keywords: RapidScat, scatterometer, sigma-0, calibration, radar, image

ACKNOWLEDGMENTS

I would first like to acknowledge my wife, Johannah, for her continual support and encouragement. It was invaluable to have someone that believed in me when I doubted myself. Additionally, I express my appreciation to Dr. Long and the rest of my committee for helping me see beyond my own understanding. Special thanks to Samuel Bury for being a constant partner in success and failure throughout graduate school.

TABLE OF CONTENTS

LIST OF TABLES

LIST OF FIGURES

CHAPTER 1. INTRODUCTION

Spaceborne wind scatterometers are radars that measure the normalized radar cross-section of the earth's surface (represented by σ^0), which is directly proportional to the measured power of the radar backscatter from the surface. These scatterometers are specifically calibrated for estimating near-surface ocean wind vectors from σ^0 measurements (as seen in Fig. 1.1).

In addition to measuring ocean wind vectors, scatterometer data is used for a variety of land and ice applications. Some of these land and ice applications include estimating sea ice extent, measuring Greenland ice melt, and estimating volumetric soil moisture content (see Figs. 1.2 and 1.3) [2] [3] [4]. Scatterometer data is also related to general vegetation and landscape characteristics of the earth. The changes in these characteristics can be observed from year to year, which can reveal potential climate changes. Spaceborne scatterometers have global coverage in a short period of time (within a day or two), which enables the creation of global datasets of scatterometer measurements and related data products (see Fig. 1.4).

Many of these data products are made into images. Many such data products use the Scatterometer Image Reconstruction (SIR) image algorithm. SIR images are high-resolution radar backscatter images of land features [5]. Examples of these images can be seen in Figs. 1.2 and 1.4. The SIR algorithm increases radar image resolution by reconstruction of the σ^0 measurements using the antenna spatial response function (SRF). The SIR algorithm takes an iterative approach to a large matrix inverse. As iterations increase, resolution and noise error both increase. The SIR algorithm provides a good trade-off of resolution and error noise [6].

RapidScat is a spaceborne scatterometer that flew its mission from 2014 to 2016. This radar is mounted on the International Space Station (ISS) to provide additional scatterometer data in the Ku-band frequency band (see Fig. 1.5). This mission was launched during a time when other Ku-band scatterometers were either in development or a non-functioning state.

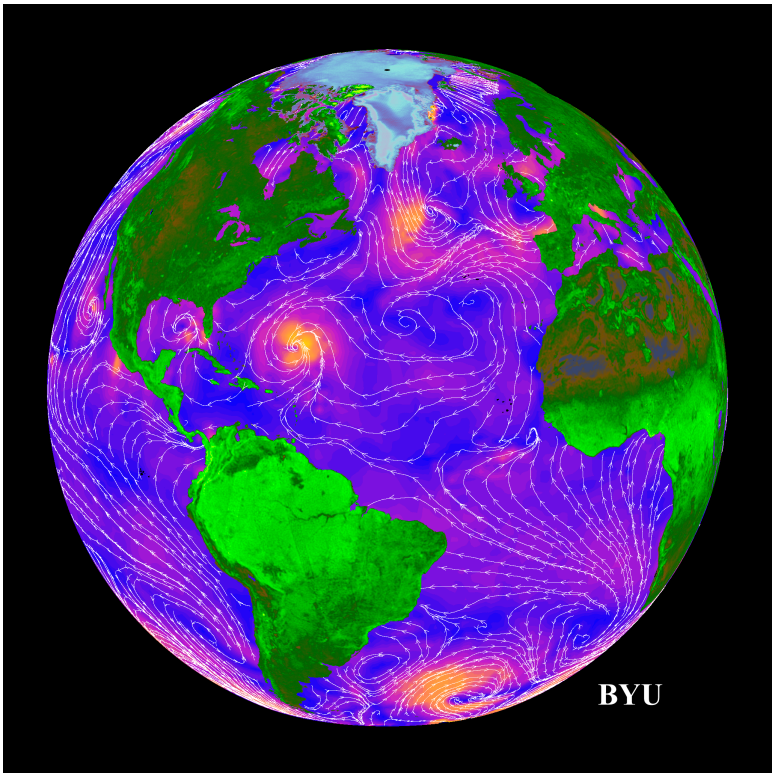

Figure 1.1: Rendering of global ocean wind vector measurements, as well as land backscatter measurements. This represents the primary application for spaceborne wind scatterometers. From the Brigham Young University (BYU) Microwave Earth Remote Sensing (MERS) group's scatterometer climate pathfinder (SCP) website [1].

In this thesis, a method is developed for improved calibration of RapidScat backscatter measurements (or σ^0) for the creation of radar backscatter images. The RapidScat scatterometer has already had basic validation and calibration tests done to test the consistency of its data measurements by comparing with the QuikSCAT scatterometer [8]. This report focuses on how to compensate for RapidScat attitude and orbital irregularities to reduce the variability of measurements for improved radar images. The estimated models of these factors also suggest a method for adjusting RapidScat measurements and other Ku-band radar measurements to a common mean, despite differences in local time of day and incidence angle. The adjustment of mean values in this way can improve the calibration of every dataset.

In this thesis, relevant background information is first introduced in Chapter 2. Next, the method for model estimation (Chapter 3) and the procedure for σ^0 adjustment are explained

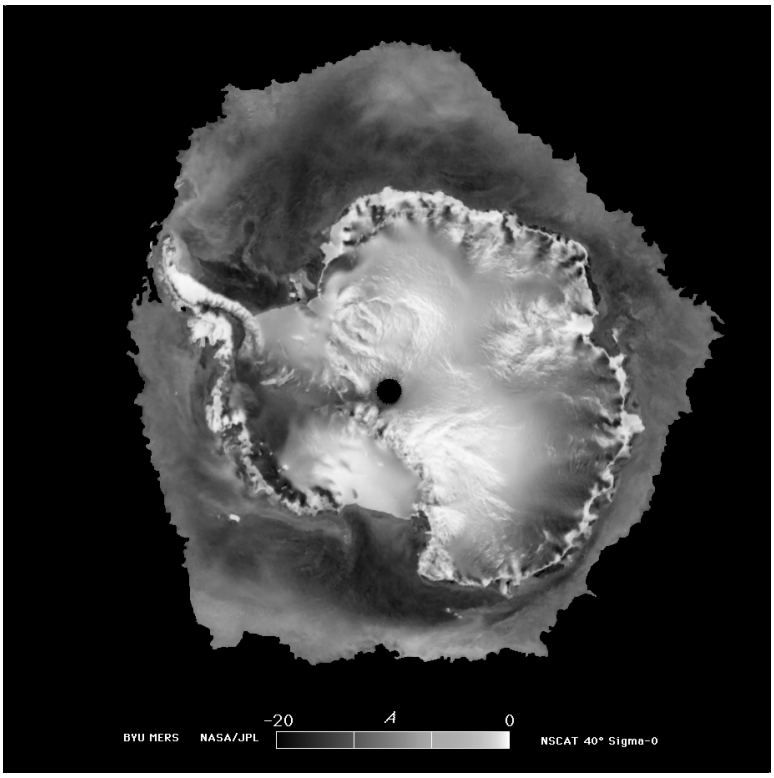

Figure 1.2: Masked SIR image of Antarctica using NSCAT data. This image shows land features and sea ice surrounding the continent (other land masses have been removed). An image like this can be used to estimate the area of sea ice and the changing extent over time. From the BYU SCP website [1].

(Chapter 4). Finally, the results of the adjustment procedure are examined by analyzing adjusted backscatter images (Chapter 5).

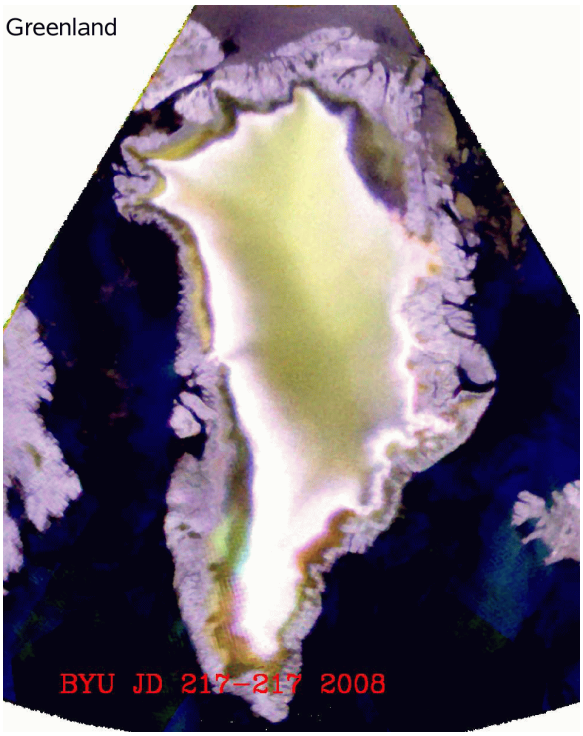

Figure 1.3: Combined SIR image of QuikSCAT and ASCAT data over Greenland. This image represents the results of both Ku-band and C-band measurements. Because of the unique properties of microwave pulses, properties of the Greenland snowpack can be inferred from this image. From the BYU SCP website [1].

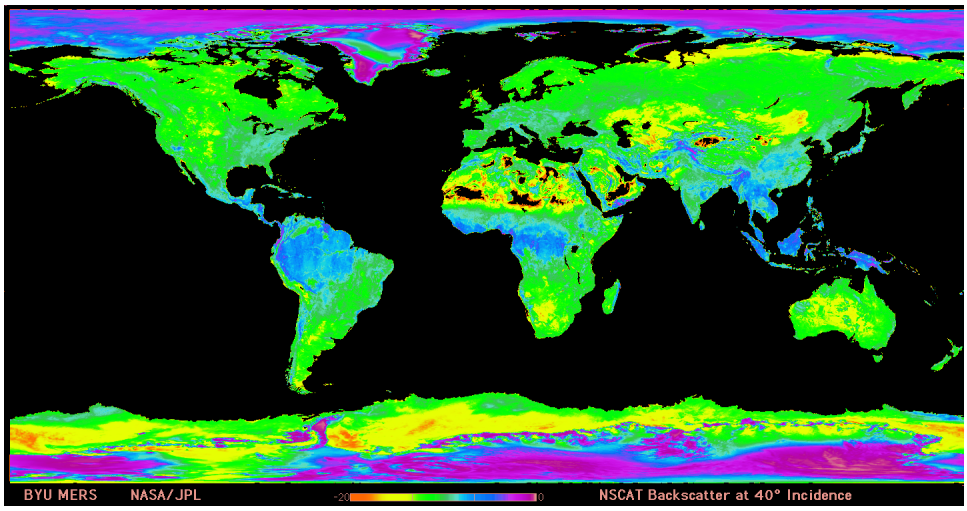

Figure 1.4: A global SIR image of NSCAT backscatter data, with ocean-only measurements masked out. Different backscatter values are correlated with various land characteristics. An image like this can be created after a few days of collecting data. From the BYU SCP website [1].

Figure 1.5: Artist's rendering of the RapidScat scatterometer on the *Columbus* module of the International Space Station (ISS). From JPL's RapidScat Mission website [7].

CHAPTER 2. BACKGROUND

Essential background information is presented in this chapter to explain the basics of microwave spaceborne scatterometry, and how those issues affect the RapidScat mission. The RapidScat mission and SIR images are introduced, and the purpose of σ^0 adjustment is explained.

2.1 Scatterometry

Spaceborne scatterometers observe σ^0, which is a measurement of the radar backscatter of the earth's surface. The σ^0 measurement is related to the power received by the radar equation. The power received is calculated as

$$P_r = \frac{P_t \lambda^2}{(4\pi)^3 L} \int_A \frac{G^2 \sigma^0}{R^4} dA. \tag{2.1}$$

The normalized radar cross-section σ^0 can then be estimated by the "X factor" method, where

$$\sigma^0 = \frac{P_r}{X}, \tag{2.2}$$

and where X is the "X factor," which is calculated as

$$X = \frac{P_t \lambda^2}{(4\pi)^3 L} \int_A \frac{G^2}{R^4} dA. \tag{2.3}$$

In the above equations, P_r is the power received, P_t is the transmitted power, λ is the wavelength of the radar pulses, G is the antenna gain, L is the system losses, R is the range to the earth's surface, and A is the area of the antenna beam footprint on the ground. Each of the values in the "X factor" (Eq. 2.3) is known or is estimated quite precisely, which makes the calculation of σ^0 by Eq. 2.2 feasible. The values of the X factor are pre-computed and stored in a lookup table. Errors caused by this calculation are not considered in this report. However, some of the basic assumptions for

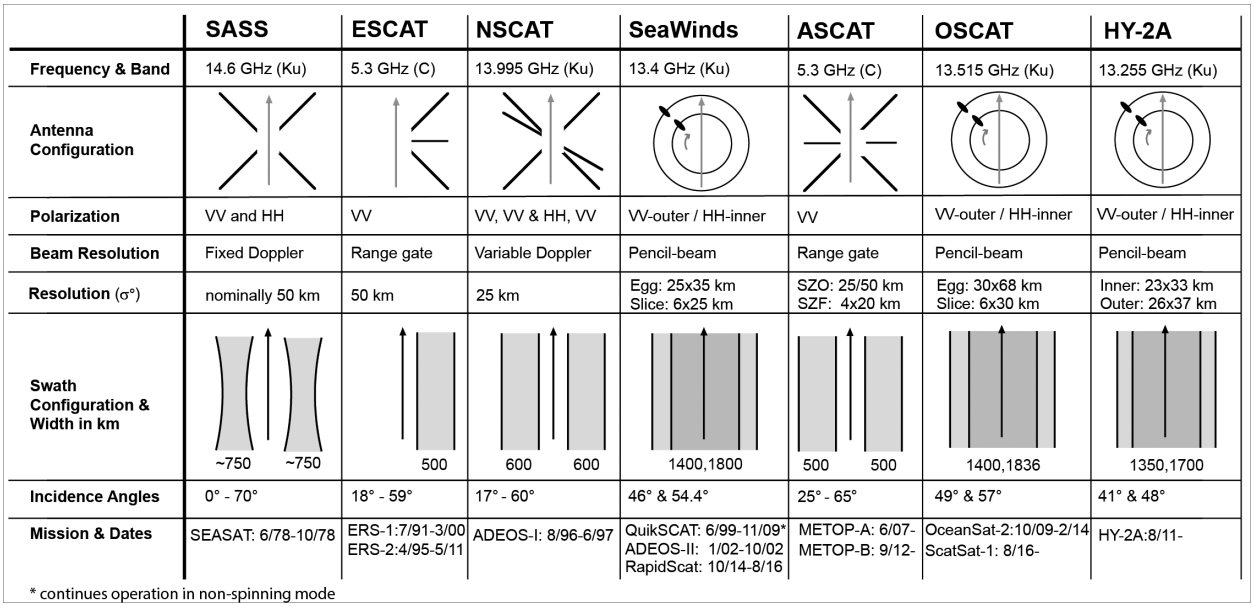

Figure 2.1: Compilation of spaceborne scatterometer missions since Seasat. From the BYU SCP website [1].

this X factor table calculation vary over time, due to changing altitude, attitude, and SNR states for the RapidScat instrument. These issues have been compensated for in previous analyses [9]. Thus, σ^0 is computed quite precisely. However, the observed σ^0 is also a function of the incidence angle and the surface characteristics. Additionally, some noise is present in σ^0 measurements from thermal noise of the receiver. The exact variations of σ^0 are uncertain, since they are caused by complex electromagnetic processes with many variables, including variables such as roughness of the surface and the viewing angle. In this thesis, variations of σ^0 caused by changes in incidence angle, local time of day (LTOD), and attitude changes are the principal parameters considered.

2.2 History of Scatterometry

Several spaceborne wind scatterometers have flown missions over the past few decades. These radars operate in either Ku-band or C-band frequencies. There are two main measurement configurations for these scatterometers: fan beams and scanning pencil beams. A summary of these scatterometers can be seen in Fig. 2.1 and Tables 2.1 and 2.2. See [10] for a detailed introduction to spaceborne radars and remote sensing.

Table 2.1: Fan Beam Scatterometer LTOD at Equator Crossing. The terms "Asc" and "Desc" refer to ascending and descending nodes, respectively.

Seasat	NSCAT	ASCAT-1/2	ERS-1/2
All	10 pm Asc	9:30 pm Asc	10/10:30pm Asc
	10 am Desc	9:30 am Desc	10/10:30am Desc

Table 2.2: Pencil Beam Scatterometer LTOD at Equator Crossing. The terms "Asc" and "Desc" refer to ascending and descending nodes, respectively. The term "Quik" refers to the QuikSCAT scatterometer and satellite.

SeaWinds/Quik	RapidScat	Oscat-1/2	TRMM
10pm/6am Asc	All	12 am Asc	All
10am/6pm Desc		12 pm Desc	

2.2.1 Fan Beam Scatterometers

Scatterometers with fan beams include the Seasat-A Satellite Scatterometer (SASS) on the Seasat-1 satellite, the NASA Scatterometer (NSCAT) on the ADEOS satellite, the Advanced Scatterometer (ASCAT) on the Metop-A satellite, ASCAT-2 on Metop-B, the AMI (in Wind Scatterometer Mode) on the ERS-1 satellite, and the AMI on ERS-2. SASS was the first spaceborne wind scatterometer to be tested by NASA. It helped to lay the groundwork for wind scatterometry by gathering σ^0 measurements from multiple azimuth angles. These measurements were colocated with *in situ* measurements made from buoys and other instruments, which enabled the creation of a geophysical model function (GMF) to correlate σ^0 measurements with wind speed and direction on the ocean. NSCAT followed SASS, and the low-noise measurements of NSCAT enabled a more accurate estimate of the GMF and ocean wind vectors across the globe. SASS and NSCAT are both Ku-band instruments. ASCAT-1 and -2, and ERS-1 and -2, are C-band instruments. The C-band scatterometers were built and designed by the European Space Agency (ESA) and were used to develop C-band GMFs.

NSCAT data is used as a primary reference in this thesis, since it provides low-noise σ^0 measurements across a large range of incidence angles. NSCAT measures the earth with six fan-beam antennas. Each fan beam antenna on NSCAT creates a long, thin footprint on the ground, each at a different azimuth angle (see Fig. 2.2). As the instrument orbits, the antenna beams

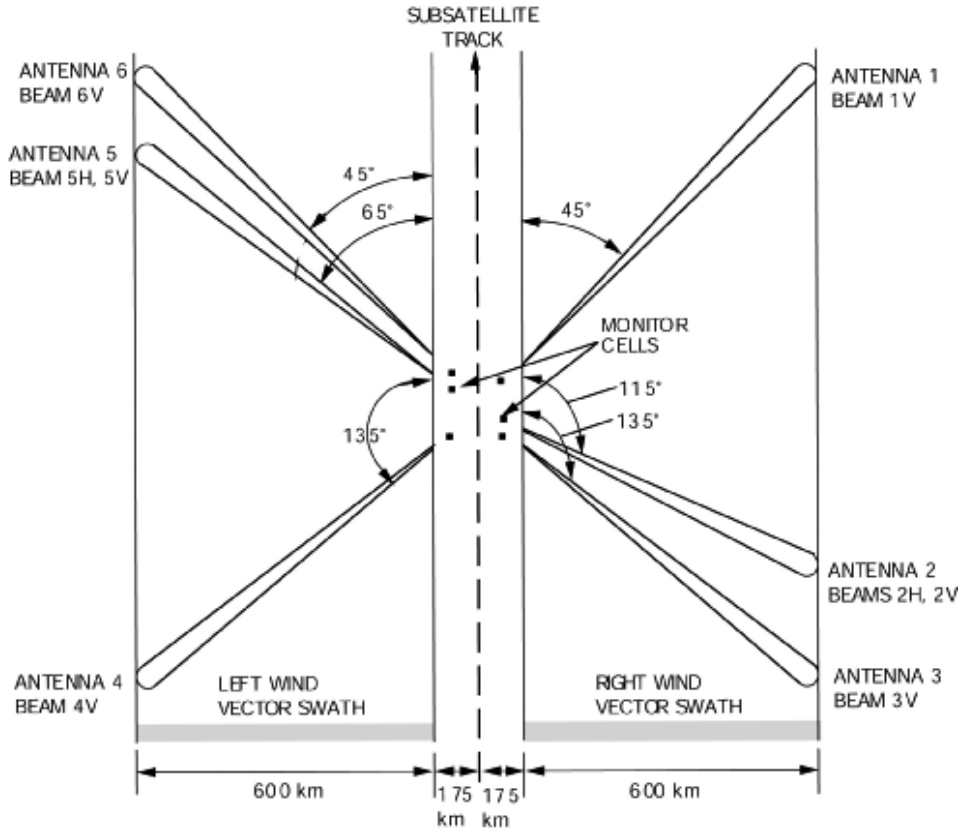

Figure 2.2: Fan beam measurement geometry for NSCAT. Because of wide beamwidths, the backscatter measurements span a large range of incidence angles, as seen in Fig. 2.4. Figure taken from Graf, et al [11].

measure over two swaths around the orbital track of the satellite, with a null measurement space in the nadir part of the swath. The antenna pattern is illustrated for NSCAT in Fig. 2.2.

2.2.2 Pencil Beam Scatterometers

Scatterometers with pencil beams include the SeaWinds instrument on the ADEOS-II satellite (known as SeaWinds), the SeaWinds instrument on the QuikSCAT satellite (known as QuikSCAT), the SeaWinds instrument on the International Space Station (known as RapidScat), the SCAT instrument on the Oceansat-2 satellite (Oscat), and Oscat-2 on the SCATSAT-1 satellite (Oscat-2). Additionally, the Chinese launched a scatterometer called HY-2A, but its data was not accessible for this thesis. These instruments are all Ku-band scatterometers.

Although it is not designed to be a scatterometer, the precipitation radar (PR) on the Tropical Rainfall Measuring Mission (TRMM) satellite is another Ku-band instrument that measures σ^0 with a scanning pencil beam. The TRMM PR is designed for 3-D precipitation mapping, and its pencil beam is electronically scanned using a phased-array antenna. The PR reports a near-surface σ_0 value that is comparable to scatterometer measurements, although the incidence angle of measurements is much lower, creating higher σ^0 measurements than Ku-band scatterometers. For simplicity, the TRMM PR dataset is referred to as TRMM for future sections of this thesis.

The data from many of these pencil beam instruments are considered in this thesis, since they all have similar operating frequencies and antenna configurations. Each of the SeaWinds scatterometers (QuikSCAT, SeaWinds, and RapidScat) have very similar hardware, with only minor modifications to RapidScat, in order for it to function on the International Space Station (ISS), at a different altitude than the other SeaWinds scatterometers. Oscat also has a rotating beam, but it functions at different incidence angles than the SeaWinds instruments, and it has differing signal processing hardware. Most of these scatterometers and radars orbit in a sun-synchronous orbit. RapidScat and TRMM do not, however. For both of these instruments, their lower-inclination orbits are not sun-synchronous and global coverage is not possible.

Because of its long mission life and low-noise backscatter measurements, QuikSCAT's dataset has become the standard for pencil-beam scatterometer calibration. QuikSCAT completed a mission of 10 years. QuikSCAT orbits close to 800 km above the geoid and measures over nearly every geophysical location. It has a sun-synchronous orbit, so it achieves over 90 percent global coverage each day and 97 percent coverage in 2 days, and it crosses the equator at approximately the same local time of day (LTOD), separated by 12-hour intervals. It has a 1,800-kilometer-wide beam swath.

2.3 Scatterometer Calibration

To improve the precision of σ^0 measurements, each scatterometer is calibrated to be consistent with *in situ* measurements and other scatterometers. Only scatterometers that emit in the same frequency band are used for this comparison.

In order to calibrate all scatterometer measurements to have similar mean values at every location on the earth, σ^0 values must be adjusted to appear to be effectively at the same incidence

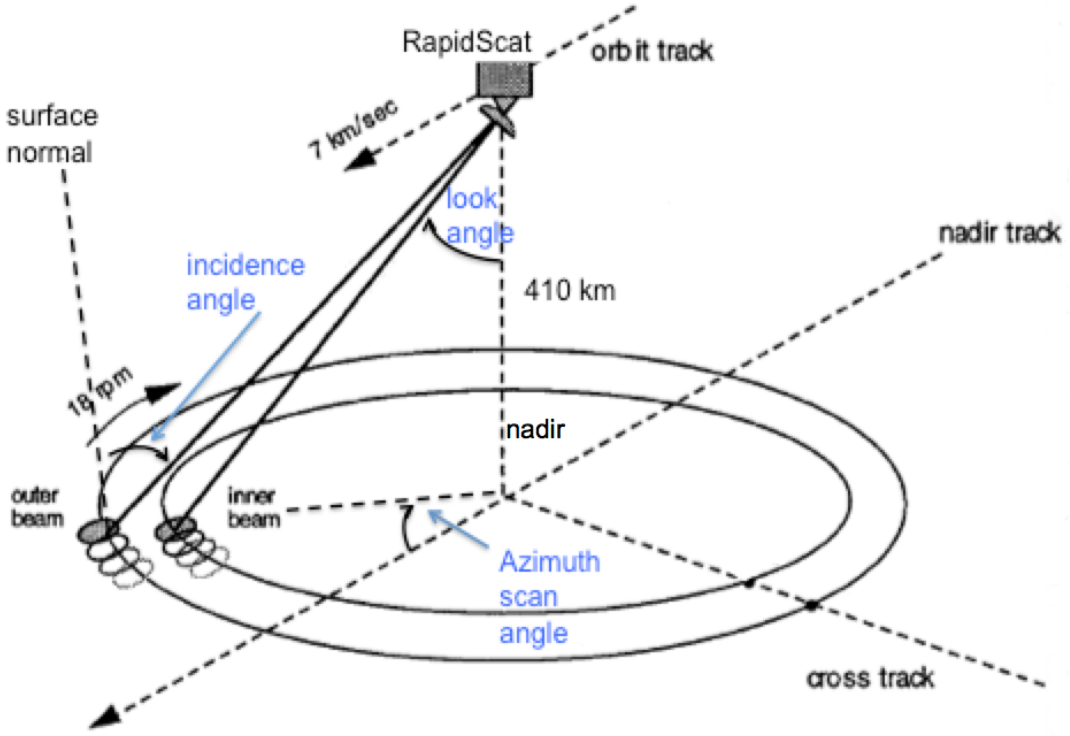

Figure 2.3: Pencil-beam measurement geometry for RapidScat. Note that incidence angle is related to the surface normal vector of the earth. From JPL's RapidScat mission website, with alterations [7].

angle and LTOD values. This adjustment of values according to incidence angle and LTOD can only be done through modeling σ^0 dependence on these parameters.

2.4 Incidence Angle Effects on σ^0

One significant parameter affecting σ^0 is incidence angle, which is the angle between the radar boresight and the surface normal vector of the earth (see Fig. 2.3). Backscatter measurements have a generally decreasing value as incidence angle increases, which can be seen in measurements made by NSCAT in Fig. 2.4. Fig. 2.5 shows the general relationship expected for σ^0 dependence on incidence angle changes, showing how the dependence is altered for different surface characteristics.

An example of incidence angle variation can be seen with fan beam scatterometers, such as NSCAT (see Fig. 2.4). Throughout its mission life, NSCAT backscatter measurements exhibited an

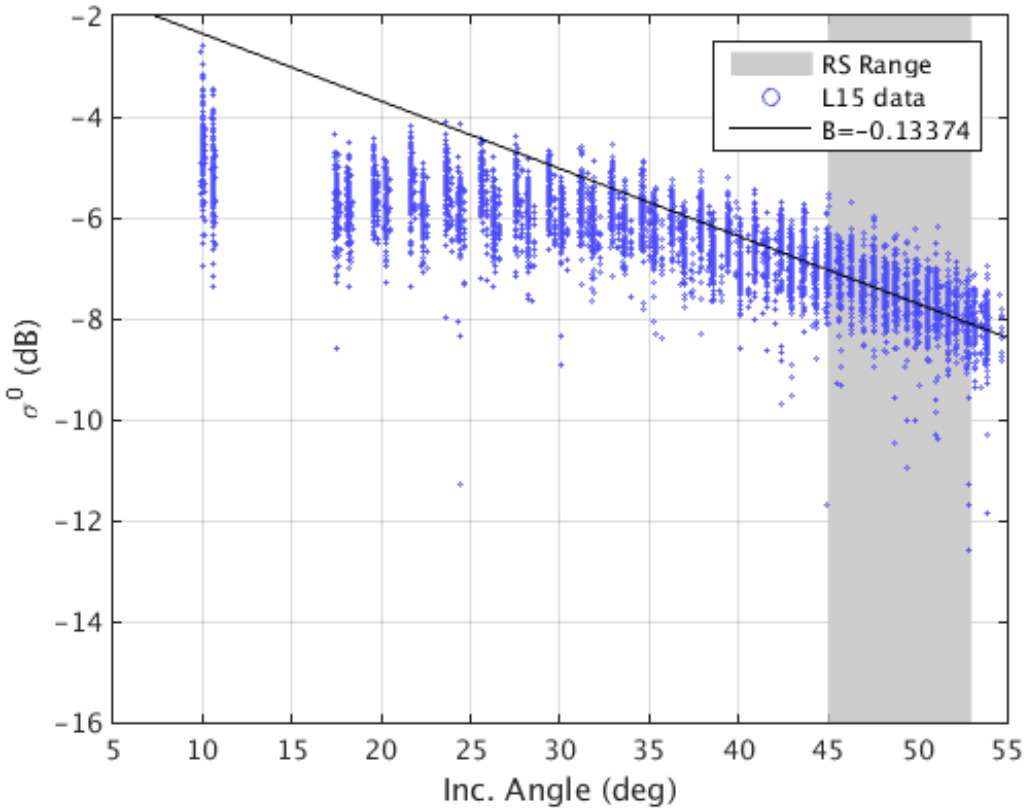

Figure 2.4: Plot of σ^0 versus incidence angle for NSCAT data over the Amazon, using ascending nodes. Note that NSCAT shows a slope of -0.13 dB/deg (represented by the letter "B") over the same incidence angle range that RapidScat spans (indicated in grey over the range of 45–53°). The fit line shown is a least-squares fit to the NSCAT data in this range.

average slope of σ^0 dependence on incidence angle that is close to -0.13 dB/deg over the Amazon across the range of incidence angles measured by RapidScat.

Incidence angle effects on σ^0 are not as prominent for pencil beam scatterometers as they are for fan beam scatterometers. This is because pencil beam scatterometers have a very narrow beamwidth, so they typically cover only a narrow incidence angle range. QuikSCAT is a pencil beam scatterometer, with beamwidths of 1.6 and 1.4 degrees for the inner and outer beams, respectively, as well as a very small change in incidence angle values over its mission life. RapidScat exhibits a much larger incidence angle range, close to a range of 45–53°.

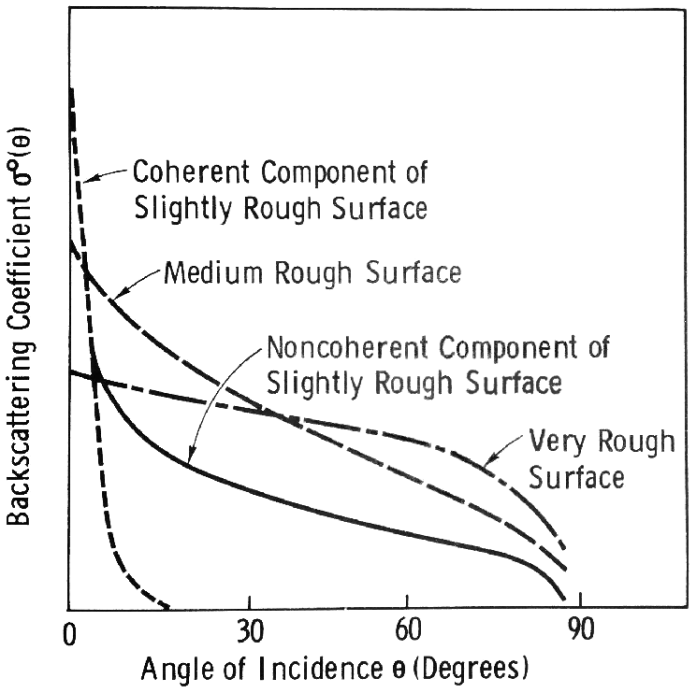

Figure 2.5: Microwave radar incidence angle dependence for different surface characteristics. This figure shows general relationships of σ^0 with incidence angle in dB space. The dependence shown by NSCAT in Fig. 2.4 is very similar to the curve labeled "very rough surface," since the Amazon rainforest appears very "rough" in the Ku-band frequency range, largely due to volume scattering. From Ulaby et al., 1982 [12].

2.5 Local Time of Day Effects on σ^0

Local time of day (LTOD) can influence σ^0 variations significantly, due to changes in electromagnetic properties of vegetation throughout the day. Over the Amazon, it is postulated that this peak at 6am is caused by dew formation on the leaves of jungle vegetation, since water is the most significant electromagnetic scatterer in vegetation in the microwave frequencies [13]. RapidScat is the first Ku-band scatterometer to take measurements of the same location over a range of local times. This span of LTOD in measurements is because RapidScat is in a non-sun-synchronous orbit, unlike QuikSCAT and NSCAT. RapidScat data shows that σ^0 variations from LTOD can be significant and that they are coupled with σ^0 variations from incidence angle.

Fig. 2.6 shows the average daily changes for σ^0 over the Amazon. This figure is a plot of measurements from the first five months (the Amazon wet season) of RapidScat data in 2015.

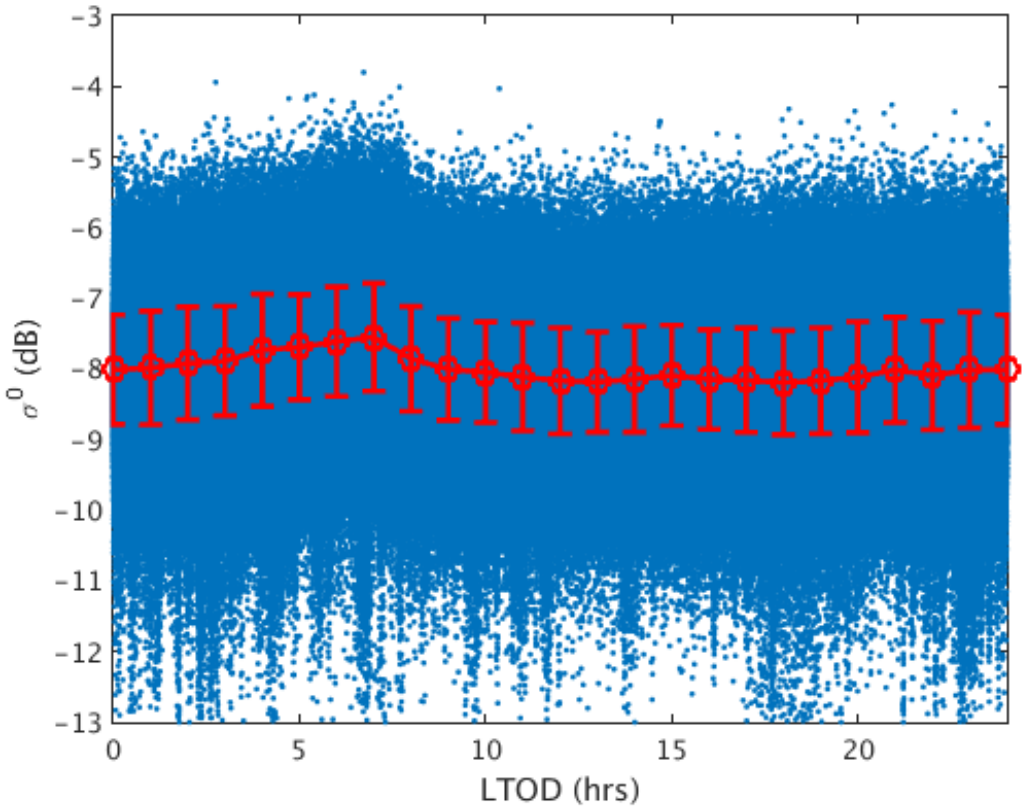

Figure 2.6: Scatter plot of σ^0 variation over 24 hours of LTOD, as observed by RapidScat. The mean and standard deviation is shown for each hour. Includes all data from the inner beam over the Amazon mask, day 1–151, 2015. Mean is represented by circles, and standard deviation is represented by horizontal bars. Note the distinct increase in backscatter values between 5 and 10 am.

Only the first five months of data are used in order to avoid seasonal effects. Note that the mean σ^0 value changes cyclically over the day on average, most notably in the morning, close to 6 am. A sinusoidal model with a period of 24 hours is necessary to model such behavior. However, the gradual nature of the changes in the mean σ^0 across the range of LTOD values (see Fig. 2.6) suggests that σ^0 measurements over a few hours (2–4 hours) of LTOD can be modeled as a first-order polynomial or a second-order polynomial, rather than a sinusoid.

2.6 Compensation for σ^0 Variation

In order to combine RapidScat backscatter measurements for a radar backscatter image at a fixed incidence angle, changes to σ^0 values caused by radar pointing and LTOD variation must be compensated for. To do this compensation, RapidScat σ^0 dependency on significant parameters is modeled.

To make radar images from fan beam scatterometer data, backscatter changes caused by incidence angle variations are compensated for. This compensation is necessary because fan beams have a very large beamwidth, and so they measure over a large range of incidence angles (see Fig. 2.2 and 2.4). This span of incidence angles occurs for every measurement. Incidence angle effects on σ^0 can be readily modeled and compensated for precisely with fan beam data because every antenna measurement is taken over a large range of incidence angles.

In this thesis, σ^0 dependence on incidence is plotted for RapidScat data over the Amazon, and a similar relationship is observed. Because a similar pattern is observed (over a smaller incidence angle range), a similar compensation procedure that used for fan beams can be applied to RapidScat. For RapidScat data, however, plotting measurements of σ^0 across a significant range of incidence angles requires multiple measurements. This means that modeling σ^0 dependence on incidence angle requires many more data points to be estimated accurately. The dependence of backscatter values on incidence angle is analyzed for several Ku-band scatterometers and RapidScat in order to create a model and then adjust the σ^0 values.

2.7 SIR Images

The Scatterometer Image Reconstruction (SIR) image algorithm enables the creation of enhanced-resolution backscatter images of the earth. The SIR algorithm assumes that measurements in the same geographic location are not affected by changes in radar pointing or the local time of day (LTOD). When these assumptions are violated, the error in the image increases. Because RapidScat data varies with radar pointing and LTOD, σ^0 dependence on these parameters is normalized to be constant across the full range of these parameter values.

2.8 RapidScat Mission

The RapidScat mission lasted from September 2014 to August 2016. It was designed to be a rapid replacement to the QuikSCAT scatterometer, which stopped functioning properly in 2009. The RapidScat mission enables the continuation of the Ku-band scatterometer dataset. Development for RapidScat began in 2012 and was completed in 2014. This rapid production timeline was enabled by retrofitting the QuikSCAT engineering model with additional commercial parts to meet the specific needs of the RapidScat mission.

RapidScat is installed on the *Columbus* module of the International Space Station (ISS), instead of a dedicated satellite platform (see Fig. 2.7). Using the ISS platform reduces many of the usual manufacturing and launch costs of a spaceborne scatterometer mission. Though not an ideal platform for an active radar instrument, the RapidScat mission continues the valuable dataset created by QuikSCAT and other Ku-band scatterometer data. Additionally, the non-sun-synchronous orbit of the ISS enable measurements from various LTODs, which is new data that was not previously available for Ku-band scatterometers.

2.8.1 Orbital Variations

RapidScat has an inclined equatorial non-sun-synchronous orbit, so the measurements are taken at varying LTODs as the orbit precesses over time. The ISS orbit only passes locations between 51.6 degrees North and South, and RapidScat observes each location at a slightly different LTOD as the orbit precesses. Full coverage of the complete orbit is accomplished within 40 hours. A full 24 hours of LTOD measurements are measured over a time period of 2 months [7]. Using RapidScat measurements from a range of LTODs enables diurnal cycles for scatterometer measurements to be characterized. However, this also means that σ^0 measurements change slightly every day in the same location, which introduces noise into radar images.

2.8.2 Attitude Variations

The ISS is an unusual platform for a spaceborne scatterometer. Most spaceborne scatterometers are mounted on a satellite platform dedicated for radars and other scientific instruments. RapidScat suffers from measurement errors because of the ISS platform. The pitch, roll, and yaw

Figure 2.7: The RapidScat scatterometer on the *Columbus* module of the International Space Station (ISS). RapidScat was launched to replace the QuikSCAT mission. Image courtesy of NASA [7].

of the space station constantly change throughout each orbit by a few fractions of a degree, which causes variations in the measurement incidence angle as the radar antenna rotates. RapidScat has a much larger incidence angle variation than other pencil beam scatterometers like QuikSCAT because of the attitude variations of the ISS. The variation in incidence angle requires adjustment of σ^0 values for the creation of low-noise SIR images.

2.8.3 Analysis of Attitude Changes

To demonstrate how incidence angle values change throughout each orbit, data from four arbitrarily-chosen and consecutive orbital revolutions of RapidScat are considered (from day 305, 2014). The data from these revolutions are typical of data throughout the mission. The data show a distinct periodic variation in incidence angle values as the antenna rotates, as seen in Fig. 2.8. Because the incidence angle values are so directly correlated with the rotation of the antenna, it

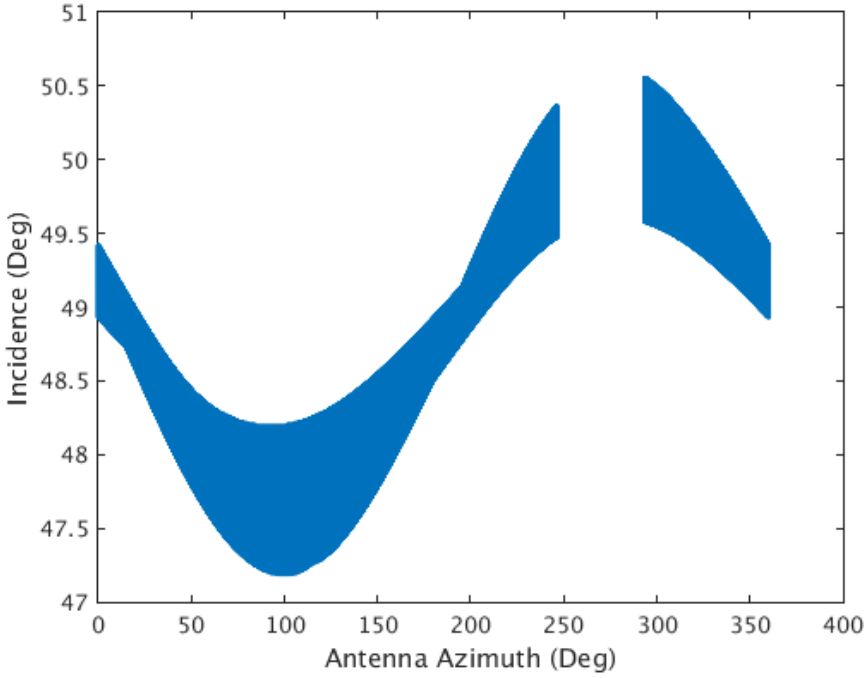

Figure 2.8: Plot of incidence angle versus antenna rotation angle for RapidScat (scatter plot). Note the spread of values as the antenna rotates. This represents all the incidence angle values within four orbital revolutions around the earth, with no time correlation. This plot suggests a non-nadir pointing angle for the spacecraft. RapidScat stops emitting for the gap in azimuth angle values (called sector blanking) in order to avoid damaging an ISS solar panel.

appears that the attitude of the spacecraft is the dominant cause of the incidence angle variation. The variation of incidence angle because of antenna rotation suggests that the ISS is maintaining a non-nadir pointing angle. The effect of attitude changes can be seen in Fig. 2.9, which shows a direct correlation between the reported roll values of the instrument and the range of variation in incidence angle. Because of these results, attitude is assumed to be the principal effect on incidence angle values in this thesis.

In the next chapter, models for normalizing σ^0 variations are considered. RapidScat σ^0 measurements are used to estimate models of σ^0 dependence on various parameters. These models are used in Chapter 4 to adjust simulated σ^0 values and show the effect of adjusting σ^0 on SIR image quality.

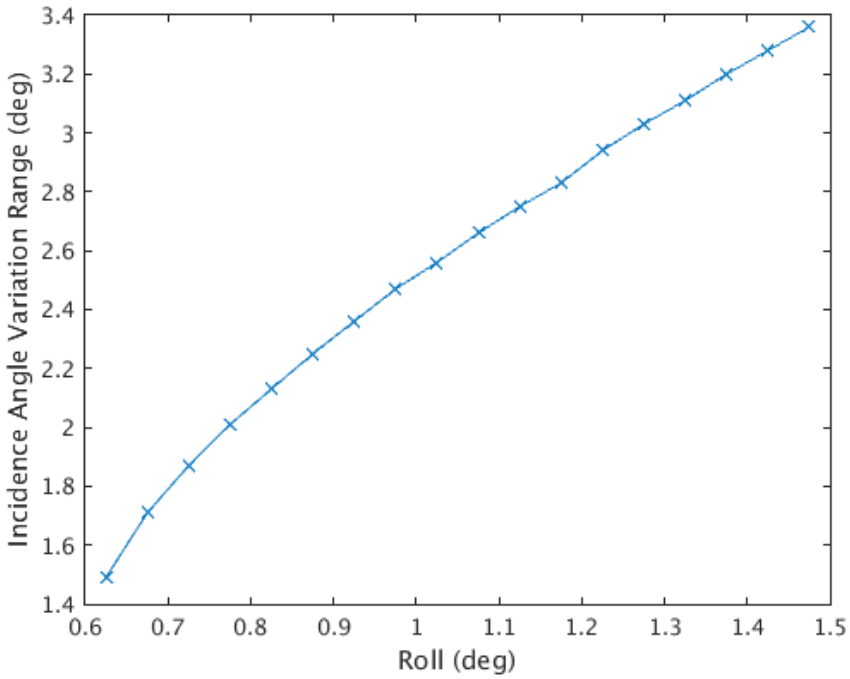

Figure 2.9: Plot of the range of incidence angle variation compared to the ISS roll angle. Note that as the roll angle increases, the variation in incidence angle also increases. Each value (marked by an "X") was calculated by binning the incidence angle data into 0.05 degree roll angle bins and then subtracting the minimum incidence angle value from the maximum incidence angle value.

CHAPTER 3. MODEL DEVELOPMENT

The goal for adjusting RapidScat σ^0 measurements is to compensate for undesired variations of σ^0 caused by several parameters, such as incidence angle and spacecraft attitude. Undesired variation in σ^0 is compensated for by a normalization procedure, where the dependence of σ^0 on each significant parameter is adjusted to yield a single, constant mean across the full range of the parameter values. This normalization procedure can improve SIR image quality. In order to do this normalization procedure, RapidScat σ^0 dependence on significant parameters is modeled.

In this chapter, RapidScat σ^0 dependence on each significant parameter is modeled. In order to do this, the parameters that are considered significant to σ^0 variation are first determined by considering the peculiarities of the RapidScat mission compared to previous sensors. Next, model structure is determined by comparing RapidScat measurements with multiple Ku-band instruments. Finally, model coefficients are estimated by a least-squares method. Models for σ^0 dependence on incidence angle and LTOD are used to normalize dependence on each parameter in Chapters 4 and 5. In addition, models for roll angle, pitch angle, and azimuth angle are used to measure the effectiveness of σ^0 adjustments for RapidScat. Simulations are used to demonstrate the validity of this approach in Chapter 4, and the procedure is applied to real RapidScat data to make SIR images in Chapter 5.

3.1 Significant Parameters

As mentioned in Chapter 2, a significant issue for RapidScat is its spacecraft platform, the International Space Station (ISS). The ISS has a variable attitude and altitude, and the orbit is not sun-synchronous. Attitude variations cause changes in incidence angle, and orbit precession causes changes in the local time of day (LTOD) for each σ^0 measurement. For a sun-synchronous orbit, measurements in a specific location happen only at one local time for an ascending or descending pass, respectively. Because of the non-sun-synchronous orbit of the ISS, RapidScat measures any

location at multiple varying local times, as the orbit precesses. RapidScat measurements span a full 24 hours of local time over the course of 2 months in any specific location.

Historically, the platform attitude has been stable for pencil-beam scatterometers, which means the measurements are measured at a single incidence angle per beam, with minimal variation. For RapidScat, incidence angle values span a range close to 3 degrees over a single orbital pass for both beams.

Changes in ISS attitude and altitude can significantly affect the ability of RapidScat to make accurate σ^0 measurements, due to range gating and ambiguous Doppler slice selection. However, these effects have been included in NASA Jet Propulsion Laboratory (JPL) processing of the L1B files used for this thesis [9]. L1B data files contain vectors of sequential measurements from the instrument. The JPL σ^0 values in the data are considered to be accurate in this thesis, so error in σ^0 measurements is assumed to not be caused by range and pointing-vector changes. However, LTOD and incidence angle variation are shown in this thesis to produce variability in the values of the σ^0 measurements.

When making radar images (such as SIR images), changes caused by these parameters lead to noisy pixel values, since measurements from multiple passes are combined, which include different LTOD and incidence angle values. SIR images are enhanced-resolution radar images created from scatterometer L1B data [14]. In order to make these images, the σ^0 measurements are assumed to be azimuthally isotropic, and σ^0 variations caused by incidence angle variations are normalized to be at a single, nominal incidence angle. LTOD has historically been constant for scatterometer data, because previous scatterometers were flown in sun-synchronous orbits. However, this is not the case for RapidScat measurements. SIR images are typically made as 1-day, 2-day, 4-day, or 30-day images, and a significant amount of variation in RapidScat σ^0 is caused by LTOD changes over these day ranges.

Ideally, variations in σ^0 measurements that are not caused by vegetation and other land features are removed so that the images primarily represent land characteristics. Simple models of backscatter versus LTOD, incidence angle, and other parameters can be employed to compute adjustments to σ^0 in order to normalize variability in σ^0 caused by variations of these parameters from their nominal value.

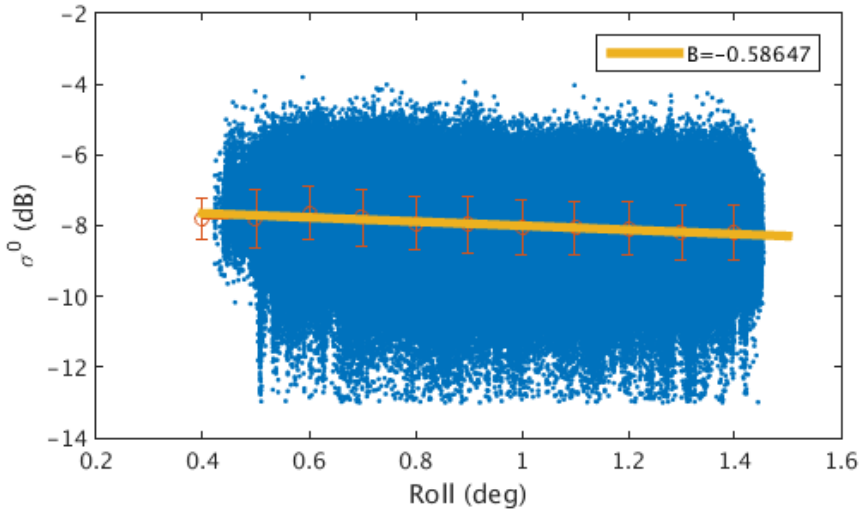

Figure 3.1: Scatter plot of σ^0 versus roll angle, including the mean (circles) and standard deviation (bars) at several roll angle bins. The solid line in the middle of the data is the first-order polynomial (linear) model of σ^0 dependence on roll angle. Note the definite downward slope. This model has a slope of -0.586 dB/deg (represented by the letter "B"). Data from days 1-151 of 2016 over the Amazon mask.

Since incidence angle variations for RapidScat are caused by variations in the attitude of the ISS, attitude variations are considered to be significant parameters that affect σ^0. Roll and pitch angles can both affect σ^0 values. This can be seen by a direct correlation between σ^0 measurements and the roll and pitch angles, as seen in Figs. 3.1 and 3.2. Fig. 3.1 shows a slope of -0.59 dB/deg for σ^0 dependence on roll angle in dB space. Fig. 3.2 shows σ^0 dependence on pitch angle in dB space, but there is not an clear model to use for σ^0 dependence on pitch angle, even though there is a significant correlation. Since there is a significant correlation for both of these parameters, σ^0 dependence on both roll and pitch angle are used as metrics for evaluating the effectiveness of σ^0 adjustments. If the magnitude of the slope of σ^0 dependence on roll or pitch angle is reduced, the adjustment is considered to be effective.

Since the SIR algorithm assumes that σ^0 is azimuthally isotropic, σ^0 dependence on azimuth angle is also a significant metric to consider when adjusting σ^0 measurements. RapidScat data is already fairly isotropic in this sense, but it is not as good as QuikSCAT data (see Fig. 3.25). Adjustments to σ^0 are considered to be effective if the amount of variation in σ^0 across the full range of azimuth angles is reduced.

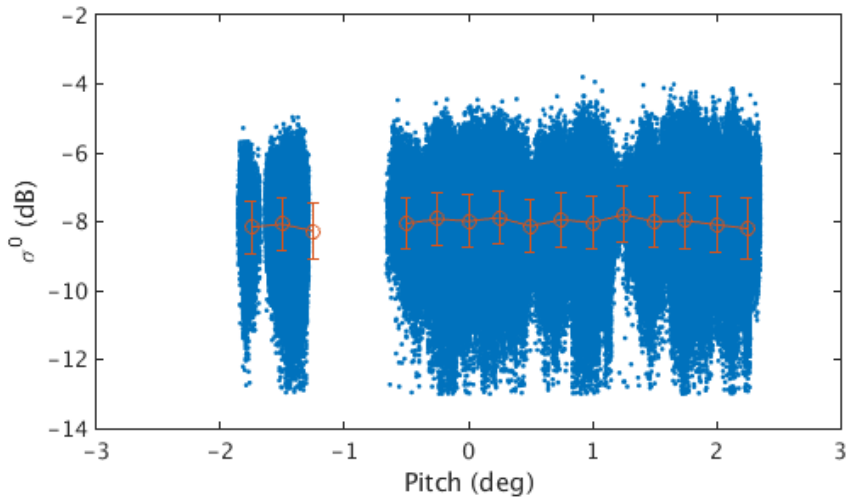

Figure 3.2: Scatter plot of σ^0 versus pitch angle, including the mean (circles) and standard deviation (bars) at several roll angle bins. Note that the mean values of each bin do not follow a consistent pattern that reflects a clear model for σ^0 dependence on pitch angle. However, σ^0 is dependent on pitch angle to some degree. Data from days 1-151 of 2016 over the Amazon mask.

In total, five parameters are chosen for modeling σ^0 dependence because of their significant effect on σ^0 values. These parameters are roll angle, pitch angle, azimuth angle, LTOD, and incidence angle. By modeling σ^0 dependence on each parameter, it is possible to normalize σ^0 dependence, as well as measure the effectiveness of σ^0 adjustments. For simplicity, the dependence of σ^0 is modeled for each parameter each time that σ^0 is adjusted. In other words, the modeling and normalization is done sequentially. Since the models of σ^0 dependence are not independent, the coefficients of each model may change as σ^0 values are altered. The models of σ^0 dependence are explained in this chapter, and the models are used in the next chapter for removing this dependence.

3.2 Data Masking

To estimate the coefficients of a σ^0 dependence model, the data are restricted to measurements taken within a homogeneous data target, meaning there is a nearly uniform response across all azimuth angles. This homogeneity enables identification of σ^0 dependence on the significant parameters, such as incidence angle or LTOD.

To restrict data to be within a homogeneous region, a mask is created over the Amazon rainforest. The Amazon is chosen for its homogeneity of vegetation and landscape over a large region and minimal changes from day to day. The mask is chosen from locations that historically (over several years) have an average backscatter value within ± 0.5 dB of the mean value of Amazon measurements. This mask is made using an average of 4-day QuikSCAT images from 10 consecutive years, using data only from the last three months of the year (October–December) to remove seasonal variations in σ^0. QuikSCAT images are used to determine homogeneous locations because of the long mission life and low measurement noise of the QuikSCAT mission.

The Amazon mask is chosen by using an iterative algorithm [8]. First, an average image is formed from QuikSCAT data. In this case, 4-day SIR images from the last three months of the years 1999-2008 are averaged together. A pixel value that is representative of the Amazon is chosen as the initial mean value of the mask. Then all pixel values in the image are compared to this initial mean value. All the pixels in the image that are within ± 0.5 dB of the mean value are included in the mask. The algorithm iterates by calculating a new mean value from the pixels contained in the current mask. The pixels in the image are then compared with this new mean value. Pixel values that fall within ± 0.5 dB of the new mean value are included in the new current mask. This algorithm repeats until the mask is no longer altered significantly between iterations. To achieve this final mask, the algorithm is iterated 100 times. Then regions that are not part of the Amazon rainforest are removed, since heavily forested regions in other parts of South America tend to be included by this algorithm. The mask used in this chapter can be seen in Fig. 3.3.

In this chapter, the mask over the Amazon is used to limit which RapidScat σ^0 measurements are included for estimating models of σ^0 dependence over the Amazon. Only measurements that are centered within the mask locations are included. Restricting data to be in these locations helps to ensure that any variations that occur to σ^0 across the range of a parameter value are caused by that parameter, instead of spatial variation in the landscape.

3.3 Estimating Models

Other Ku-band scatterometers and radars can be employed to characterize a model for RapidScat data. To estimate a model for RapidScat σ^0 dependence, the σ^0 dependence on a

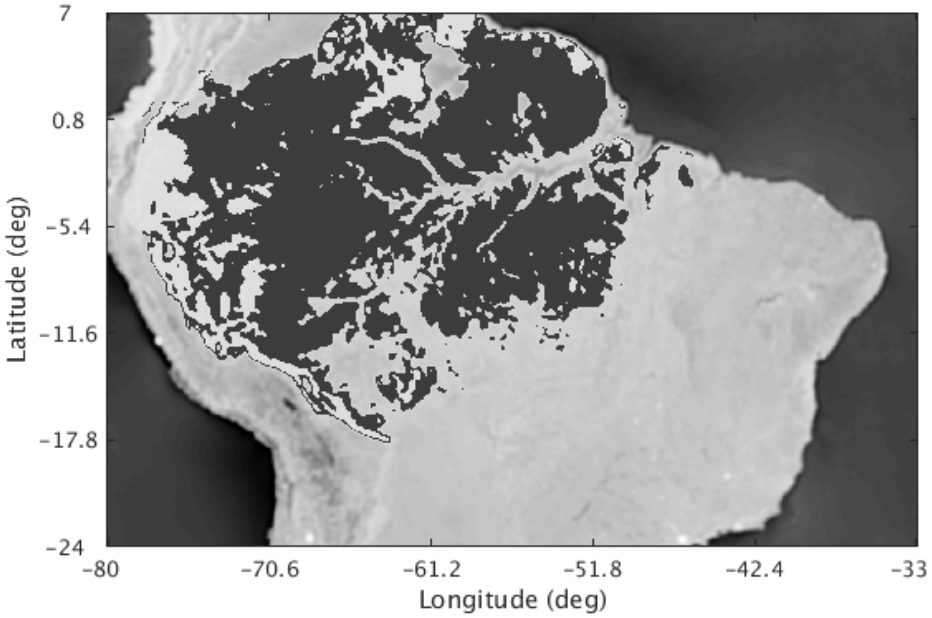

Figure 3.3: Image of the mask locations over the Amazon rainforest, superimposed over a SIR radar image of South America. The dark pixels over the Amazon rainforest designate the mask. This mask represents the pixels that are within ± 0.5 dB of the mean value of all the pixels in the mask. This mask was created by using pixel values in a 10-year average QuikSCAT SIR image.

parameter is first plotted for several Ku-band instruments. Then the RapidScat model is designed by comparing its measurements to these other Ku-band scatterometer measurements.

Backscatter measurements from masked locations are plotted versus a parameter, and a least squares fit is used to estimate a model for the dependence of σ^0 on this parameter. A uniform sampling distribution of parameter data helps to ensure that this least squares method works effectively. However, using masked data creates non-uniform sampling distributions for most parameters. The sampling distribution for each σ^0 dependence model is analyzed in subsequent sections to determine how accurate the models are, even without a completely uniform sampling distribution for each parameter.

The σ^0 measurements are modeled for each significant parameter as a mean σ^0 functionvalue, plus some variation caused by changes in the surface, noise in the receiver, and other parameter variations. The mean σ^0, $f(\mathbf{x})$, is a function of the significant parameter and reflects any significant σ^0 dependence. The variation from the mean is represented by v and is modeled as white noise.

The modeled σ^0

$$\sigma^0 = f(\mathbf{x}) + \nu \;\; dB, \tag{3.1}$$

where σ^0 is a vector of σ^0 measurements, $f(\mathbf{x})$ is an affine model of the mean σ^0, $\mathbf{x}$ is a vector of the significant parameter values, and $\nu \sim N[\mathbf{0}, \sigma_\nu^2 \mathbf{I}]$ is a vector of independent, identically-distributed (iid) normal random variables. The affine model, $f(\mathbf{x})$, is defined by an observation matrix, $\mathbf{H}$, multiplied by a coefficient vector, $\mathbf{c}$,

$$f(\mathbf{x}) = \mathbf{H}\mathbf{c}, \tag{3.2}$$

where the coefficients are estimated according to a least-squares psuedo-inverse,

$$\hat{\mathbf{c}} = (\mathbf{H}^\top \mathbf{H})^{-1} \mathbf{H}^\top \sigma^0, \tag{3.3}$$

and $\mathbf{H}$ is a known matrix of predetermined basis vectors. Because the coefficients are estimated by a least-squares psuedo-inverse, the affine model $f(\mathbf{x})$ can be estimated by a projection of σ^0 onto the space of the observation matrix, $\mathbf{H}$, where the estimate

$$\begin{aligned} \hat{f}(\mathbf{x}) &= \mathbf{H}\hat{\mathbf{c}} \\ &= \mathbf{H}(\mathbf{H}^\top \mathbf{H})^{-1} \mathbf{H}^\top \sigma^0 \\ &= \mathbf{P}_\mathrm{H} \sigma^0. \end{aligned} \tag{3.4}$$

Only the affine model $f(\mathbf{x})$ is estimated for each parameter. The unknown variance caused by unmodeled parameters and receiver noise is ignored.

This least-squares method is used in this chapter to estimate $f(\mathbf{x})$ for each significant parameter that affects σ^0. Each model for σ^0 dependence is either used to normalize the σ^0 dependence or to create a metric to test the effectiveness of adjusting σ^0.

3.3.1 Model Assumptions

The variation in the model (ν) is assumed to be normally distributed. Since receiver noise is actually additive Gaussian white noise, in dB space it is log normal. Two histograms of some

RapidScat σ^0 values in the Amazon mask for a range of six days are shown in Fig. 3.4. This figure shows that the distributions both look nearly normal, though the long tails on the left suggest they may be log normal. Since several thousand measurements are combined, for simplicity, the distributions are assumed to be normal. Future analysis can include the potential mean bias caused by using least squares with a log normal distribution.

3.4 Incidence Angle Model

In order to estimate the model for σ^0 dependence on incidence angle for RapidScat, Ku-band σ^0 measurements from various instruments are compared. For this analysis, NSCAT, Oscat, TRMM, QuikSCAT, and RapidScat data are compared. For each dataset, σ^0 measurements are plotted as a function of their respective incidence angle measurements. These plots are combined together into a single plot to show the general shape of Ku-band σ^0 response to incidence angle over the Amazon (see Figs. 3.5 and 3.7).

The σ^0 dependence on incidence angle for RapidScat in general is represented as a straight line in dB space (see Fig. 3.6). The model function

$$\begin{aligned} f(\theta) &= K_\theta \mathbf{1} + B\theta \\ &= [\, \mathbf{1} \mid \theta \,][\, K_\theta \; B \,]^\top \\ &= \mathbf{H}_\theta \mathbf{c}_\theta, \end{aligned} \tag{3.5}$$

where $B \approx -0.1$ dB/deg over the Amazon for the wet season (days 1–151), $\mathbf{1}$ represents a column vector of ones, θ represents a column vector of measured incidence angle values, and K_θ and B are the coefficients of the affine model. The coefficient values vary for different regions and different day ranges. This model is estimated by a least-squares fit of RapidScat data. This first-order polynomial is similar to the shape of NSCAT measurements over the same incidence angle range (see Fig. 3.6). The measurements of Oscat and QuikSCAT largely seem to agree with the NSCAT measurements as well. RapidScat measurements have a similar shape, but on average its σ^0 values are lower than NSCAT values.

Over the range of angles measured by RapidScat, the shape of the σ^0 dependence on incidence angle is best modeled as a line with a gently decreasing slope (see Fig. 3.6). RapidScat

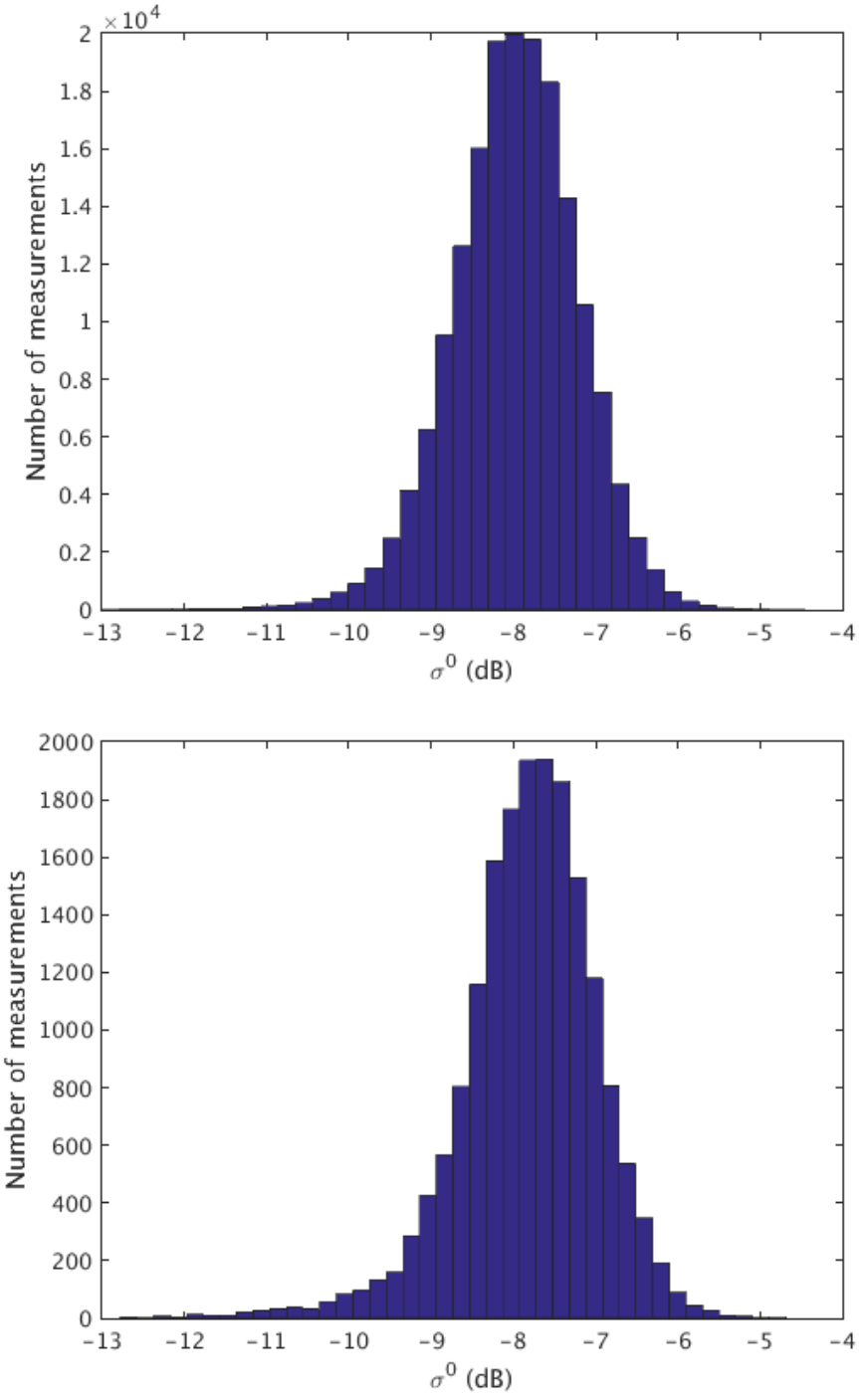

Figure 3.4: Histograms of σ^0 within the Amazon mask for 6 days of data. Top: histogram of all σ^0 values. Bottom: histogram of σ^0 within a bin of 0.5 hours of LTOD. Note in both cases that the distribution looks nearly normal, but both are more similar to a log normal distribution, with slightly more values present at the lower end of the distribution.

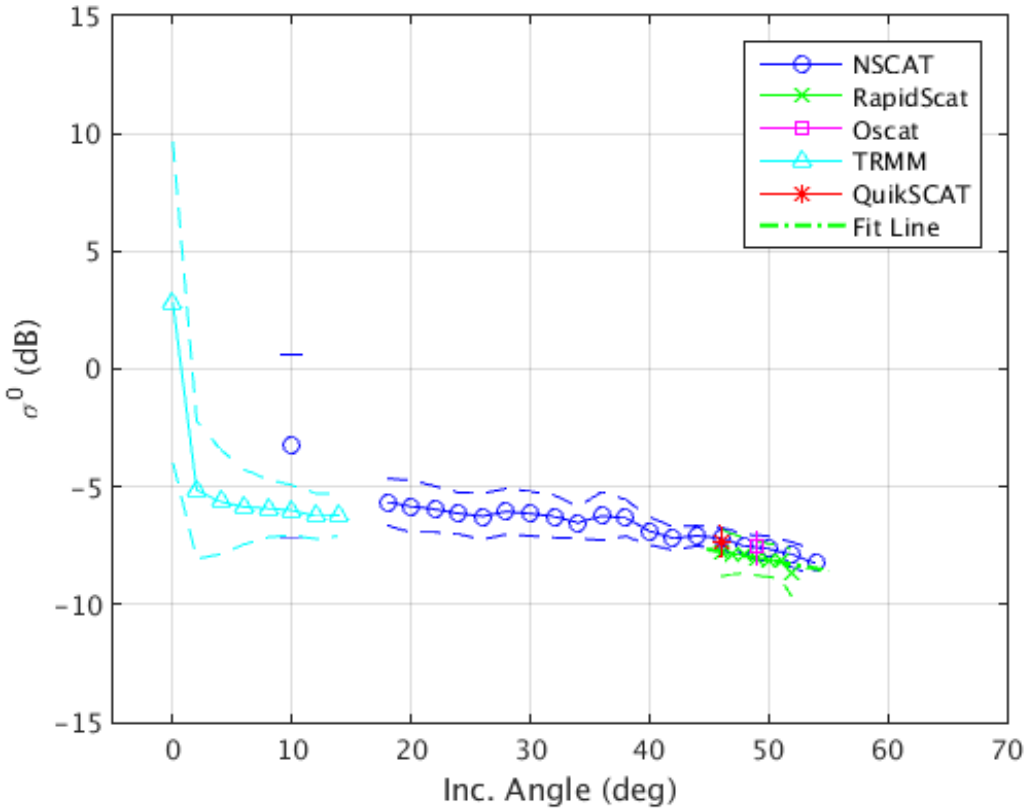

Figure 3.5: Mean and standard deviation of σ^0 dependence on incidence angle for multiple Ku-band scatterometers: TRMM, NSCAT, RapidScat, Oscat, and QuikSCAT. These measurements match a general shape of the incidence angle dependence, as seen in Fig. 3.7.

σ^0, however, has a subtle but distinct parabolic shape over its range, compared to NSCAT (see Fig. 3.6). Since this is an anomaly compared to other scatterometers, a linear fit is used (instead of a parabola) to describe the model for this parameter, to match other scatterometers. The parabolic shape does not appear to be caused by incidence angle variations alone.

Additionally, RapidScat models are made for different day ranges. For SIR image processing, data from a variable length of day ranges are used. The range of days used is typically 1, 2, 4, or 30 days. The same first-order polynomial fit is used to model incidence angle dependence for any day range.

Since these models of σ^0 dependence on incidence angle are estimated by a least-squares method, the sampling distribution of incidence angle values is considered. As the number of

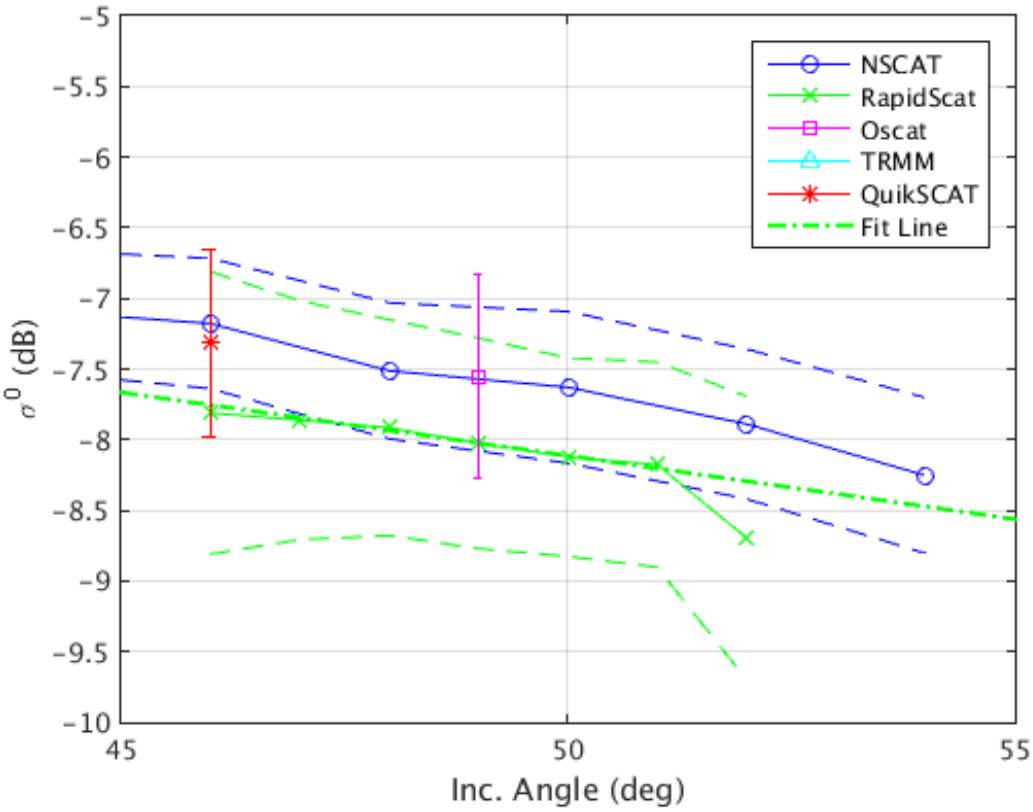

Figure 3.6: Zoomed-in version of Fig. 3.5 in the range of RapidScat incidence angles. Because RapidScat only measures over a small range of incidence angles compared to NSCAT, the variation for RapidScat is modeled as a straight line (shown as a dotted green line across the full range of RapidScat incidence angles). The parabolic shape is ignored because it is not consistent with the dependence on incidence angle demonstrated by other scatterometers.

samples in an incidence angle range increases, the least squares estimate tends to be more accurate over that range.

3.4.1 Sampling Distribution of Incidence Angle

The mask of the Amazon rainforest (see Fig. 3.3) is used to ensure that σ^0 measurements considered are spatially homogeneous, which enables a clear identification of σ^0 dependence on incidence angle. In this section, the sampling distribution of the incidence angle values within the mask is considered in order to determine the accuracy of a least-squares model.

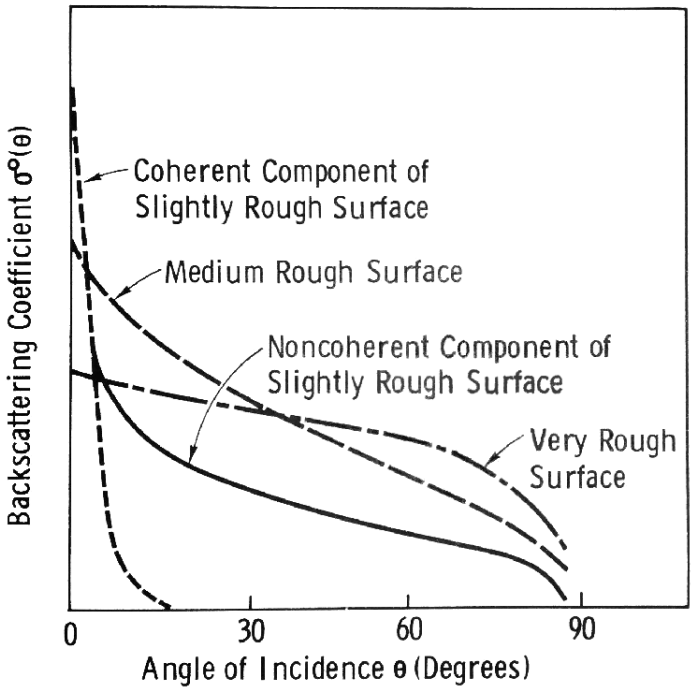

Figure 3.7: Conceptual curves of microwave radar backscatter dependence on incidence angle. Note the similarity with the TRMM and NSCAT curves in Fig. 3.5. From Ulaby et al., 1982 [12].

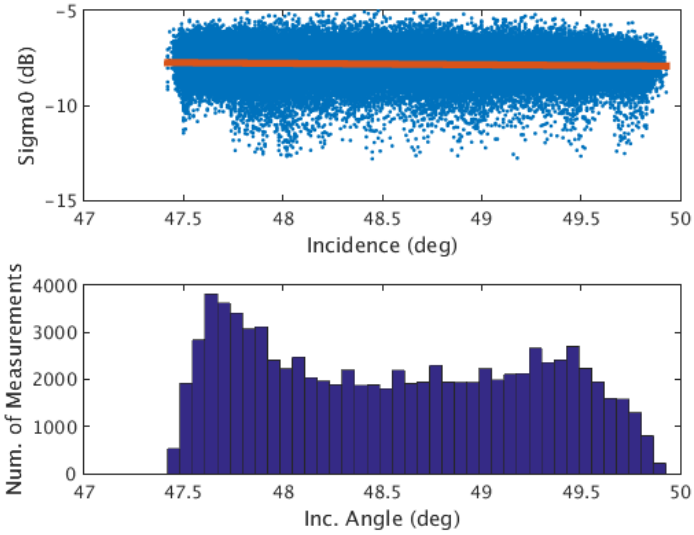

Figure 3.8: Histogram of sampled incidence angle values of the inner beam of RapidScat for a six-day range in the Amazon mask (days 100–105, 2015). Note the presence of two modes, one on the low end and one at the high end of the incidence angle range.

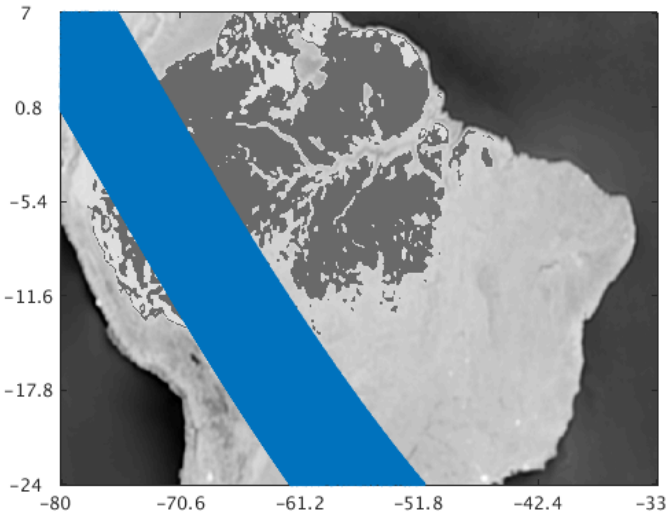

Figure 3.9: Unmasked measurement locations for orbit revolution 3090 (rev 3090) over South America. The dark band across the image marks the measurement locations. The dark pixels over the Amazon designate the mask. This measurement swath is a descending pass from rev 3090, day 100, 2015.

The sampling distribution is determined by creating a histogram of incidence angle values used for a model of σ^0 dependence. An example of this can be seen for an arbitrary six-day range (days 100-105, 2015) in Fig. 3.8. Significant non-uniform modes can be seen in the distribution of incidence angle in this case. The presence of such modes are analyzed in data from two sequential passes of the radar. Only the inner beam is analyzed, because a similar distribution of samples is seen in the outer beam data. First, the pass over the Amazon from orbit revolution 3090 (rev 3090), from day 100, 2015, of RapidScat (Fig. 3.9) is analyzed, and then orbit revolution 3089 (rev 3089), from day 100, 2015, of RapidScat is analyzed (Fig. 3.10).

In rev 3090, incidence angle variation across the swath can be observed, as seen in Fig. 3.11, perpendicular to the direction of travel for the spacecraft. This pattern of incidence angle variation appears to occur in general, suggesting that roll angle is a principle factor affecting incidence angle variation. Because of where the mask intersects the measured locations of the swath, the mask removes more measurement locations on one part of the swath than the other (see Fig. 3.12). Removing these locations causes certain incidence angle values to be reduced in the sampling distribution of incidence angle, with a greater number of higher incidence angles being present in

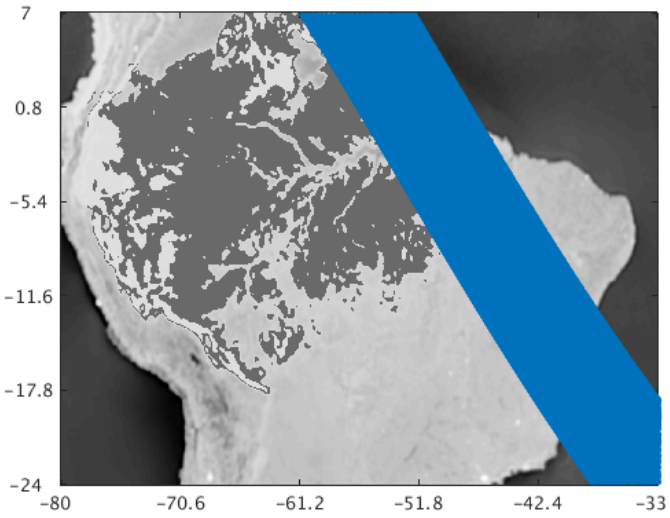

Figure 3.10: Unmasked measurement locations for orbit revolution 3089 (rev 3089) over South America. The dark band across the image marks the measurement locations. The dark pixels over the Amazon designate the mask. This measurement swath is a descending pass from rev 3089, day 100, 2015.

the data, because the northeast side of the swath intersects a larger area of the mask than the other side (see Fig. 3.13).

In rev 3089, a similar effect is caused by the intersection of the swath with the mask. The swath of this rev crosses the Amazon on the opposite side of the Amazon mask (see Fig. 3.10). For this rev, only the southwest part of the swath has significant area intersecting with the mask (Fig. 3.14). Because of how the incidence angle values vary across the swath (similar to rev 3090, as in Fig. 3.11), a greater number of lower incidence angle values is selected by the mask (see Fig. 3.15).

When data from both passes are combined, a bimodal pattern appears, as seen in Fig. 3.8. Though the incidence angle values are not strictly uniform, the values do not necessarily suggest a bias in the sampling distribution of RapidScat. Fortunately, this sampling distribution is relatively uniform and has a sufficient number of points, which enables a good least squares estimate.

Fig. 3.16 shows the distribution of incidence angle values measured for RapidScat model over the first five months of the year in 2016. This shows the range of incidence angles possible for RapidScat over several months. The shape of the distribution is determined by locations removed

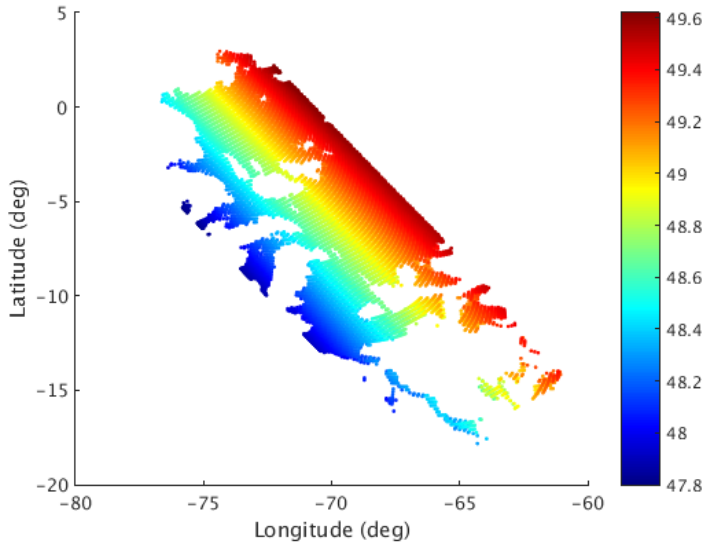

Figure 3.11: Incidence angle values across the masked swath measurements from rev 3090 (Fig. 3.12). Note that the northeast half of the swath correlates to higher incidence angle values and that the southwest half correlates to lower values. In addition to explaining a non-uniform sampling distribution, this figure suggests that there is a consistent non-zero roll angle for all the measurements in the swath, because the incidence angle variations are orthogonal to the direction of the orbit. Note that the northeast half of the masked swath has a greater total area than the southwest half.

by the mask, as well as variation in the range of incidence angle values that is caused by a changing roll angle. Though the distribution is not uniform, there are a significant number of values in the center section of the range.

The coefficients of this first-order polynomial model for σ^0 dependence on incidence angle may change, depending on the number of days used to estimate them and the location of the measurements. However, the sample distributions analyzed in this section for short day ranges (see Fig. 3.8) and much longer day ranges (see Fig. 3.16) have a sufficient number of measurements in the center range to create an accurate least-squares model.

3.4.2 Incidence Angle Model Summary

In summary, RapidScat σ^0 dependence on incidence angle is modeled in dB space as a first-order polynomial. RapidScat samples of incidence angle are not fully uniform within the Amazon mask due to the intersection of the mask and the swath. However, a significant number of

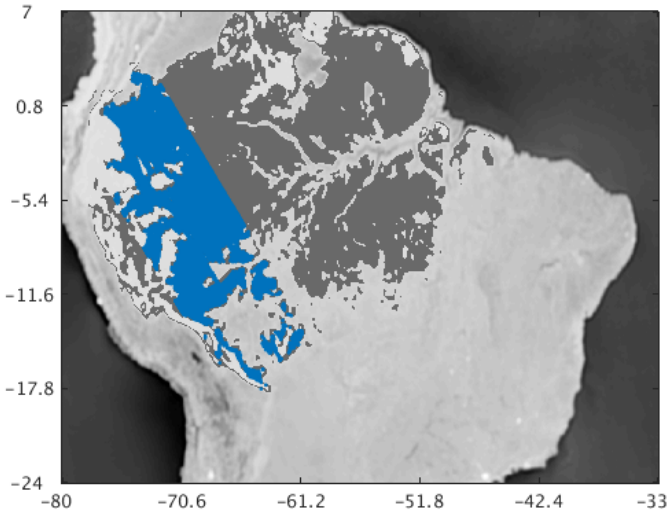

Figure 3.12: Masked measurement locations for orbit rev 3090 over South America. The darkest pixels over the Amazon rainforest mark the measurement locations for rev 3090 within the Amazon mask. The dark pixels over the Amazon designate the whole mask. Compare with Fig. 3.9. Note that the swath has greater area in the northeast half of the swath than the southwest half. Because of where the Amazon mask and the measurement swath intersect, there are more measurements removed from one side of the swath than the other. This measurement swath is a descending pass from rev 3090, day 100, 2015.

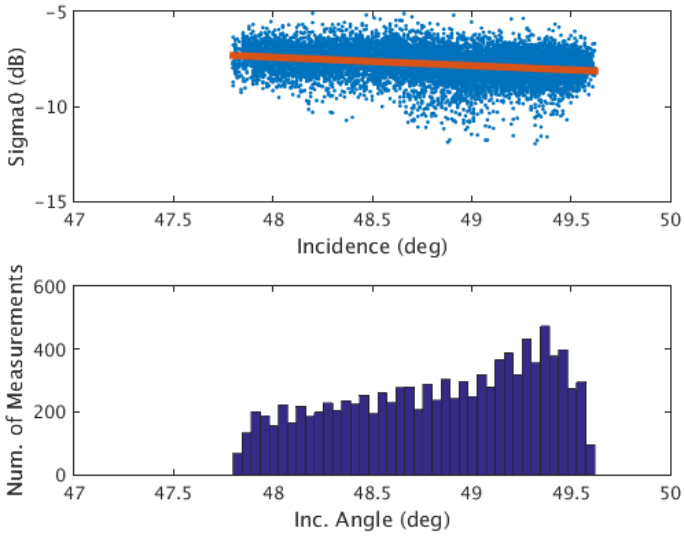

Figure 3.13: Histogram of incidence angle values present from rev 3090 across the Amazon mask. There are more incidence angle values on the high end of the range, rather than the low end. This is caused by locations being masked out in this pass (see Figs. 3.12 and 3.11).

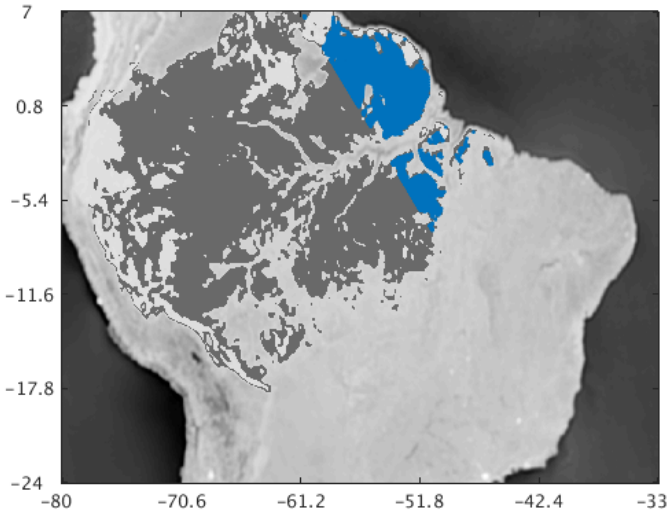

Figure 3.14: Masked measurement locations for rev 3089 over South America. The darkest pixels over the Amazon rainforest mark the measurement locations within the Amazon mask. The dark pixels over the Amazon designate the whole mask. Compare with Fig. 3.10. Note that the swath has greater area in the southwest half of the swath than the northeast half. Because of where the Amazon mask and the measurement swath intersect, there are more measurements removed from one side of the swath than the other. This measurement swath is a descending pass from rev 3089, day 100, 2015.

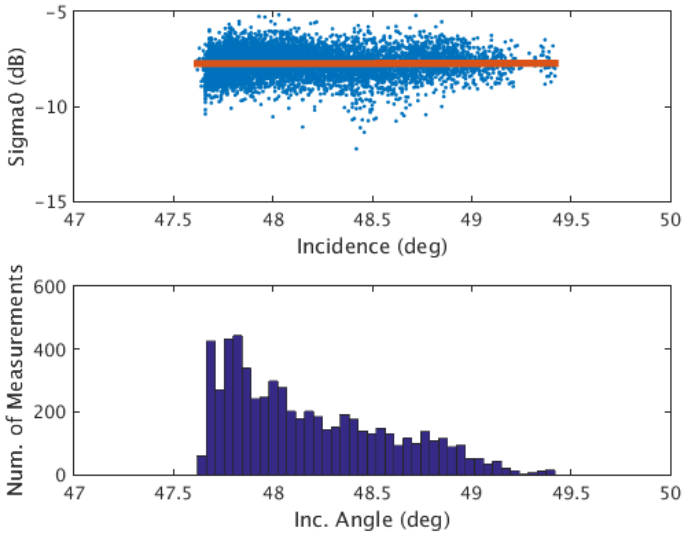

Figure 3.15: Histogram of incidence angle values present from the rev 3089 across the Amazon mask. There are more incidence angle values on the low end of the range, rather than the high end. This caused by locations being masked out in this pass (see Fig. 3.14).

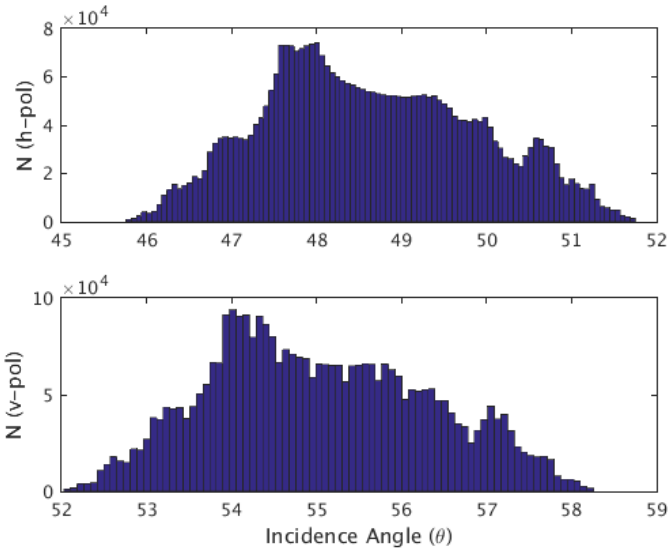

Figure 3.16: Histogram of sampled incidence angle values for the inner (top) and outer (bottom) beams of RapidScat for the first five months of 2016 over the Amazon mask. Note the presence of one significant mode on the low end of the incidence angle range. This histogram provides a good representation of how wide the range can be over the course of five months.

values are present for the majority of the range of incidence angles for the day ranges used for SIR images.

3.5 LTOD Model

In order to estimate the model for σ^0 dependence on LTOD for RapidScat, Ku-band σ^0 measurements from various instruments are again compared. For this analysis, TRMM, NSCAT, QuikSCAT, and RapidScat data are compared. For each dataset, σ^0 measurements are plotted as a function of their respective LTOD measurements. These plots are combined into a single plot to show a general Ku-band σ^0 dependence on LTOD over the Amazon (see Fig. 3.17).

In Fig. 3.17, NSCAT and QuikSCAT data are restricted to a few small time ranges because of their sun-synchronous orbits. However, the σ^0 measurements over those small ranges show changes that are similar to the changes of σ^0 dependence on LTOD for TRMM and RapidScat. The TRMM data are included because the TRMM satellite is in a non-sun-synchronous orbit like RapidScat, so the TRMM data also span a full 24 hour period. Though the coefficients of RapidScat and TRMM σ^0 dependence on LTOD are somewhat different, the models for each radar follow a

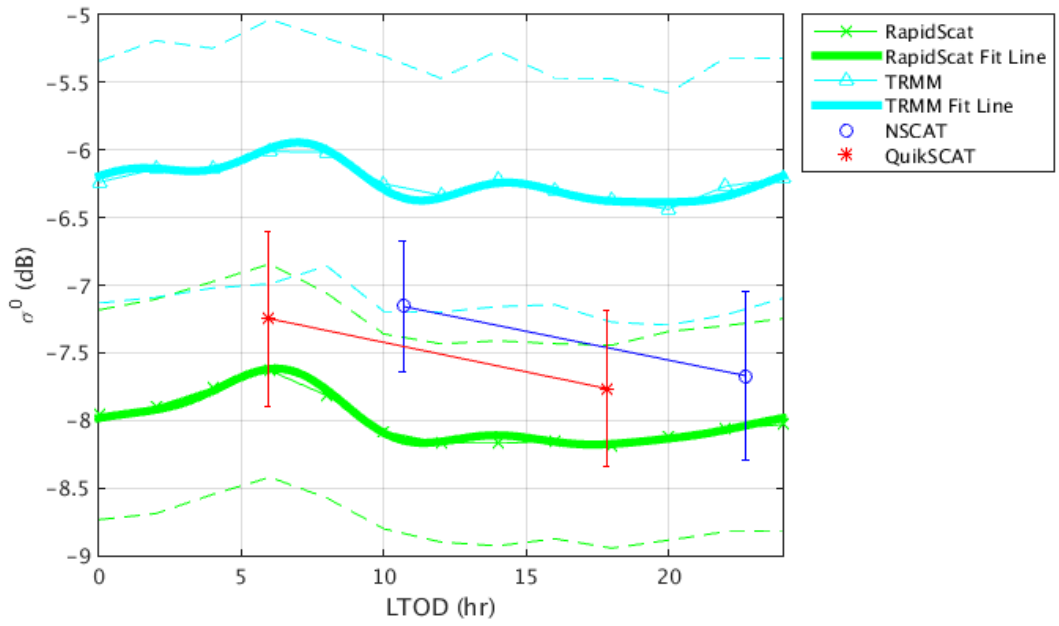

Figure 3.17: Mean and standard deviation for dependence of σ^0 on LTOD for RapidScat, TRMM, QuikSCAT, and NSCAT. Both TRMM and RapidScat measure σ^0 over a full range of LTOD because of non-sun-synchronous orbits. Both TRMM and RapidScat models show a periodic variation, with a peak close to 6 am. The average of σ^0 measurements is significantly higher for TRMM, due to a lower incidence angle range. Only TRMM measurements with incidence angle values greater than 10 degrees are used in order to remove the larger bias of the nadir measurements.

similar pattern over the full range of 24 hours. RapidScat is the only Ku-band wind scatterometer to measure a full 24 hours of LTOD. TRMM also measures σ^0 in the Ku-band over a full 24 hours of LTOD, but it is not designed to be a wind scatterometer, and so measures at much lower incidence angle values than RapidScat does. TRMM measurements are at a higher average σ^0 value because they are measured at a much lower incidence angle range (see Fig. 3.5). However, only measurements measured at incidence angle values greater than 10° are used for estimating σ^0 dependence on LTOD for TRMM. Restricting TRMM data to this incidence angle range makes the data more comparable with RapidScat data.

The dependence of σ^0 on LTOD for RapidScat over a full 24 hours of LTOD is represented as a fourth-order Fourier series model. This model is effective at representing a periodic variation with a significant peak in σ^0 at 6 am (as seen in Fig. 3.17). This model nearly matches the mean at each LTOD bin value. Higher order periodic models can be used to model this behavior, but

higher models may introduce noise into adjusted σ^0 values when they are used for a normalization procedure. Additionally, a fourth-order Fourier model is shown to be effective at removing azimuth angle biases present in Oscat data [15]. The model function

$$
\begin{aligned}
f(\tau) &= K_\tau + \sum_{i=1}^{4} A_i \cos(i\tau\omega) + B_i \sin(i\tau\omega) \\
&= \begin{bmatrix} 1 & \cos(1\tau_1\omega) & \sin(1\tau_1\omega) & \dots & \cos(4\tau_1\omega) & \sin(4\tau_1\omega) \\ 1 & \cos(1\tau_2\omega) & \sin(1\tau_2\omega) & \dots & \cos(4\tau_2\omega) & \sin(4\tau_2\omega) \\ \vdots & \vdots & \vdots & & \vdots & \vdots \\ 1 & \cos(1\tau_N\omega) & \sin(1\tau_N\omega) & \dots & \cos(4\tau_N\omega) & \sin(4\tau_N\omega) \end{bmatrix} \begin{bmatrix} K_\tau \\ A_1 \\ B_1 \\ \vdots \\ A_4 \\ B_4 \end{bmatrix} \\
&= \mathbf{H}_\tau \mathbf{c}_\tau,
\end{aligned}
\tag{3.6}
$$

where $\omega = \frac{2\pi}{24}$ to create a model with a period of 24 hours; τ is a vector of RapidScat LTOD values; τ_i is a specific LTOD value from this vector of values; N is the number of values in this vector; and where K_τ, A_i, and B_i are the estimated coefficients of the model. A least-squares fit of the data is calculated to estimate the coefficients of this model. A large number of measurements is used (from five months) over the Amazon to reduce undesired biases from RapidScat in the data when estimating this least squares model.

3.5.1 Shorter Day Ranges

However, SIR images are made typically using only 1, 2, 4, or 30 days of data. Additionally, SIR images may only use ascending and descending passes over a range of days, or they may use both passes. For example, Fig. 3.18 shows how σ^0 dependence on LTOD might be modeled for a range of six days. In this figure, a fourth-order Fourier series is used (as above), as well as two first-order polynomial models for the separate ranges. When the range of LTOD values is less than four hours in a disjoint range, the Fourier model has significantly different coefficients than a model estimated from a model estimated from a full 24 hours (see Fig. 3.17). Fig. 3.19 shows an example of using only ascending passes over a range of six days. Figs. 3.20 and 3.21 show

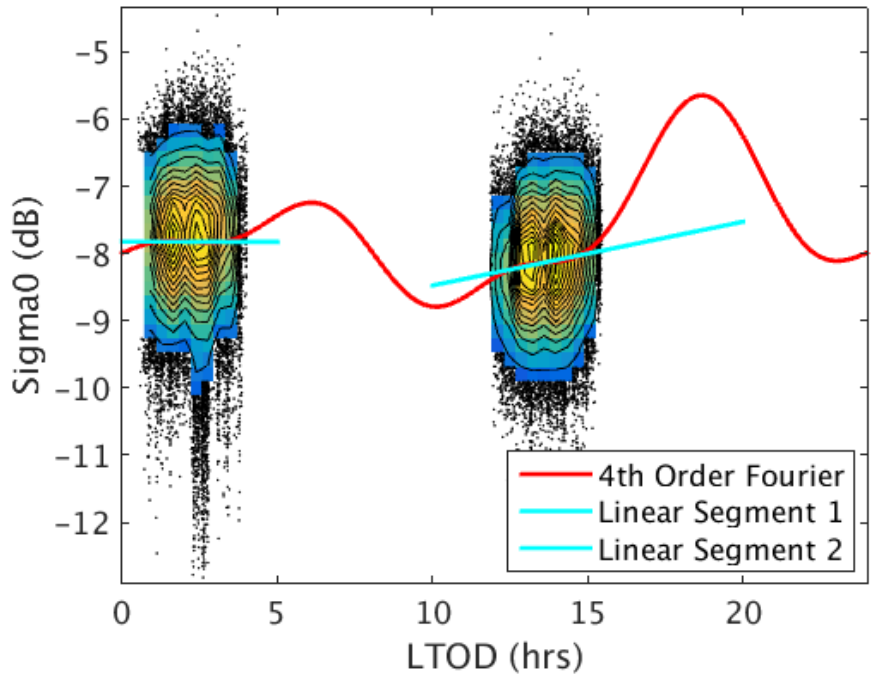

Figure 3.18: Scatter plot of σ^0 versus LTOD for Days 100–105, 2015, for RapidScat. Note that the LTOD ranges are disjoint and are separated by a range close to 12 hours. Each disjoint set spans a range less than 4 hours of LTOD.

an even more significant deviation from the expected Fourier model shape seen in Fig. 3.17. For these cases where the disjoint ranges of LTOD are both less than four hours, a linear fit is more consistent with the model seen in Fig. 3.17.

Therefore, a linear model is more appropriate for disjoint ranges that are smaller than 4 hours. In this case, the model function

$$\begin{aligned} f(\tau) &= K_\tau + B\tau \\ &= [\,\mathbf{1} \mid \tau\,][\,K_\tau\ B\,]^\top \\ &= \mathbf{H}_\tau \mathbf{c}_\tau, \end{aligned} \tag{3.7}$$

where τ is a column vector of LTOD values from a single disjoint range, $\mathbf{1}$ is a column vector of ones, K_τ and B are the coefficients of the model, $\mathbf{H}_\tau$ is the observation matrix for LTOD, and $\mathbf{c}_\tau$ is the vector of coefficients. For the case of using both ascending and descending passes, two separate models are estimated.

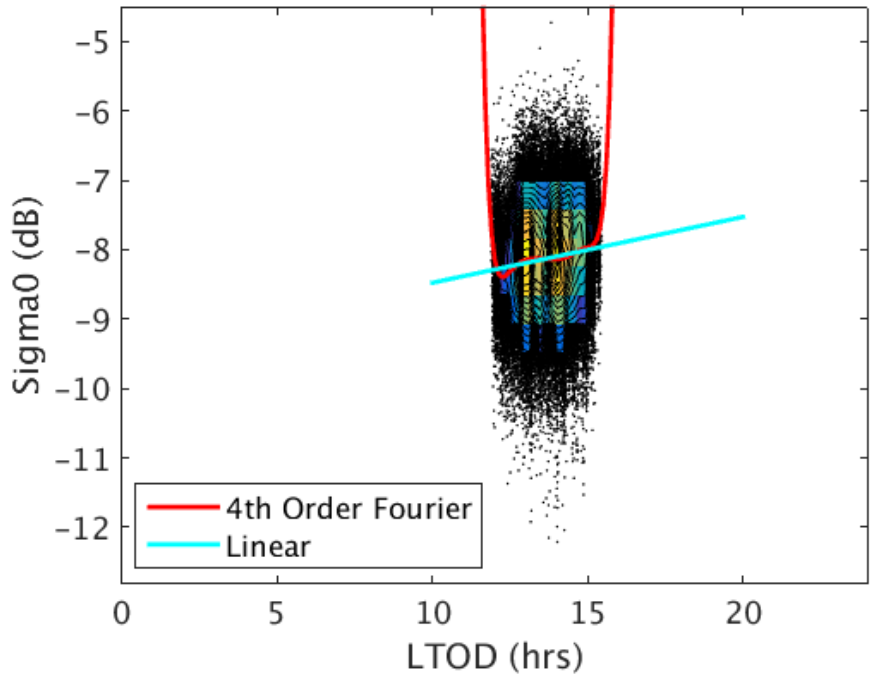

Figure 3.19: Scatter plot of σ^0 versus LTOD for Days 100–105, 2015, ascending nodes only, for RapidScat. Note that LTOD values span a range smaller than 4 hours. Both a fourth-order Fourier model and first-order polynomial model are shown. Figs. 3.20 and 3.21 show the details of the Fourier model in the center and outer ranges.

3.5.2 LTOD Metric

Additionally, a different model of LTOD is used as a metric for how effective normalization of σ^0 dependence on incidence angle and LTOD is. The model

$$\begin{aligned} f(\tau) &= K_\tau + A_1\cos(\tau\omega) + A_2\sin(\tau\omega) \\ &= [\,\mathbf{1} \mid \cos(\tau\omega) \mid \sin(\tau\omega)\,][\,K_\tau\, A_1\, A_2\,]^\top \\ &= \mathbf{H}_\tau \mathbf{c}_\tau, \end{aligned} \tag{3.8}$$

where $\omega = \frac{2\pi}{24}$ to ensure a period of 24 hours; τ is a column vector of LTOD values from RapidScat; $\mathbf{1}$ is a column vector of ones; K_τ, A_1, and A_2 are the coefficients of the model; $\mathbf{H}_\tau$ is the observation matrix for LTOD; and $\mathbf{c}_\tau$ is the vector of coefficients. This lower-order periodic model of σ^0 dependence on LTOD is used as a metric because it is simple to calculate and can reveal variability remaining in the dependence model after adjustments are made. Additionally, this lower-order

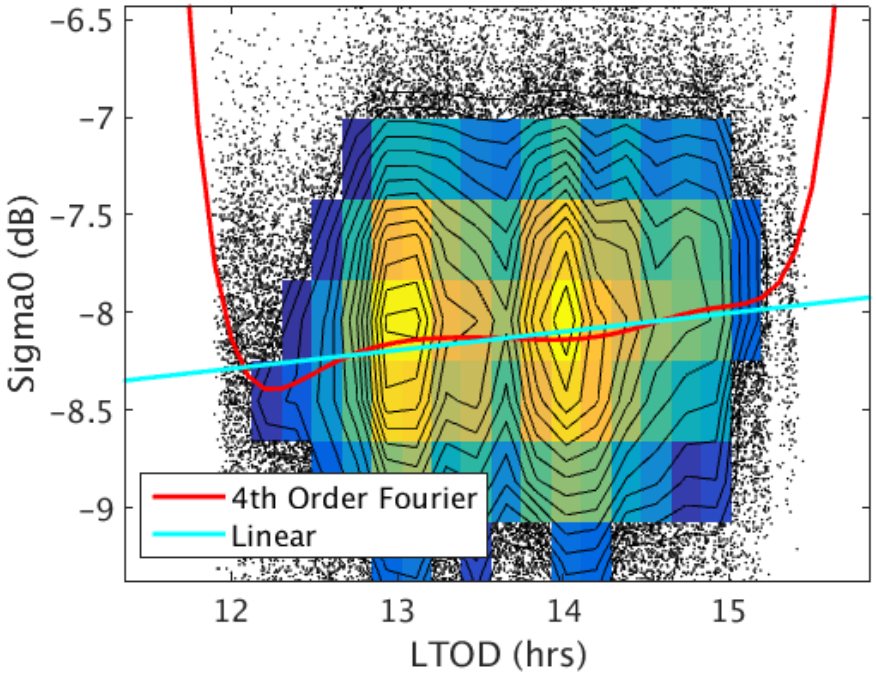

Figure 3.20: Zoomed-in version of central range of Fig. 3.19.

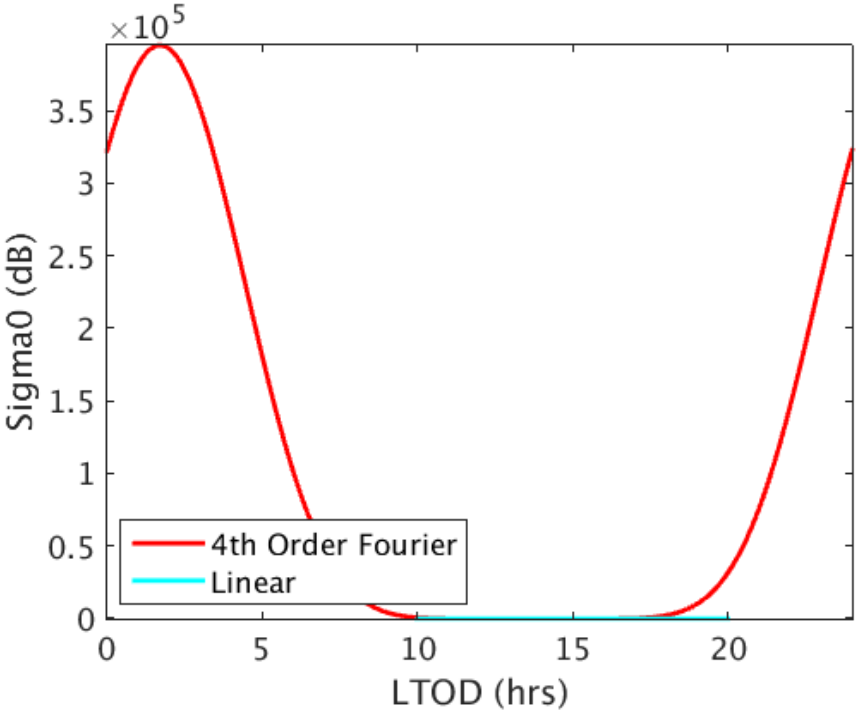

Figure 3.21: Zoomed-out version of Fig. 3.19. Note that the range of σ^0 values covered by the model is far larger than any possible value of σ from RapidScat.

model is effective at modeling narrow ranges of LTOD, when a full 24 hours is not available. Coefficients from least-square models are used as metrics in this thesis because they measure how much the models change from adjustments made to σ^0. The desired end result is to have models with minimal variability caused by certain parameters in order to enable accurate SIR image reconstruction.

The coefficients A_1 and A_2 are used to create a metric for the effectiveness of normalization of σ^0 dependence on incidence angle and LTOD. The metric

$$A = \max\{|A_1|, |A_2|\}. \tag{3.9}$$

This metric A is a rough estimate of maximum deviation away from the mean of the model estimate. The closer A is to zero, the more the σ^0 dependence on LTOD is normalized.

3.5.3 Sampling Distribution of LTOD

The sampling distribution of LTOD values is now considered. A near-uniform distribution of LTOD values helps to ensure an accurate least squares model estimate.

Fig. 3.22 shows the range of LTOD values over the first five months of the year in 2016. This figure shows a fairly uniform distribution of LTOD values for the creation of the model in Fig. 3.17. Since LTOD is periodic over 24 hours, it takes a full range of 24 hours to estimate an accurate model of LTOD. RapidScat requires around two months to measure values over a full 24 hours of LTOD. For day ranges less than two months, smaller ranges of LTOD are measured.

Fig. 3.23 shows the range of LTOD values in the ascending passes for six consecutive days over the Amazon mask. Over six days, the data is measured at a total range of LTOD close to 3.5 hours. Two standard deviations of this data covers a range close to 1.5 hours. SIR images are typically made with only 4 days of data or less, and an even smaller range of LTOD values is observed over that time. The range of LTOD values in this day range is a small enough to make LTOD effects relatively small, since it is less than 4 hours. As seen in Fig. 3.20, the change over 4 hours or less can be modeled by a first-order polynomial model.

Fig 3.24 shows the sampling distribution for a six day range, including both ascending and descending passes. This figure demonstrates two disjoint sets of LTOD measurements. As seen in

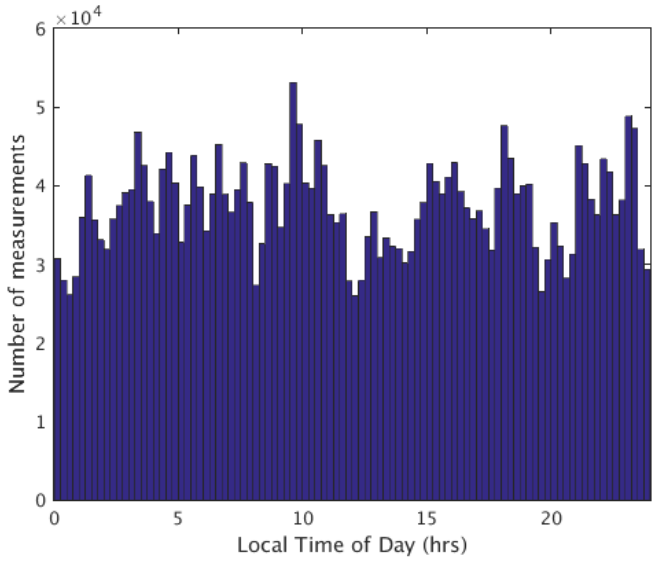

Figure 3.22: Histogram of LTOD over the first 5 months of 2016, the data used to create Fig. 3.17. The distribution of LTOD values is nearly uniform, with every LTOD value having a significant number of measurements to ensure an accurate least squares model.

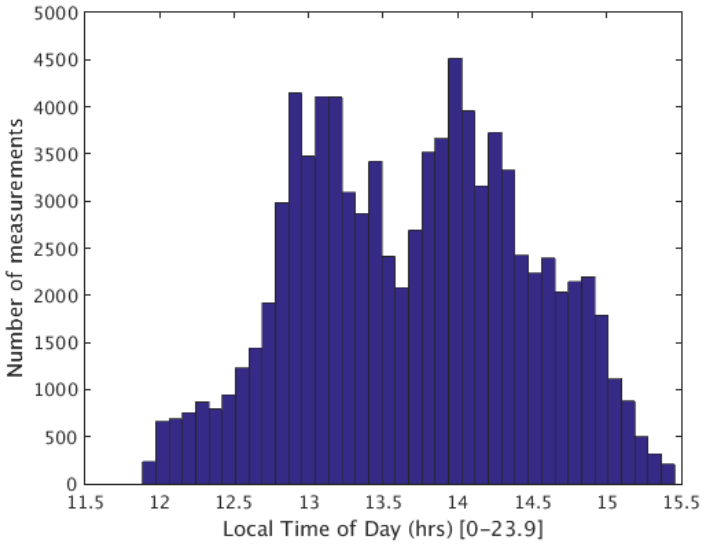

Figure 3.23: Histogram of LTOD in a range of 6 days, for ascending passes only. In this histogram, two standard deviations is a range of 1.5 hours and the full range is close to 3.5 hours. From days 100–105, 2015.

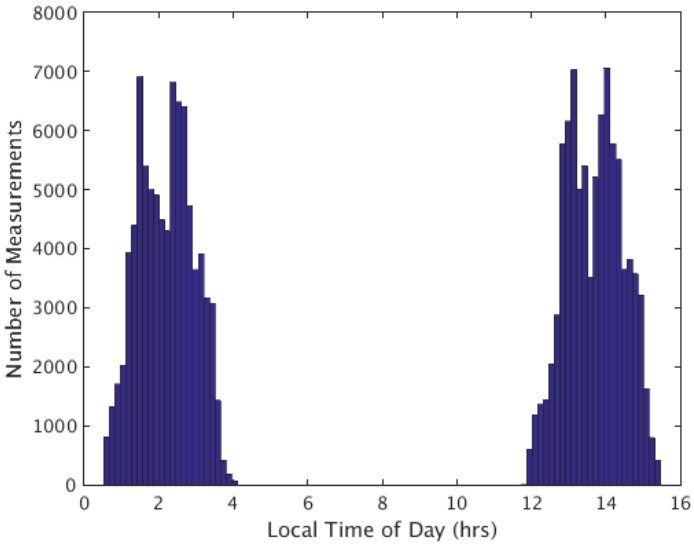

Figure 3.24: Histogram of LTOD in a range of 6 days, for both ascending and descending passes. Note the presence of two disjoint ranges of LTOD values that are nearly 12 hours apart. Both ranges of values have a similar sampling distribution (as in Fig. 3.23). From days 100–105, 2015.

Fig. 3.18, there is a need for a piecewise linear fit with a different model for each disjoint set in this case.

3.5.4 LTOD Model Summary

In summary, σ^0 dependence on LTOD is modeled as a fourth-order Fourier series, except when any disjoint range of LTOD values is shorter than four hours. LTOD samples are uniform over two months or more, but they are not for shorter day ranges. A first-order polynomial is used to model dependence for these shorter day ranges. Though the sampling distribution is not uniform for shorter day ranges, there are a sufficient number of values in the central part of these ranges to enable an accurate linear fit. Also, a sinusoidal model of a single frequency is used to estimate a metric for σ^0 dependence on LTOD.

3.6 Azimuth Angle Model

For azimuth angle modeling, QuikSCAT, RapidScat, and Oscat are used to compare dependence of σ^0 on azimuth angle for different Ku-band pencil beam scatterometers (see Fig. 3.25).

QuikSCAT data has a relatively flat dependence, compared to the other scatterometers, while RapidScat shows minor aberrations. Oscat has significant deviations from a flat response (for unknown reasons). Because of its similarity to QuikSCAT, RapidScat is expected to have a flat response, with minor aberrations. Since the RapidScat data exhibits relatively flat behavior (compared to Oscat), no normalization procedure is necessary for RapidScat dependence on azimuth angle. Although RapidScat σ^0 dependence on azimuth angle is not perfectly flat, the variations from the mean are much smaller than 0.1 dB, so they are considered insignificant.

However, a decrease in this variability in azimuth angle is an improvement. To verify that RapidScat variability in azimuth angle is reduced or maintained, it is used as a metric during other normalization procedures. A sinusoidal fit is used to test how much the RapidScat data deviates from a normalized (i.e., flat) dependence. The metric model

$$\begin{aligned} f(\phi) &= K_\phi + A_1\cos(\phi\omega) + A_2\sin(\phi\omega) \\ &= [\,\mathbf{1} \mid \cos(\phi\omega) \mid \sin(\phi\omega)\,][\,K_\phi\ A_1\ A_2\,]^\top \\ &= \mathbf{H}_\phi \mathbf{c}_\phi, \end{aligned} \tag{3.10}$$

where $\omega = \frac{2\pi}{360}$ to ensure a period of 360 degrees; ϕ is a column vector of azimuth angle values from RapidScat; $\mathbf{1}$ is a column vector of ones; K_ϕ, A_1, and A_2 are the coefficients of the model; $\mathbf{H}_\phi$ is the observation matrix for azimuth angle; and $\mathbf{c}_\phi$ is the vector of coefficients.

The coefficients A_1 and A_2 are used to create a metric for the effectiveness of normalization of σ^0 dependence on incidence angle and LTOD. The metric

$$A = \max\{|A_1|, |A_2|\}. \tag{3.11}$$

This metric A is a rough estimate of maximum deviation away from the mean of the model estimate. The closer A is to zero, the more σ^0 dependence on azimuth angle is normalized.

3.7 Roll Angle Model

Since RapidScat σ^0 errors are influenced by variations in the ISS attitude, the relationship between the attitude and changes to σ^0 values is significant. When plotting the roll angle of the ISS

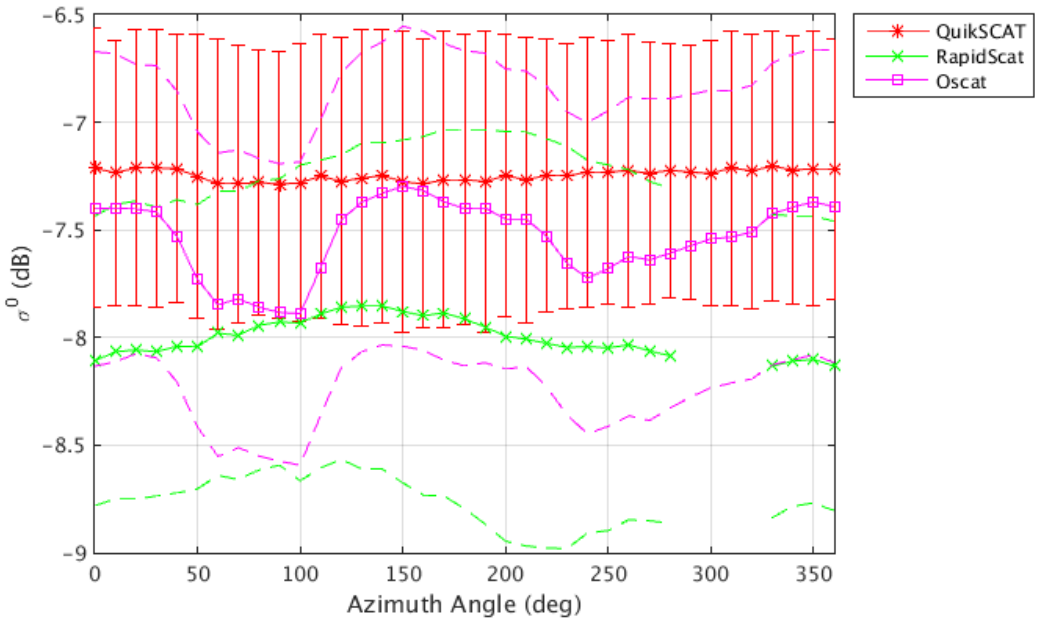

Figure 3.25: Mean and standard deviation for σ^0 versus azimuth angle for RapidScat, QuikSCAT, and Oscat. The symbols in the legend represent the mean of the data, and the dotted lines (for RapidScat and Oscat) and bars (for QuikSCAT) represent the standard deviation. QuikSCAT has a deviation from the mean σ^0 that is relatively small ($\pm$0.02 dB), and RapidScat data has a slightly larger deviation.

with the incidence angle of the RapidScat measurements over four revolutions around the earth, a direct correlation between the roll angle and the range of incidence angle values is apparent (see Fig. 3.26). Additionally, incidence angle values are found to change linearly across the physical measurement swath on the ground during a single pass (see Fig. 3.11). Comparing incidence angle changes with the pitch and yaw of the ISS did not yield any clear correlations. These results suggest that the roll angle is the principle factor causing incidence angle variation. Although pitch does not contribute directly to σ^0 variation, it is a variable that demonstrates some correlation to σ^0 variation (see Fig. 3.2). Therefore, σ^0 dependence on both roll and pitch angles are used as metrics to determine how effective normalization of σ^0 dependence on incidence angel and LTOD is.

Fig. 3.1 shows the dependence of σ^0 on roll angle measured by RapidScat over the Amazon for the first five months of the year. This figure demonstrates that σ^0 values are highly correlated with changes in the roll angle, mostly likely because of the relationship between the roll and

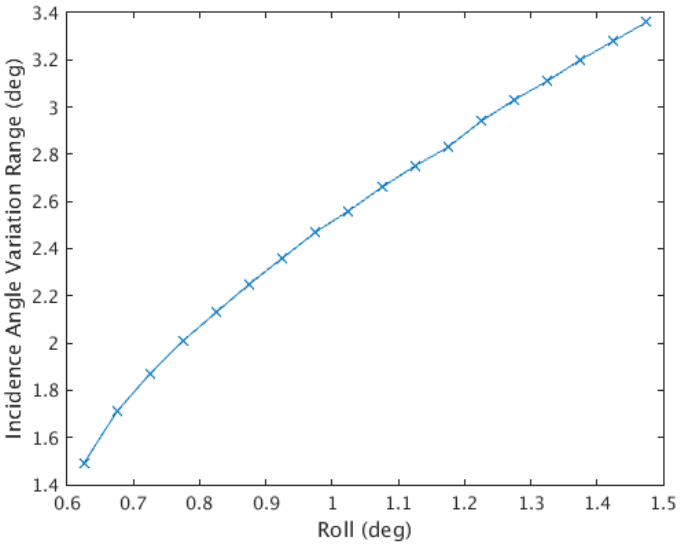

Figure 3.26: Plot of the maximum range of incidence angle variation as a function of roll angle for four consecutive orbit revolutions. There is a direct correlation between the increase of the roll angle and the increase in the maximum range of incidence angle variations.

incidence angle changes. Dependence on roll angle cannot be compared with other scatterometers, since these attitude variations are not as prominent for them. Because of this uncertainty, only a first-order polynomial is used to model σ^0 dependence on roll angle. The model function

$$\begin{aligned} f(\varphi) &= K_\varphi \mathbf{1} + B\varphi \\ &= [\,\mathbf{1} \mid \varphi\,][\,K_\varphi\ B\,]^\top \\ &= \mathbf{H}_\varphi \mathbf{c}_\varphi, \end{aligned} \tag{3.12}$$

where φ is a column vector of RapidScat roll angle values; $\mathbf{1}$ is a column vector of ones; K_φ and B are the coefficients of the model, and $\mathbf{H}_\varphi$ is the observation matrix for roll angle; and $\mathbf{c}_\varphi$ is the vector of coefficients. The coefficient B is used as the metric. As the magnitude of B (the slope) gets closer to zero, the more normalized σ^0 dependence on roll angle is.

3.8 Pitch Angle Model

The metric model for σ^0 dependence on pitch angle is linear, as for roll angle, since the dependence of σ^0 on pitch is uncertain. The model function

$$\begin{aligned} f(\psi) &= K_\psi \mathbf{1} + B\psi \\ &= [\ \mathbf{1} \mid \psi\ ][\ K_\psi\ B\ ]^\top \\ &= \mathbf{H}_\psi \mathbf{c}_\psi, \end{aligned} \tag{3.13}$$

where ψ is a column vector of RapidScat pitch angle values, $\mathbf{1}$ is a column vector of ones, K_ψ and B are the coefficients of the model, $\mathbf{H}_\psi$ is the observation matrix, and $\mathbf{c}_\psi$ is a column vector of the coefficients. The coefficient B is used as the metric. As the magnitude of B decreases, the dependence of σ^0 on pitch angle is more normalized.

3.9 Multidimensional Model

A multidimensional model can be used for normalization. Two main options are considered here: normalizing just incidence angle and LTOD, or normalizing all significant parameters. The model function for coupled incidence angle and LTOD is

$$\begin{aligned} f(\theta,\tau) &= K_{\theta\tau} + B_\theta \theta + \sum_{i=1}^{4} A_i \cos(i\tau\omega) + B_i \sin(i\tau\omega) \\ &= \begin{bmatrix} 1 & \theta_1 & \cos(1\tau_1\omega) & \sin(1\tau_1\omega) & \dots & \cos(4\tau_1\omega) & \sin(4\tau_1\omega) \\ 1 & \theta_2 & \cos(1\tau_2\omega) & \sin(1\tau_2\omega) & \dots & \cos(4\tau_2\omega) & \sin(4\tau_2\omega) \\ \vdots & \vdots & \vdots & & \vdots & \vdots & \\ 1 & \theta_N & \cos(1\tau_N\omega) & \sin(1\tau_N\omega) & \dots & \cos(4\tau_N\omega) & \sin(4\tau_N\omega) \end{bmatrix} \begin{bmatrix} K_\tau \\ B_\theta \\ A_1 \\ B_1 \\ \vdots \\ A_4 \\ B_4 \end{bmatrix} \\ &= \mathbf{H}_{\theta\tau} \mathbf{c}_{\theta\tau}, \end{aligned} \tag{3.14}$$

where θ is a vector of RapidScat incidence angle values; θ_i is a specific incidence angle value from this vector of values; $\omega = \frac{2\pi}{24}$ to create a model with a period of 24 hours; τ is a vector of RapidScat LTOD values; τ_i is a specific LTOD value from this vector of values; N is the number of values in this vector; and where K_τ, B_θ, A_i, and B_i are the estimated coefficients of the model.

The coupled model for all the significant parameters considered is

$$\begin{aligned} f(\theta,\varphi,\psi,\phi,\tau) = K_{all} + B_\theta\theta + B_\varphi\varphi + B_\psi\psi + A_\phi\cos(\phi\omega_\phi) + B_\phi\sin(\phi\omega_\phi) \\ + \sum_{i=1}^{4} A_i\cos(i\tau\omega_\tau) + B_i\sin(i\tau\omega_\tau) \\ = \mathbf{H}_{all}\mathbf{c}_{all}, \end{aligned} \tag{3.15}$$

where

$$\mathbf{H}_{all} = \begin{bmatrix} 1 & \theta_1 & \varphi_1 & \psi_1 & \cos(\phi_1\omega_{phi}) & \sin(\phi_1\omega_\phi) & \cos(i\tau_1\omega_\tau) & \sin(i\tau_1\omega_\tau) \\ 1 & \theta_2 & \varphi_2 & \psi_2 & \cos(\phi_2\omega_{phi}) & \sin(\phi_2\omega_\phi) & \cos(i\tau_2\omega_\tau) & \sin(i\tau_2\omega_\tau) \\ \vdots & \vdots & \vdots & \vdots & & \vdots & \vdots & \vdots \\ 1 & \theta_N & \varphi_N & \psi_N & \cos(\phi_N\omega_{phi}) & \sin(\phi_N\omega_\phi) & \cos(i\tau_N\omega_\tau) & \sin(i\tau_N\omega_\tau) \end{bmatrix} \tag{3.16}$$

and

$$\mathbf{c}_{all} = \begin{bmatrix} K_{all} & B_\theta & B_\varphi & B_\psi & A_\phi & B_\phi & A_i & B_i \end{bmatrix}^\top, \tag{3.17}$$

where $i = 1,2,3,4$ (meaning there are eight columns for LTOD in $\mathbf{H}_{all}$ and there are eight coefficients associated with LTOD in $\mathbf{c}_{all}$). In the above equations, θ is a vector of RapidScat incidence angle values; θ_i is a specific incidence angle value from this vector of values; φ is a vector of roll angle values; φ_i is a specific roll angle value from the vector; ψ is a vector of pitch angle values; ψ_i is a specific pitch angle value from the vector; $\omega_\phi = \frac{2\pi}{360}$ to create a model with a period of 360°; ϕ is a vector of azimuth angle values; ϕ_i is a specific azimuth angle value from the vector; $\omega_\tau = \frac{2\pi}{24}$ to create a model with a period of 24 hours; τ is a vector of LTOD values; τ_i is a specific LTOD value from the vector; N is the number of values in the vectors; and where K_{all}, B_θ, B_φ, B_ψ, A_ϕ, B_ϕ, A_i, and B_i are the estimated coefficients of the model.

These two coupled models can be used to normalize σ^0 on these parameters. However, the coupled models were empirically found to not be as effective as the sequential models. Thus a detailed analysis of the coupled models is not provided in this thesis.

3.10 Chapter Summary

Examples of the models used for RapidScat σ^0 dependence normalization is shown in Fig. 3.27. Since incidence angle and LTOD are the parameters that directly affect the value of σ^0 measurements, only these parameters are used for normalization. A linear fit is used for σ^0 dependence on incidence angle, and a fourth-order Fourier series is used for σ^0 dependence on LTOD when the range of LTOD values covers a range larger than 4 hrs or more. If less than 4 hours of LTOD are covered in any disjoint range, a linear fit is used for normalization.

An example of the models used for metrics of σ^0 normalization is shown in Fig. 3.28. The σ^0 dependence on all the significant parameters (roll angle, pitch angle, incidence angle, azimuth angle, and LTOD) are modeled to create metrics for the effectiveness of σ^0 adjustments. After σ^0 is adjusted and its dependence on incidence angle and LTOD is normalized, metrics that are closer to zero are better. For roll angle, pitch angle, and incidence angle, the slope of the linear fit is the metric. For azimuth angle and LTOD (which are periodic), the max of the magnitude of the two sinusoidal coefficients of the sinusoidal fit is used.

In addition, examples of multidimensional models are presented, as seen in Eqs. 3.14 and 3.15. Though these models are not used to test the normalization procedure in the following chapters, a multidimensional approach can be pursued by future analysts to compare with the analysis in this thesis.

In the next chapter, the normalization procedure for reducing σ^0 dependence on undesired parameters is presented and analyzed. Estimating the correct models for σ^0 dependence on these parameters is essential for the normalization procedure presented.

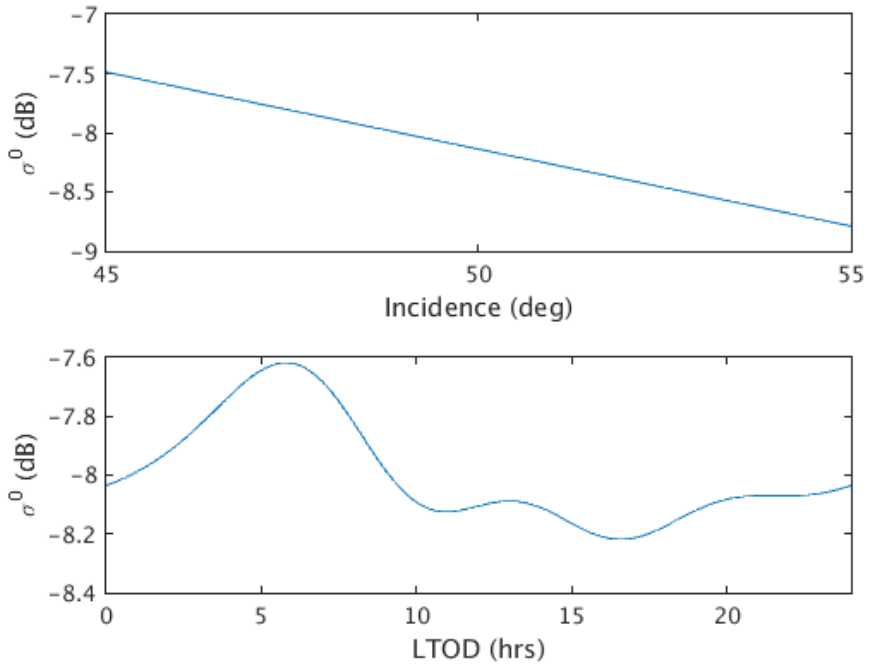

Figure 3.27: Examples of the models used for normalizing the σ^0 dependence on incidence angle and LTOD.

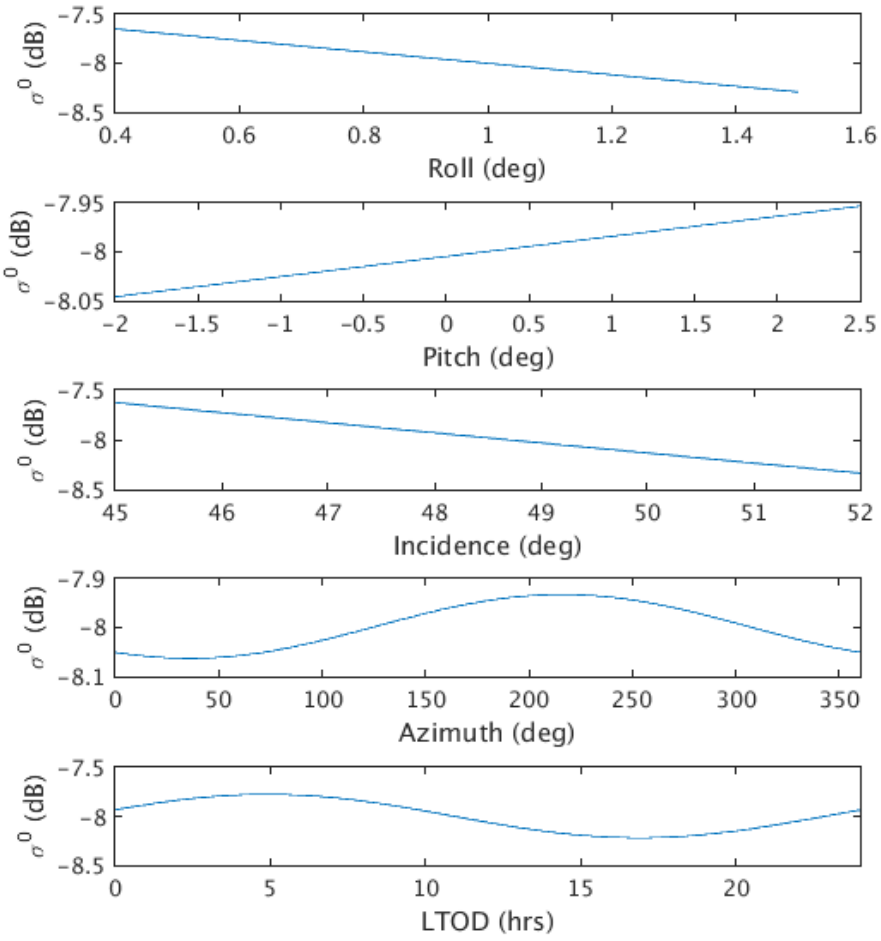

Figure 3.28: Examples of the models used as metrics for normalizing the σ^0 dependence on incidence angle and LTOD.

CHAPTER 4. NORMALIZATION PROCEDURE

The models from Chapter 3 are used in this chapter to compute adjustments to σ^0 values in order to remove undesired variation in σ^0. A normalization procedure is described that adjusts σ^0 values to remove or reduce the mean dependence of σ^0 on the significant parameters, which are incidence angle, azimuth angle, LTOD, roll angle, and pitch angle. A simulation is then demonstrated to show the functionality of this procedure for RapidScat data.

4.1 Procedure

Normalizing the undesired effect of a parameter on σ^0 is done by adjusting the mean of σ^0 to be constant across the parameter range. The adjusted σ^0 mean is the mean σ^0 value at a single nominal parameter value. This normalization is computed by subtracting a model function from a scalar nominal σ^0 value and adding the difference to the backscatter measurements. The adjusted σ^0 values

$$\sigma^0_{adj} = \sigma^0 + [f(x_{nom}) - f(\mathbf{x})], \tag{4.1}$$

where σ^0_{adj} represents a vector of the adjusted backscatter values, σ^0 represents a vector of the original backscatter measurements, $f(x_{nom})$ represents the value of the σ^0 model at a nominal parameter value x_{nom}, and $f(\mathbf{x})$ is the model of mean σ^0 dependence on a given parameter vector $\mathbf{x}$. Figs. 4.1, 4.2, and 4.3 show an example of how this normalization procedure is applied in the case of σ^0 dependence on incidence angle. This normalization procedure is performed for backscatter measurements in a SIR setup file, using models estimated from these setup file measurements. A SIR setup file contains L1B measurements that are organized according to their affected pixel locations. The adjusted σ^0 values are written to a new setup file, from which a SIR image is created. Two RapidScat SIR images are produced for comparison in this chapter. One is made from the original setup file, and the second one is made from the setup file with adjusted σ^0 measurements.

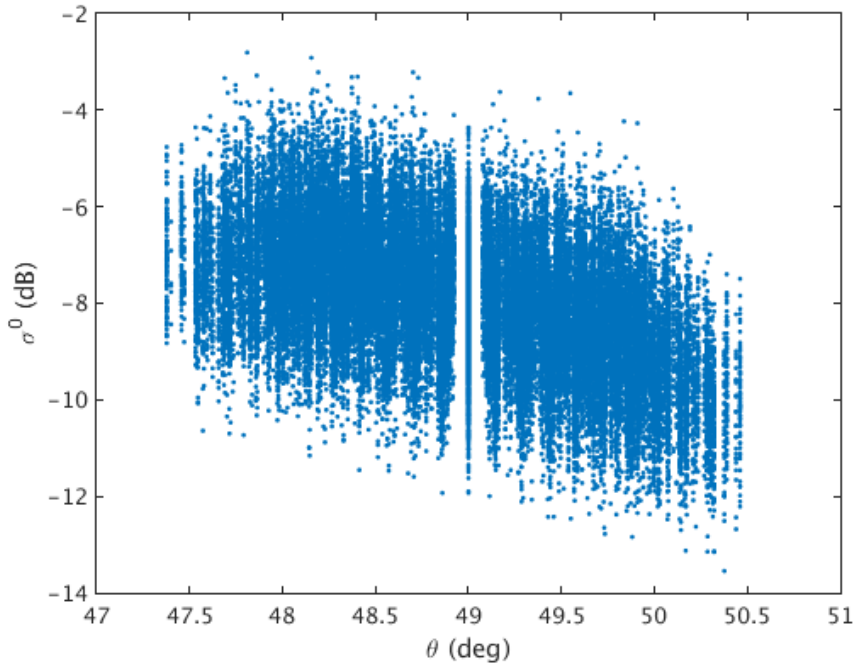

Figure 4.1: Example of σ^0 dependence on a parameter (θ, or incidence angle, in this case). The purpose of the normalization procedure is to remove this dependence by changing the mean dependence to have a slope close to zero. Plot made from simulated data. The gap around $\theta = 49°$ is inserted to emphasize the nominal parameter value.

SIR images are also made for QuikSCAT data over the same time range for additional comparison, since QuikSCAT SIR images typically have very low noise.

Normalization of σ^0 values alters the coefficients of the models of σ^0 dependence on each parameter. In order to normalize the mean σ^0 values to be constant across the parameter range, σ^0 values are normalized consecutively. The coefficients for a new model of σ^0 dependence are estimated from the adjusted σ^0 data before using the new model to normalize σ^0 dependence on a new parameter. To do this consecutive adjustment, the adjusted σ^0

$$\begin{aligned} \sigma^0_{i,adj} &= \sigma^0_{i-1,adj} + [f_i(x_{i,nom}) - f_i(\mathbf{x}_i)] \\ \sigma^0_{i+1,adj} &= \sigma^0_{i,adj} + [f_{i+1}(x_{i+1,nom}) - f_{i+1}(\mathbf{x}_{i+1})], \end{aligned} \tag{4.2}$$

where $f_i(\mathbf{x}_i) = \mathbf{P}_{\mathrm{H}_i}\sigma^0_{i-1,adj} = \mathbf{H}_i(\mathbf{H}_i^\top\mathbf{H}_i)^{-1}\mathbf{H}_i^\top\sigma^0_{i-1,adj}$ is the model for σ^0 dependence on the current parameter, after the previous σ^0 adjustment; $f_i(x_{i,nom})$ is the value of the model of σ^0 dependence at a nominal parameter value $x_{i,nom}$ in the current parameter vector $\mathbf{x}_i$; and $\sigma^0_{i,adj}$

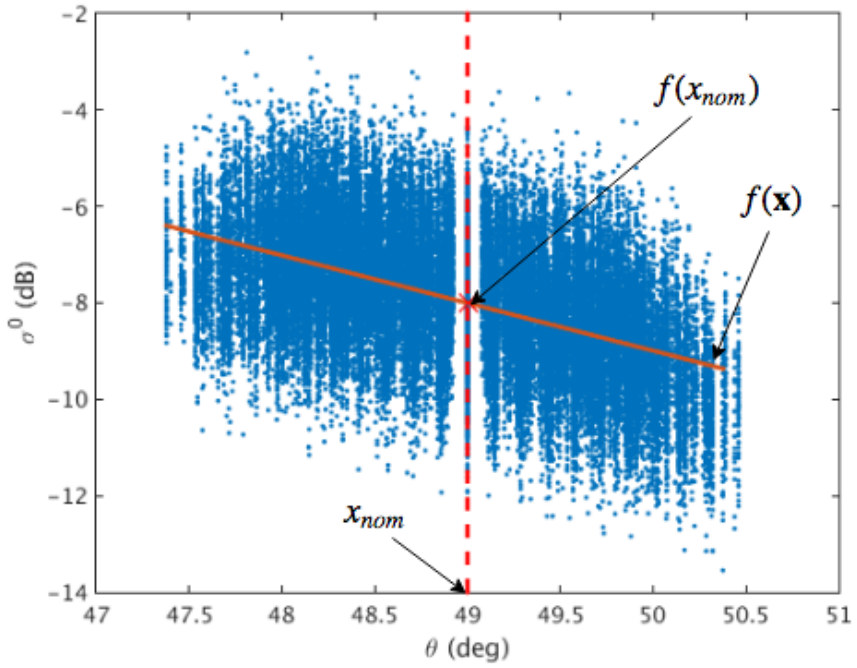

Figure 4.2: Example of the normalization calculation in Eq. (4.1). The function $f(\mathbf{x})$ represents the mean dependence of σ^0 on the parameter vector (θ, or incidence angle, in this case). The value $f(x_{nom})$ is the nominal value that σ^0 is adjusted to match. The value x_{nom} is the parameter value where $f(\mathbf{x})$ is evaluated to determine the nominal σ^0 value.

represents the vector of σ^0 values for the next iteration. For the first iteration, $\sigma^0_{i-1,adj}$ is the original σ^0 vector σ^0. Fig. 4.4 shows a block diagram of this consecutive normalization approach.

The criterion for how the nominal value is chosen depends on the parameter. For incidence angle, the nominal value chosen is 49° for the inner beam. This value is chosen because 49° is the designed incidence angle for the inner beam of RapidScat. For LTOD, any time of day can be chosen. Most scatterometers have two particular LTODs that they measure a given location at. Using a model for RapidScat σ^0 dependence on LTOD over a full 24 hours can be used to adjust all scatterometers to be normalized to the same effective LTOD value. A good choice for this value is 6 am over the equator over the Amazon, since this is one of the LTODs that QuikSCAT data is measured at.

The effectiveness of normalization procedures can be measured by estimating models of σ^0 dependence on every significant parameter for each normalization iteration (see Chapter 3 for more details). First-order polynomial models are used for incidence angle, roll angle, and pitch angle for

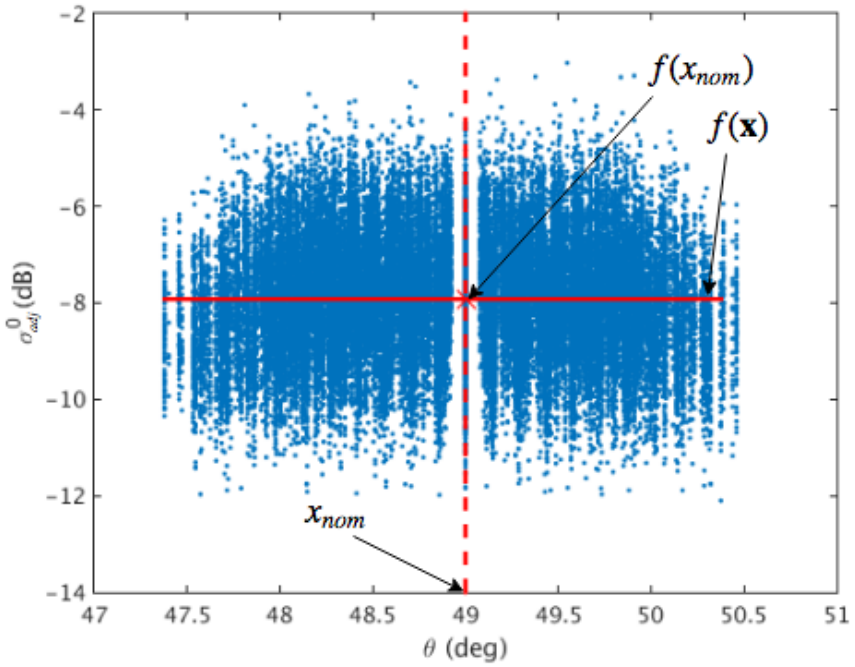

Figure 4.3: Example of the resulting σ_{adj} dependence on the parameter vector after the normalization procedure (see Eq. 4.1). Note that the mean model function $f(\mathbf{x})$ now has a slope with a small magnitude, and mean σ^0 values match the model function at the nominal value $f(x_{nom})$.

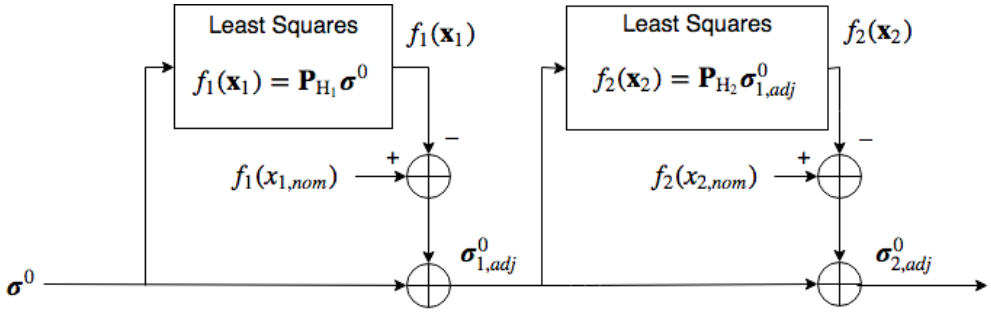

Figure 4.4: Block diagram of the consecutive normalization procedure shown in Eq. (4.2). The dependence of σ^0 is normalized for one parameter, and then the adjusted σ^0 values are used to estimate a model of the adjusted σ^0 dependence on another parameter.

Table 4.1: The mean and variance of σ^0 during the consecutive steps of the normalization procedure example shown in Figs. 4.5, 4.6, and 4.7.

Step	Mean	Variance
1) Original σ^0 (Fig. 4.5)	-7.995	0.610
2) After LTOD Normalization (Fig. 4.6)	-8.088	0.578
3) After Incidence Normalization (Fig. 4.7)	-7.999	0.561

checking the results of normalization, and the magnitude of the slope of these dependence models is used as a metric for the effectiveness of the procedure. First-order sinusoidal models are used for LTOD and azimuth angle for checking the results of normalization, and the maximum magnitude of the two sinusoidal coefficients are used as a metric for the effectiveness of the procedure.

An example of a consecutive normalization procedure is shown in Figs. 4.5, 4.6, and 4.7, where σ^0 dependence on LTOD is normalized first, and then dependence on incidence angle is normalized. Fig. 4.5 is the original data, Fig. 4.6 is the data after dependence on LTOD is normalized, and Fig. 4.7 is the data after dependence on incidence angle is normalized. Note that after the normalization procedure, the model functions in this example all have metrics that are small or significantly less than the original (compare Fig. 4.5 and 4.7). Note that whichever dependence model is normalized last tends to have better results. In this case, dependence on LTOD is better in Fig. 4.6 than in Fig. 4.7, since LTOD is normalized first. Also, the dependence on incidence angle is better in Fig. 4.7 because incidence angle is normalized last. The results of the effect of this normalization on the variance is summarized in Table 4.1. Note that the variance decreases with each normalization step, which suggests that the overall variability in the measurements is reduced.

This normalization procedure is applied to RapidScat data to remove incidence angle and LTOD variations to σ^0 in a simulation in the next section. This simulation demonstrates the effectiveness of this approach with the assumptions made about RapidScat σ^0 variations.

4.1.1 Multidimensional Considerations

Multidimensional models can also be used for this normalization procedure. Since each dependence model is known to be dependent on each other, using a coupled model with each significant parameter included could potentially remove dependence better than a consecutive ap-

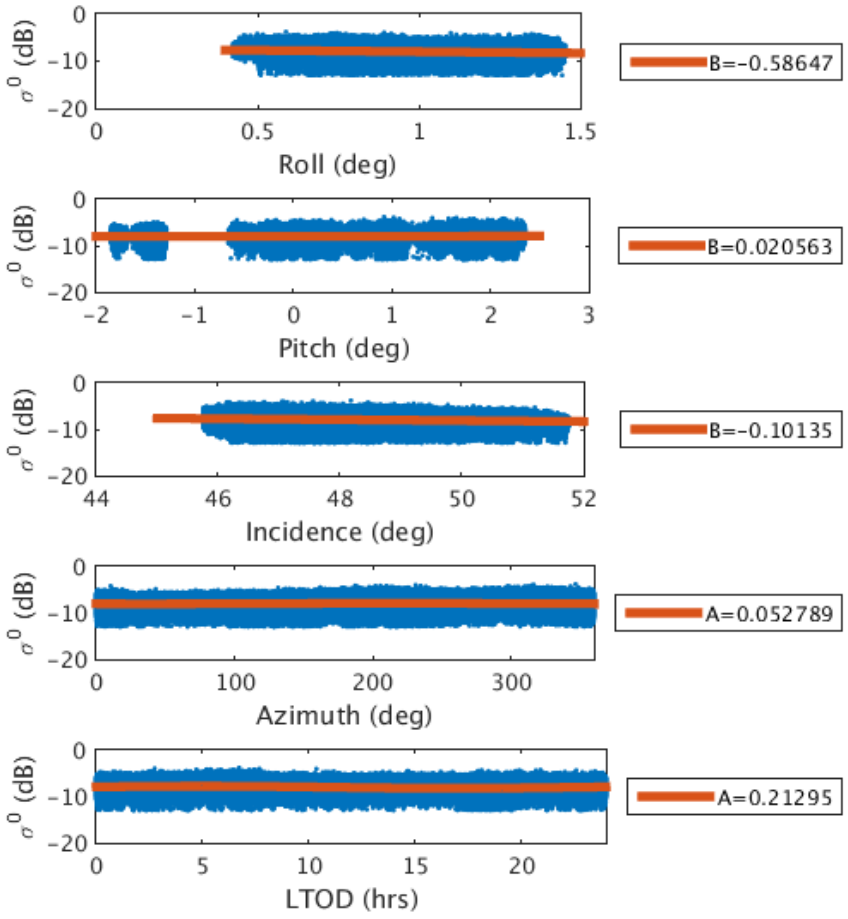

Figure 4.5: Plots of the metric models for the original σ^0 dependence on roll angle, pitch angle, incidence angle, azimuth angle, and LTOD. This is the first time step of the example normalization procedure. The *A* or *B* value for each plot is a metric for the effectiveness of the normalization procedure. From days 1-151, 2015 over the Amazon mask. The letter *B* is the coefficient representing the slope of a first-order polynomial fit. The letter *A* is the maximum magnitude of the sinusoidal coefficients of a first-order sinusoidal fit (see Chapter 3).

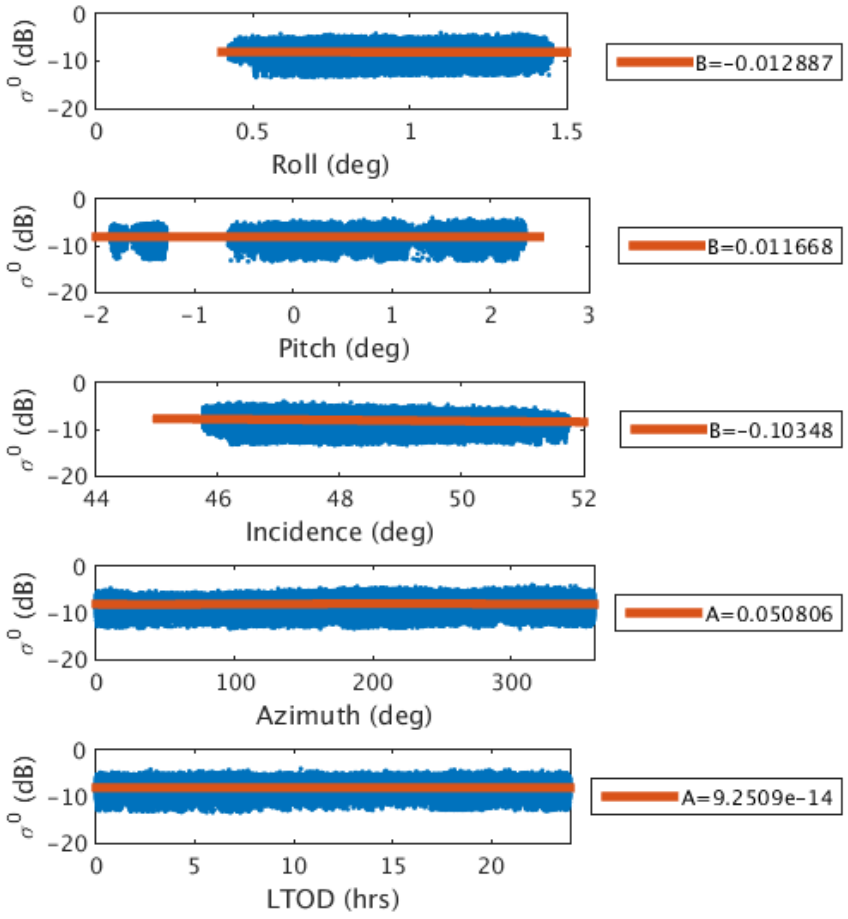

Figure 4.6: Plots of the metric models estimated from adjusted σ^0 values after σ^0 dependence on LTOD is normalized based on a fourth-order Fourier series model. This is the second time step of the example normalization procedure. Note that the magnitude of the metric for dependence on LTOD is close to zero and that the slope of σ^0 dependence on roll angle is significantly reduced to -0.01 dB/deg. This suggests a significant dependence between the dependence of σ^0 on roll angle and LTOD. The metrics for σ^0 dependence on other parameters are reduced to some degree, except for incidence angle (compare with Fig. 4.5).

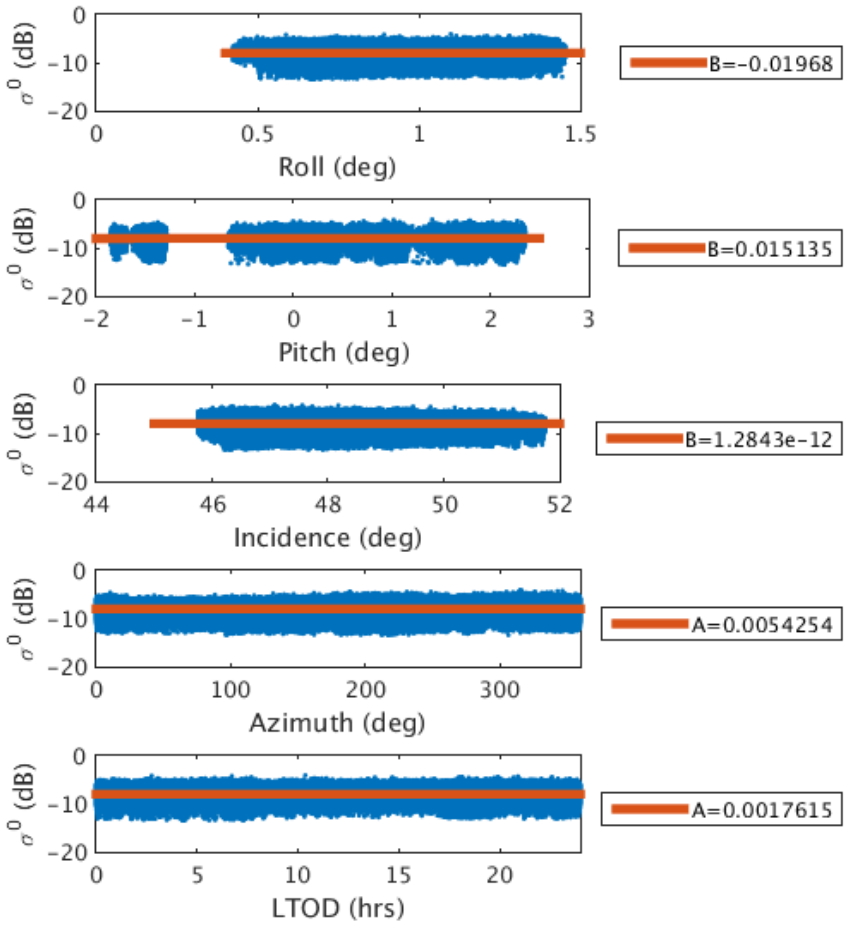

Figure 4.7: Plots of the metric models estimated from adjusted σ^0 values after σ^0 dependence on incidence angle is normalized. This is the final time step of the normalization procedure. The metrics for all parameters have been reduced significantly, compared to Fig. 4.5, although the metric for LTOD is worse than in Fig. 4.6. The metric for dependence on incidence angle is the smallest because it is normalized last.

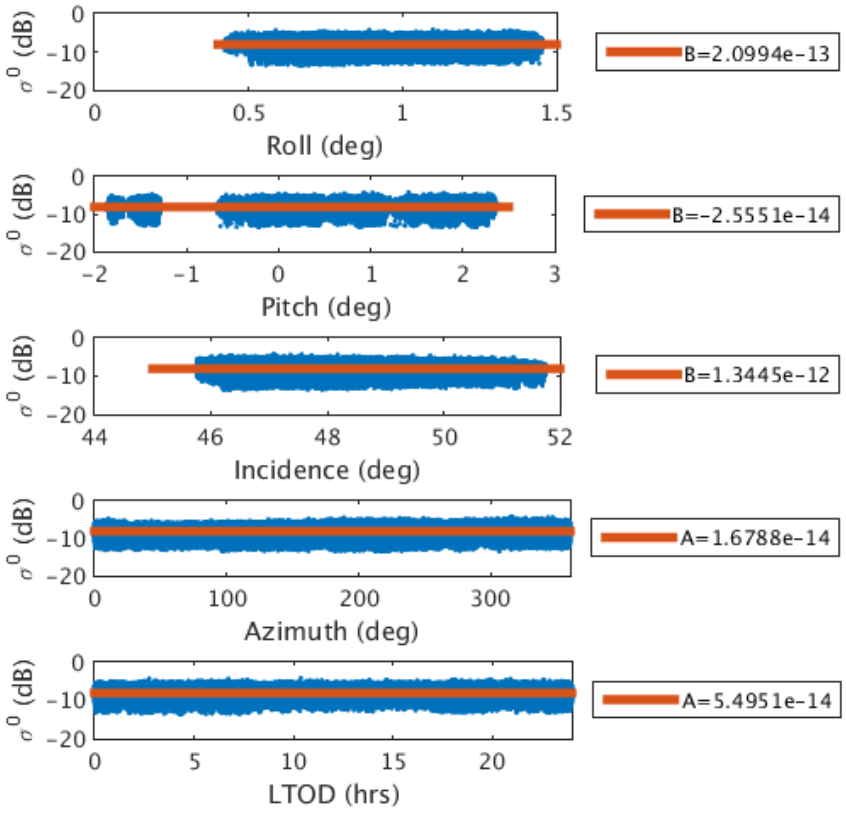

Figure 4.8: The results of applying a multidimensional model (see Eq. 3.15) with a single step of the normalization procedure. Note that the slope is minimal for every significant parameter the affects the variability of σ^0.

proach. Empirical testing suggested that this did not do as well as the consecutive approach taken in this thesis. Since incidence angle and LTOD are the principle parameters that directly effect σ^0 values in a physical sense, only these parameters are used for the normalization procedure. Future experiments may analyze the difference between multidimensional normalization and consecutive normalization in more detail.

The results of a multidimensional normalization is seen in Fig. 4.8. This figure shows that a multidimensional normalization may be more effective at reducing σ^0 variability. However, this adjustment may introduce more variability into the measurements, since it is only incidence angle and LTOD that physically affect σ^0 values directly. This approach can be examined by future analysts.

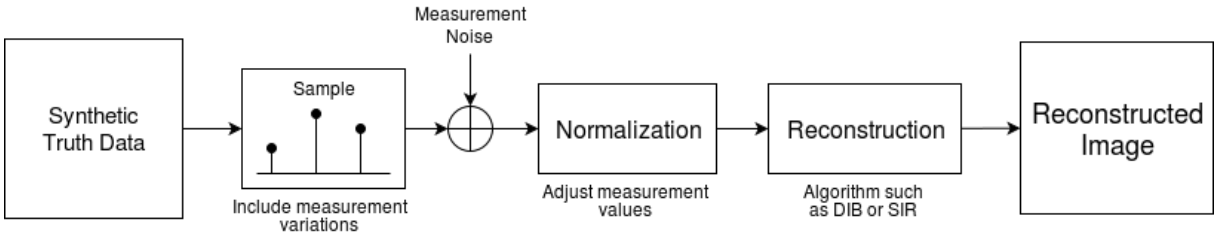

Figure 4.9: The simulation process.

4.2 Simulation

In order to test the effectiveness of the proposed normalization algorithm for RapidScat σ^0 measurements, a simulation is created. This simulation demonstrates the effectiveness of the algorithm, and it identifies some of the strengths and weaknesses of the algorithm.

The simulation represents the radar measurement process. This measurement process begins with a synthetic radar system that measures synthetic truth data in a measurement region on an extended surface (including receiver noise). Then these measurements are adjusted by a normalization procedure, and then the normalized measurements are used to reconstruct an estimate of the original truth data (with an algorithm such as drop-in-the-bucket or SIR) and create a corresponding image of the measurements on the ground. See Fig. 4.9 for a visual representation of this simulation process. The drop-in-the-bucket algorithm (DIB) reconstructs images by averaging together all σ^0 measurements that are located within a given pixel. Within the assumptions made for this particular simulation, SIR and DIB are equivalent algorithms. The synthetic radar system in this simulation mimics σ^0 measurement variations expected in the RapidScat system. This system mimics changes to backscatter measurements caused by incidence angle variations and different local times of day (LTODs) for measurements in the same location. Two different measurement scenarios are used in this simulation to test the effectiveness of the normalization algorithm in restoring the original data. The resulting image at the end of the simulation is used to compare the normalized measurements with the truth data at every location in the measurement region and to show how the normalization procedure improves a radar image.

In the simulation, the synthetic truth data represents a region with homogeneous land features to simulate the Amazon rainforest. This region has a mean of -8 dB and a standard deviation of 1 dB, to mimic the Amazon rainforest, with some variation in the vegetation. This truth data is

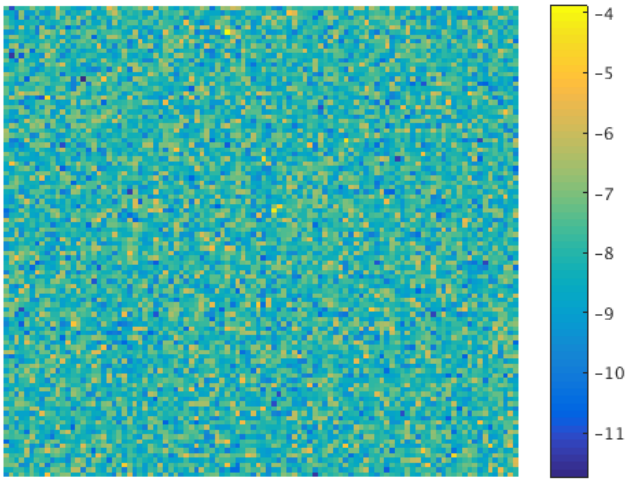

Figure 4.10: Ideal reconstructed image of the synthetic truth values of σ^0. This image synthesizes a homogeneous land region, like the Amazon rainforest. Each pixel simulates an ideal antenna response pattern for that location.

represented by a constant, plus a normal random variable,

$$\sigma^0_{true}(x,y) = -8 + \nu(x,y) \;\; dB, \tag{4.3}$$

where $\nu \sim$ N[0,1] dB, and (x,y) is an ordered pair designating the location in the region in terms of antenna measurement bins. A 100-by-100 grid of these measurements is used for the simulation. An initial image is created in the simulation to visually represent this truth data at each antenna measurement location. In order to do this, the synthetic data is measured exactly, with no measurement variation or noise added. The synthetic truth data represents the average backscatter over a simplified rectangular antenna response pattern, and pixels in the final reconstructed image of the simulation use pixel sizes that are the exact same dimensions as the antenna response function. Therefore, a DIB reconstruction exactly reproduces the truth data of the measurement region when there are no errors in the measurement or reconstruction process. This image of the truth data can be seen in Fig. 4.10.

Two simulation scenarios are considered. The first scenario simulates a simple measurement scheme, where measurement swaths are vertically oriented. The second scenario simulates

a more involved measurement scheme, where measurement swaths are diagonally oriented and where roll angle effects on incidence angle are included. Three images are produced for each scenario: one without measurement errors or normalization, one without normalization, and one with both included. The first image is sampled and reconstructed after the first block in Fig. 4.9, the second image is reconstructed after the summing block, and the third image is the reconstructed image in the final block.

4.2.1 Simple Simulation Scenario

The first scenario considered in the simulation is a simple process to verify the feasibility of the calibration algorithm. The simulated RapidScat measurements are created where the swath width for each pass is modeled as being 5 measurement response patterns wide. Each pass is adjacent with no overlap. The incidence angle variation across the swath is simulated by a decrease to σ^0 as incidence angle values increase, where the incidence angle values increase from left to right across the swath width. The incidence angle is chosen to be 47° at the leftmost column of the swath and increases by one degree for each column, from left to right. This makes the center column 49°, which is the nominal value. The σ^0 values are simulated to decrease by 1 dB for each degree increase in incidence angle. The LTOD effect is modeled as a cosine with an amplitude of 1 dB and a period of 24 hours, centered around the mean, and the peak occurring at 12am. The whole measurement process in this scenario is

$$\sigma^0_{meas}(x,y,\theta,t) = \sigma^0_{true}(x,y) + (\theta_{nom} - \theta) + \cos\left(\frac{2\pi}{24}t\right) + n(x,y) \;\; dB, \tag{4.4}$$

where $\theta_{nom} = 49^\circ$, θ is the incidence angle, t is the LTOD, (x,y) is an ordered pair designating the pixel location of the measurement in the measurement region, and $n(x,y) \sim N[\mathbf{0}, \sigma^2\mathbf{I}]$ represents receiver noise for the radar measurement at each location, where $\sigma^2 = (0.1)^2$. Each swath varies in LTOD so that 24 hours of LTOD are covered across the entire measurement region. To create an image of the simulated measurements, the measurements are reconstructed into an image, without any normalization. An example of this image is shown in Fig. 4.11. The image illustrates the kind of errors that are caused by uncorrected RapidScat incidence angle and LTOD variations.

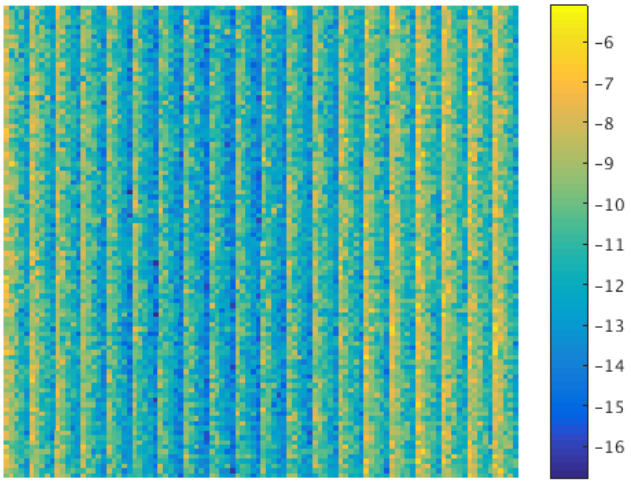

Figure 4.11: Reconstructed image of the unadjusted synthetic measurements of σ^0, showing variations caused by incidence angle and LTOD variations.

To normalize the σ^0 measurements, all the measurement values for each parameter are combined into separate vectors. A least-squares method is used to model the dependence of σ^0 on LTOD. This model is used to normalize the σ^0 measurements to have the same mean (the mean at a nominal LTOD value). Then a model is estimated for the dependence of σ^0 dependence on incidence angle, and the σ^0 measurements are normalized to the mean at a nominal incidence angle value. See Figs. 4.12, 4.13, 4.14, and 4.15 for a representation of these normalization steps. The normalized measurements are used to create a reconstructed image using the DIB method, and the resulting image can be seen in Fig. 4.16.

The results of the simulation for the first scenario can be seen in Table 4.2. The adjusted data image has minimal effects from incidence angle and LTOD variation remaining, and most of the residual error is from the instrument receiver noise (see Figs. 4.16, 4.17, and 4.18). Error is defined as the difference between the normalized image and the truth image (see Fig. 4.17 and 4.18). However, for normalization procedures that are calculated with actual data, no truth image can be generated, so the only difference image that can be generated is the difference between the unadjusted image, and the adjusted image (see Fig. 4.19). This difference does not represent the error of the image, but it shows a pattern of incidence angle and LTOD effects on σ^0. If this pattern appears in a difference image and the overall variance of the image decreases, it is assumed that

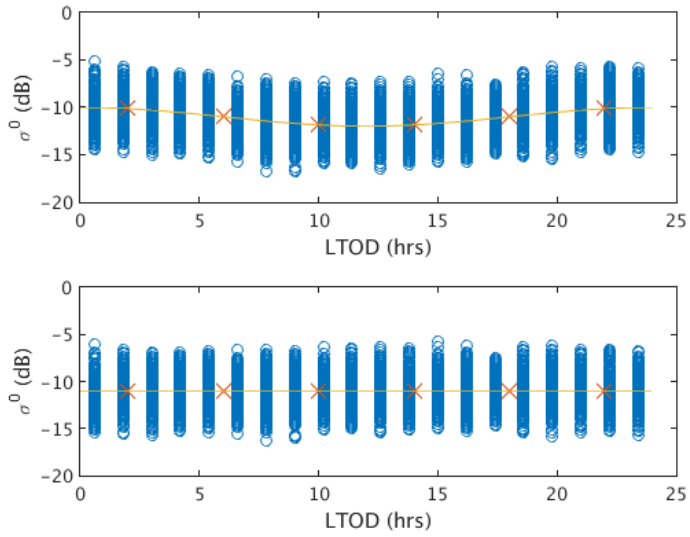

Figure 4.12: Plots representing the normalization procedure for σ^0 dependence on LTOD for the first simulation scenario. A least squares method is used to model σ^0 dependence on LTOD (top). Then all values at every LTOD bin are adjusted to have the same mean value as the nominal LTOD bin (bottom). The line in the middle of the data is the least squares fit of the data for each plot. The "X" marks are for the mean of the data at each of six different LTOD bins.

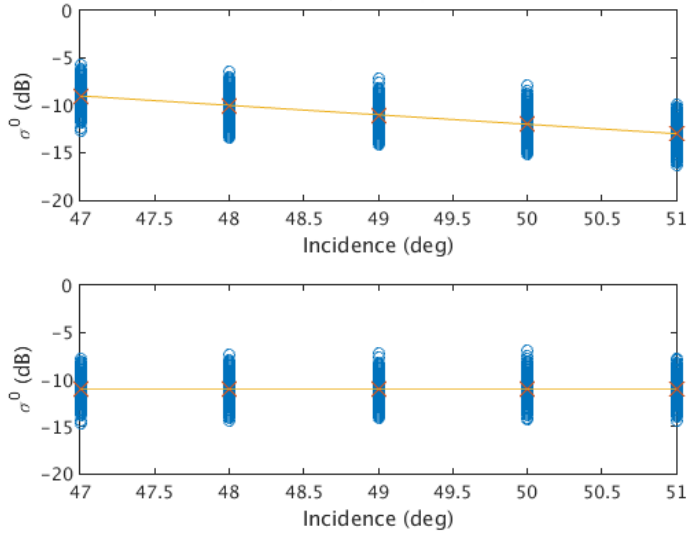

Figure 4.13: Plots representing the normalization procedure for σ^0 dependence on incidence angle for the first simulation scenario, after σ^0 dependence on LTOD is normalized, as in Fig. 4.12. A least squares method is used to model σ^0 dependence on incidence angle (top). Then all the values at each incidence angle bin are adjusted to have the same mean values as the nominal incidence angle bin (bottom). The line in the middle of the data is the least squares fit of the data for each plot. The "X" marks are for the mean of the data at each of five different incidence angle bins.

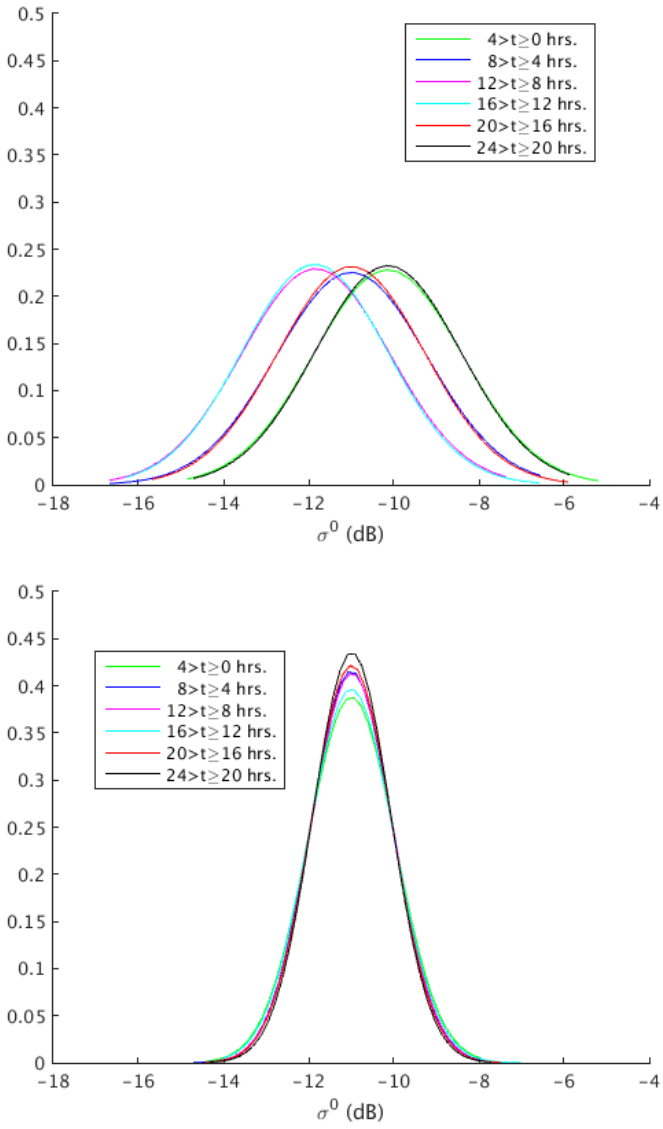

Figure 4.14: Distributions of the LTOD bins for the normalization of σ^0 versus LTOD in Fig. 4.12. Top: the original distributions for σ^0 versus LTOD. Bottom: the same distributions after normalizing σ^0 dependence on both LTOD and incidence angle. Note that the means are aligned in the bottom figure and that the variance is visibly reduced. The means are aligned by normalizing σ^0 to a single LTOD bin, and the variance is reduced by normalizing σ^0 with respect to incidence angle.

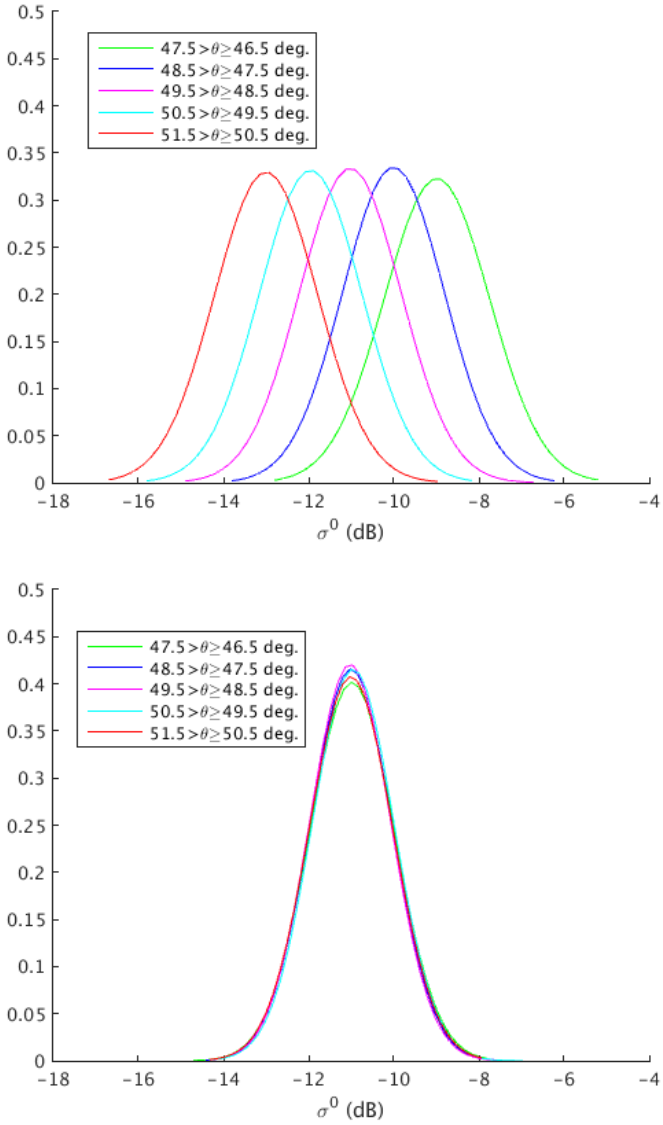

Figure 4.15: Distributions of the incidence angle bins for the normalization of σ^0 versus incidence angle in Fig. 4.13. Top: the original distributions for σ^0 versus incidence angle. Bottom: the same distributions after normalizing σ^0 dependence on both incidence angle and LTOD. Note that the means are aligned in the bottom figure and that the variance is visibly reduced. The means are aligned by normalizing σ^0 to a single incidence angle bin, and the variance is reduced by normalizing σ^0 with respect to LTOD.

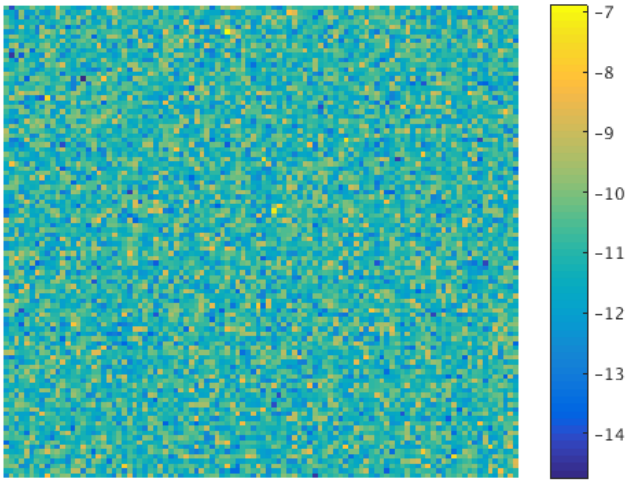

Figure 4.16: Reconstructed image of the normalized measurements. Note that the incidence angle and LTOD variations have been removed (compare with Fig. 4.11).

Table 4.2: Mean and variance of σ^0 measurements in each of the images produced for the first simulation scenario (see Figs. 4.10, 4.11, and 4.16). Note that the RapidScat incidence angle and LTOD variations cause significantly higher variability in the unadjusted (not normalized) image, compared to the synthetic truth image. The normalized image has significantly reduced variability of σ^0 measurements, and the variance of this image is close to the original variance exhibited in the synthetic truth image. The mean is shifted significantly by the synthetic RapidScat measurement system, and the mean is unaffected by the normalization procedure. The mean is unaffected by the procedure because the nominal value used for adjusting σ^0 is the same as the mean σ^0 value.

Data	Mean	Variance
Synthetic Truth (Fig. 4.10)	- 8.000 dB	0.992
Not Normalized (Fig. 4.11)	-10.978 dB	3.539
Normalized (Fig. 4.16)	-10.978 dB	0.999

these effects are removed. The same pattern might infer an increase in these variations, but this leads to an increase in variance.

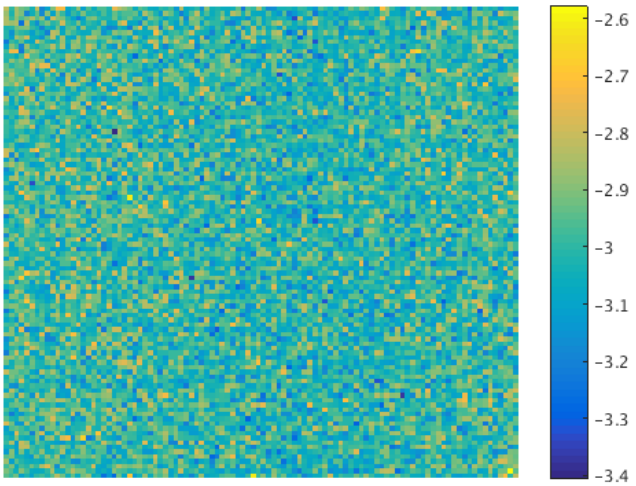

Figure 4.17: Difference between the normalized image (Fig. 4.16) and the synthetic truth image (Fig. 4.10). Note that there is a difference close to 3 dB between the means of the two images (see color scale). Also note that there is a significant variance in the difference (see color scale range). The mean difference is caused by simulated incidence angle and LTOD variability (see Table 4.2), and the variance is mainly due to radar receiver noise ($\sigma^2 = (0.1)^2$).

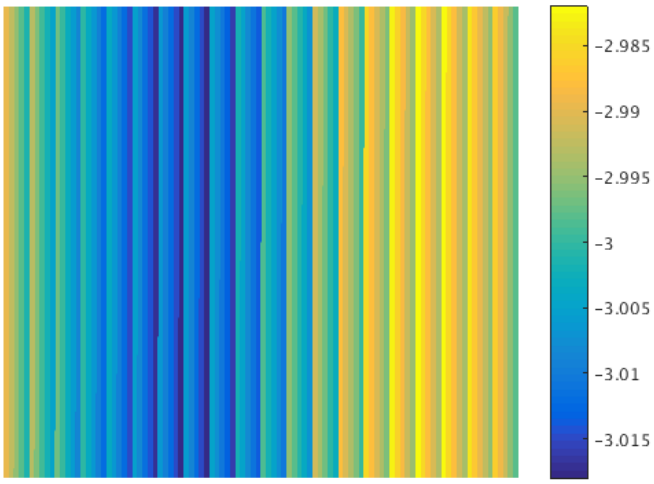

Figure 4.18: Difference between the normalized image (Fig. 4.16) without receiver noise and the ideal reconstructed image (Fig. 4.10). Note the difference in the mean close to 3 dB (caused by measurement variation and the calibration procedure), as well as a variance in the difference, which is due to residual LTOD and incidence angle variations (see color scale). These errors are significantly less than the errors present in Fig. 4.17. The small variance in this image shows the effectiveness of the normalization procedure.

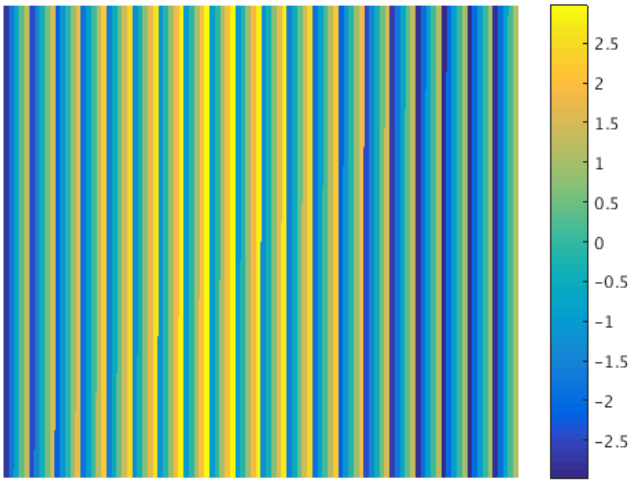

Figure 4.19: Difference between the normalized image (Fig. 4.16) and the original measured image (Fig. 4.11). This is the only difference image that is possible to calculate for real data, since there is no real truth data. The pixel values are significantly different from the true difference image, but the pattern is similar (see Fig. 4.18). This pattern and the reduced variance in Table 4.2 suggest that variations in the pixels are removed by the normalization procedure.

4.2.2 Augmented Simulation Scenario

For the second scenario, a more detailed measurement process is followed. Measurement swaths are modeled as being 20 antenna response patterns wide, and the swaths are oriented as diagonals across the measurement region. This mimics the orbital passes of the ISS more closely than the first scenario. The measurement swaths are non-overlapping for one set of passes, but a second set of passes is made with the same diagonal orientation, with swaths slightly overlapping the swaths from the previous set. Two additional sets of passes are created in the same way, with diagonals passing in the other direction across the opposite corners. Fig. 4.20 shows an example of one set of diagonal passes, including incidence angle and LTOD variations.

Additionally, the correlations between LTOD, roll angle, and incidence angle are included. The model for roll versus LTOD is a cosine, with a random phase shift and amplitude, with a different realization for each pass. The roll angle model

$$\varphi(t) = -(1-\nu_1)(0.287)\sin\left(\frac{2\pi}{24}(t-1.36-\nu_2)\right)+0.994, \tag{4.5}$$

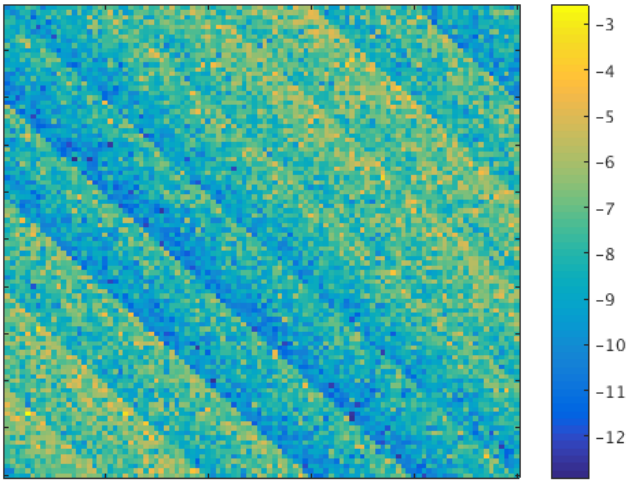

Figure 4.20: One set of simulated measurement passes for the second simulation scenario, including LTOD and incidence angle variations.

where φ is the roll angle in degrees, and t is the LTOD in hours (see the top plot in Fig. 4.21). The random variables have zero-mean Gaussian distributions with different variances, where $v_1 \sim N\left[0, \left(\frac{1}{4}\right)^2\right]$ and $v_2 \sim N\left[0, \left(\frac{2\pi}{4}\right)^2\right]$. The roll angle is simulated to be constant for each pass of the radar, since the LTOD of each pass is also constant. This model is determined by a least-squares estimate of roll and LTOD measures from the wet season in the Amazon (see the top plot in Figs. 4.22). The roll value for each pass is calculated from the LTOD values of each pass in the simulation. The LTOD for each swath varies in the simulation so that a full 24 hours are covered across the measurement region, and these LTOD values are exactly 12 hours later for the passes crossing the other diagonal direction.

Roll angle values determine the range of incidence angle variation. The model for the range of variation

$$R_\theta(\varphi) = 2.1032\ln(\varphi) + 2.5215, \tag{4.6}$$

where R_θ is the range of incidence angle values (in degrees) spanned for the pass, and φ is the roll angle (in degrees) (see the bottom plot in Fig. 4.21). The coefficients of this model are determined by a least-squares estimate of roll versus the range of incidence angle for data from four arbitrary consecutive orbital revolutions (see the bottom plot in Fig. 4.22). This model is only accurate

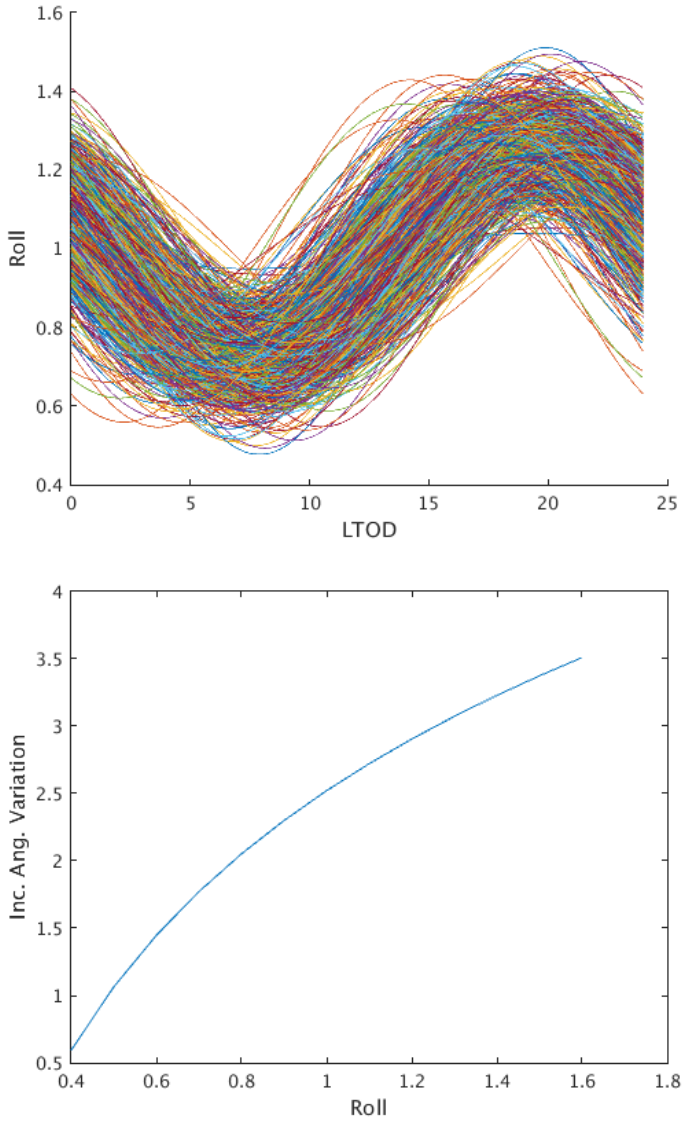

Figure 4.21: Models for orbital attitude effects in the measurements for the second simulation scenario. Top: One thousand realizations of the model of the dependence of roll angle on LTOD. Each unique realization of the model is used for a single pass to determine a specific roll angle from the LTOD of the pass (the roll angle is assumed to be constant across a single pass). Bottom: Model for the dependence of incidence angle variation on the roll angle. The roll angle determined from the top model determines the range of incidence angles across the swath.

within the measured range of $[0.6, 1.6]$ degrees roll angle. Incidence angle values are calculated so that the maximum and minimum values occur in the leftmost and rightmost edges of the swath, respectively, and then the values decrease linearly from the left side of the swath to the other.

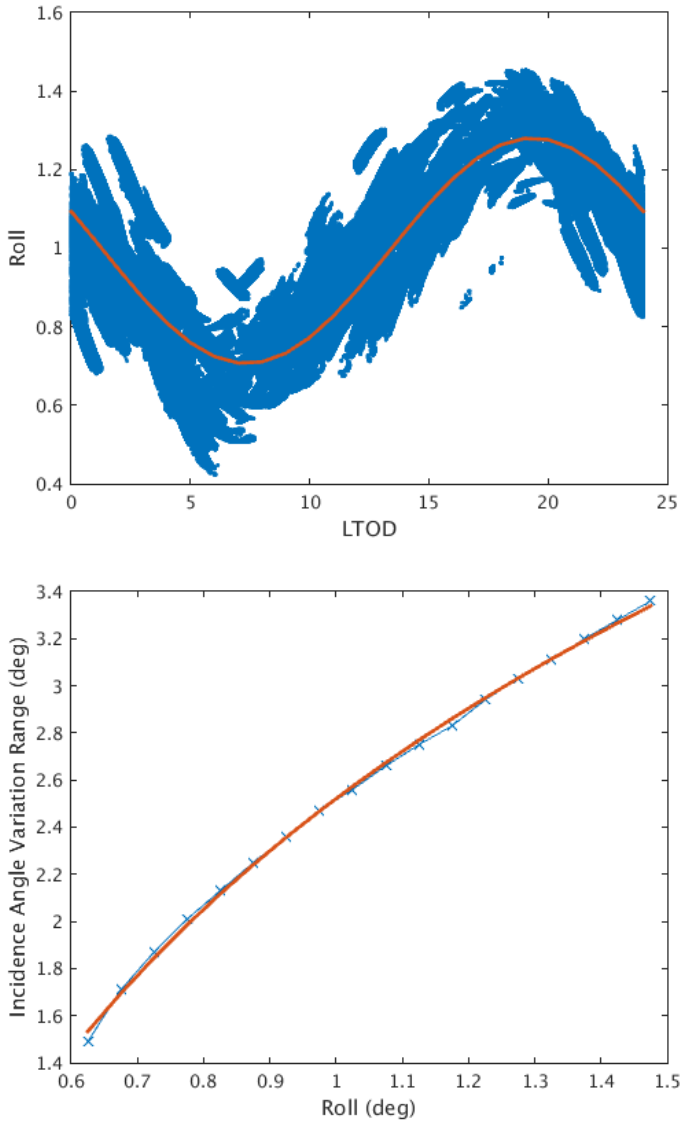

Figure 4.22: Data used to estimate the least squares models of attitude effects on σ^0 (see Fig. 4.21). Top: Actual RapidScat data used to model roll angle dependence on LTOD. From days 1–151, 2016. The fit line in the data points shows the mean function for the random model in Fig. 4.21. The line segments in the data are incomplete due to masking the data. Note that the individual line segments seem to have different phases and amplitudes than the central line. Bottom: RapidScat data used to model incidence angle variation range dependence on roll angle. From four arbitrary consecutive revs, day 100, 2015. This model is only considered accurate within this range of roll angles ($[0.6, 1.6]$ degrees).

The whole measurement process in this scenario is

$$\sigma^0_{meas}(x,y,\theta,t) = \sigma^0_{true}(x,y) + (\theta_{nom} - \theta) + \cos\left(\frac{2\pi}{24}t - \frac{\pi}{2}\right) + n(x,y) \;\; dB, \tag{4.7}$$

where $\theta_{nom} = 49^\circ$, θ is the incidence angle calculated from the roll angle (which is calculated from the LTOD), t is the LTOD, and (x,y) designates a pixel location in the region, and $n(x,y) \sim N[\mathbf{0}, \sigma^2\mathrm{I}]$ represents receiver noise for each antenna measurement, where $\sigma^2 = (0.1)^2$ (see Fig. 4.23). The incidence angle value is calculated as

$$\theta(t,k) = \left(\theta_{nom} + \frac{R_\theta(\varphi(t))}{2}\right) - \frac{R_\theta(\varphi(t))}{20}k, \tag{4.8}$$

where t is the LTOD of the pass; $\varphi(t)$ is the roll angle of the pass, calculated from the current LTOD; $R_\theta(\varphi(t))$ is the range of incidence angle values spanning the swath, calculated from the current roll angle; and k is the index of the column of the swath ($k = 1,2,\ldots,20$, counting from left to right for the first two set of diagonal passes and right to left for the second two sets of passes). Fig. 4.24 shows the truth image, and Fig. 4.25 shows the results of Eq. 4.7 on the truth data.

The normalization procedure is performed as before, except that σ^0 dependence on incidence angle is normalized first, followed by the dependence on LTOD (see Figs. 4.26, 4.27, 4.28, and 4.29). The adjusted image has minimal effects from LTOD and incidence angle remaining, and most of the residual error is from measurement receiver noise (see Figs. 4.30, 4.31, 4.32). Error is defined as the difference between the adjusted image and the truth image, as before (see Figs. 4.31 and 4.32). However, the difference that can be calculated for real data is the difference between the adjusted image and the original measured image (see Fig. 4.33). Seeing a pattern of incidence angle and LTOD effects on σ^0 (as seen in Fig. 4.33) and a decrease in overall variance in this difference image suggests that the normalization was successful at removing σ^0 variation caused by these parameters. Table 4.3 shows the mean and variance for each image of the normalization procedure for the second simulation scenario.

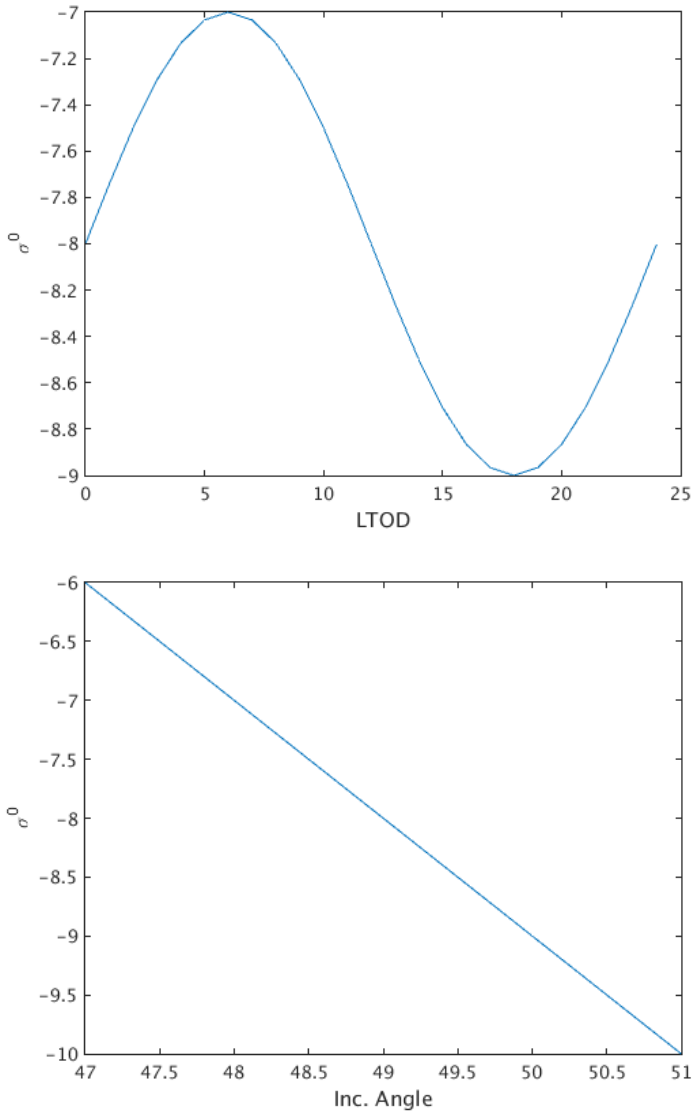

Figure 4.23: Models for incidence angle and LTOD variations in σ^0 in the second measurement scenario. Top: Model for σ^0 dependence on LTOD. This model determines how much to alter σ^0 from the mean for a given LTOD. Bottom: Model for σ^0 dependence on incidence angle. This model determines how much σ^0 is altered from the original value, based on a given incidence angle. LTOD values are chosen arbitrarily for each pass, which then determines the roll angle, and then the roll angle determines what incidence angle values to use for the measurement pass (using models in Fig. 4.21).

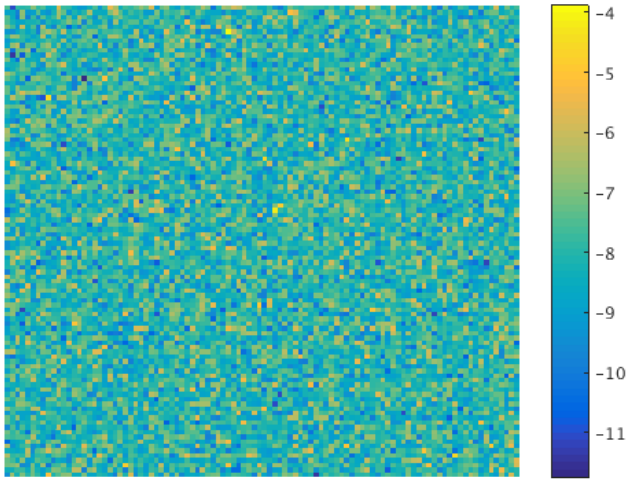

Figure 4.24: Ideal reconstructed image of the synthetic truth values of σ^0 for the second scenario. This image synthesizes a homogeneous land region, like the Amazon rainforest. Each pixel simulates an ideal antenna response pattern for that location. This image is equivalent to the image in Fig. 4.10, even though there are four overlapping measurements that are averaged together in each pixel location.

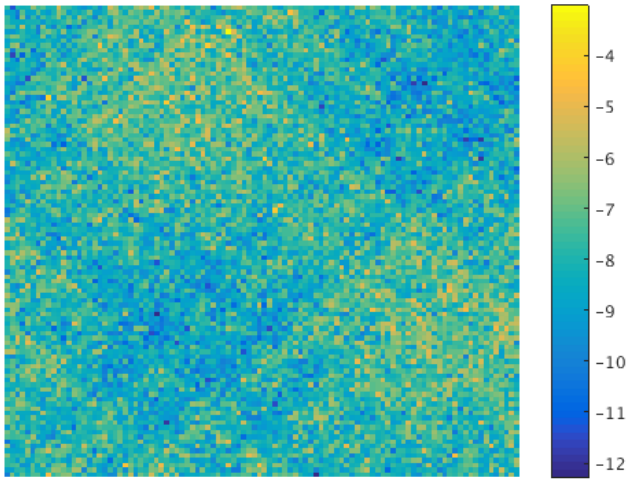

Figure 4.25: Simulated reconstructed RapidScat image of the Amazon rainforest, including errors from incidence angle and LTOD variation. A simple "drop-in-the-bucket" (DIB) algorithm is used, where measurements in the same pixel are averaged together.

Table 4.3: Mean and variance of σ^0 measurements in each of the images produced for the second simulation scenario (see Figs. 4.24, 4.25, and 4.30). Note that the RapidScat measurement variations cause a much higher variance in the data compared to the synthetic truth data. The normalization procedure reduces the overall variance of σ^0 measurements to be close to the original variance exhibited in the synthetic truth data image. Note that the mean is changed by the measurement process, as well as the normalization procedure. It is not feasible to estimate the original mean, but the normalization procedure can be designed to keep the mean the same as before the normalization procedure, if desired.

Data	Mean	Variance
Synthetic Truth (Fig. 4.24)	-8.000 dB	0.992
Not Normalized (Fig. 4.25)	-7.952 dB	1.322
Normalized (Fig. 4.30)	-7.877 dB	0.997

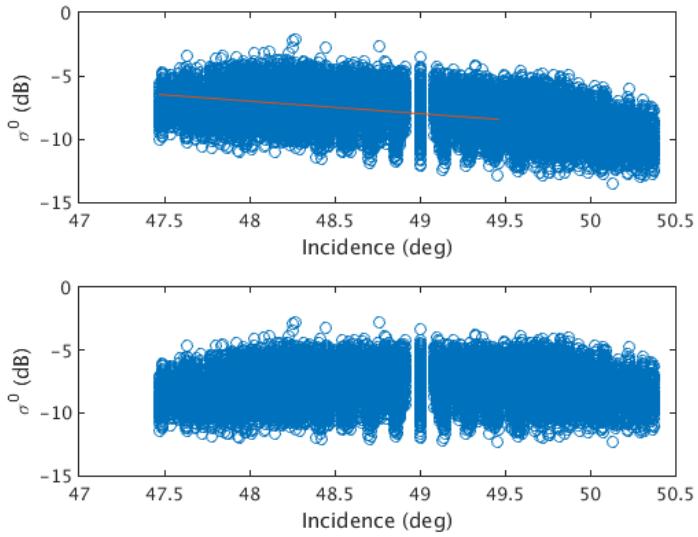

Figure 4.26: Normalization procedure for σ^0 dependence on incidence angle for the second simulation scenario. A least squares method is used to model σ^0 dependence on incidence angle (top). Then all values at every incidence angle bin are adjusted to have the same mean as the nominal incidence angle bin (bottom).

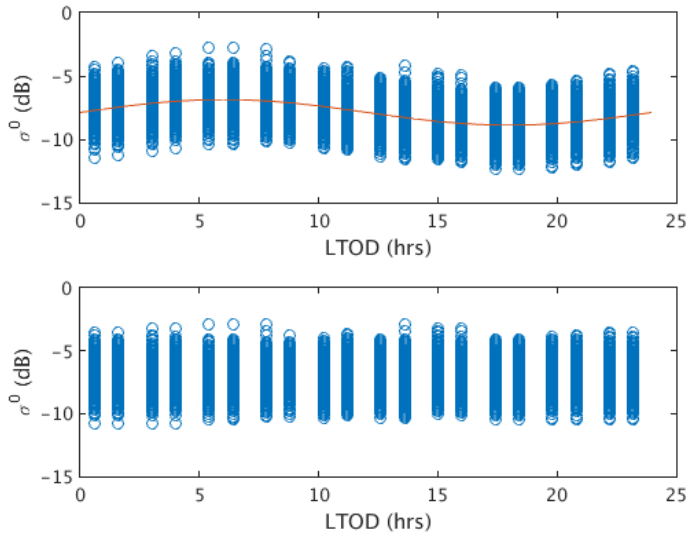

Figure 4.27: Normalization procedure for σ^0 dependence on LTOD for the second simulation scenario, after σ^0 dependence on incidence angle is normalized. A least squares method is used to model σ^0 dependence on LTOD (top). Then all values at every LTOD bin are adjusted to have the same mean as the nominal LTOD bin (bottom).

4.2.3 Additional LTOD Considerations

An additional scenario to consider for simulation is using a shorter day range for the data. When RapidScat data is normalized for a day range less than 60 days long, there is no assurance that a full 24 hours of LTOD are available for modeling. When day ranges are only a few days long, two disjoint ranges of LTOD values are measured if both ascending and descending passes are included, and one single, narrow range is measured if only ascending or descending passes are included.

Though it is possible to include a large enough day range of RapidScat data for any normalization procedure, it is faster computationally to only normalize data from a few days. Fig. 4.34 shows an example of a simulated normalization procedure for two disjoint ranges of LTOD, representing what this data might look like for two to six consecutive days of RapidScat data. When the LTOD ranges are narrow (like Fig. 4.34), the periodic nature of σ^0 dependence on LTOD is not evident, so a linear fit for each disjoint range can be more accurate for normalization. It is recommended to consider this linear approach for LTOD ranges that are 4 hours long or less, for each data range. For a range longer than 4 hours, the sinusoidal nature of LTOD dependence can lead

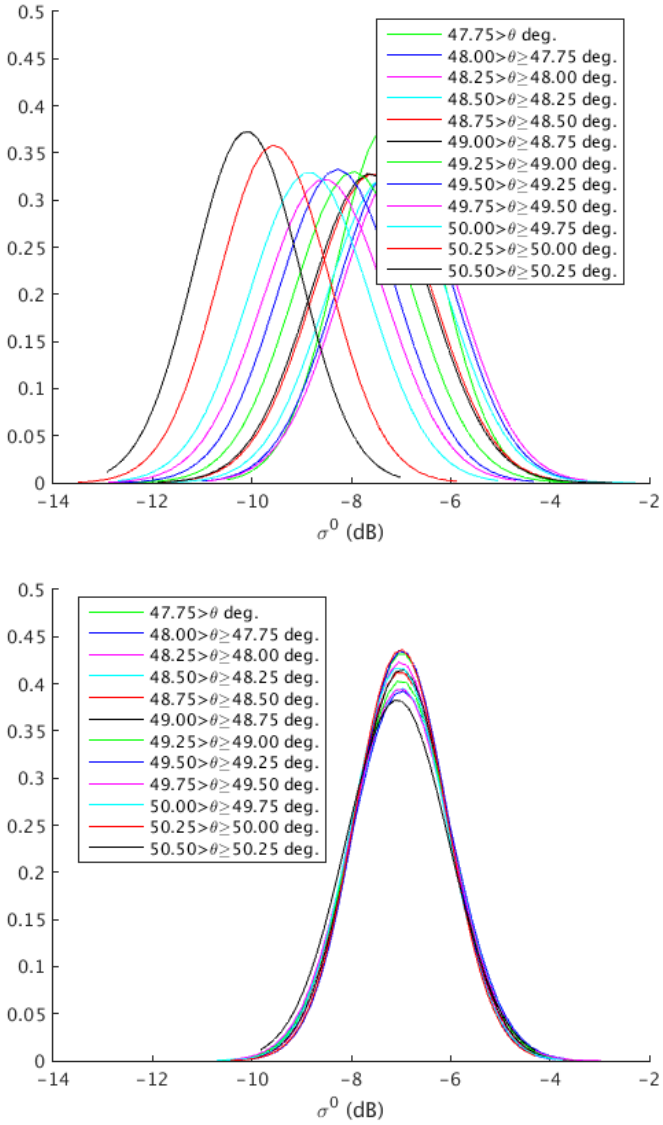

Figure 4.28: Distributions of the incidence angle bins for the normalization of σ^0 versus incidence angle (see Fig. 4.26). Top: the original distributions for σ^0 versus incidence angle. Bottom: the same distributions after normalizing both σ^0 versus incidence angle and σ^0 versus LTOD. Note that the means are aligned in the bottom figure and that the variance is visibly reduced. The means are aligned by normalizing σ^0 to a single incidence angle bin, and the variance is reduced by normalizing σ^0 with respect to LTOD.

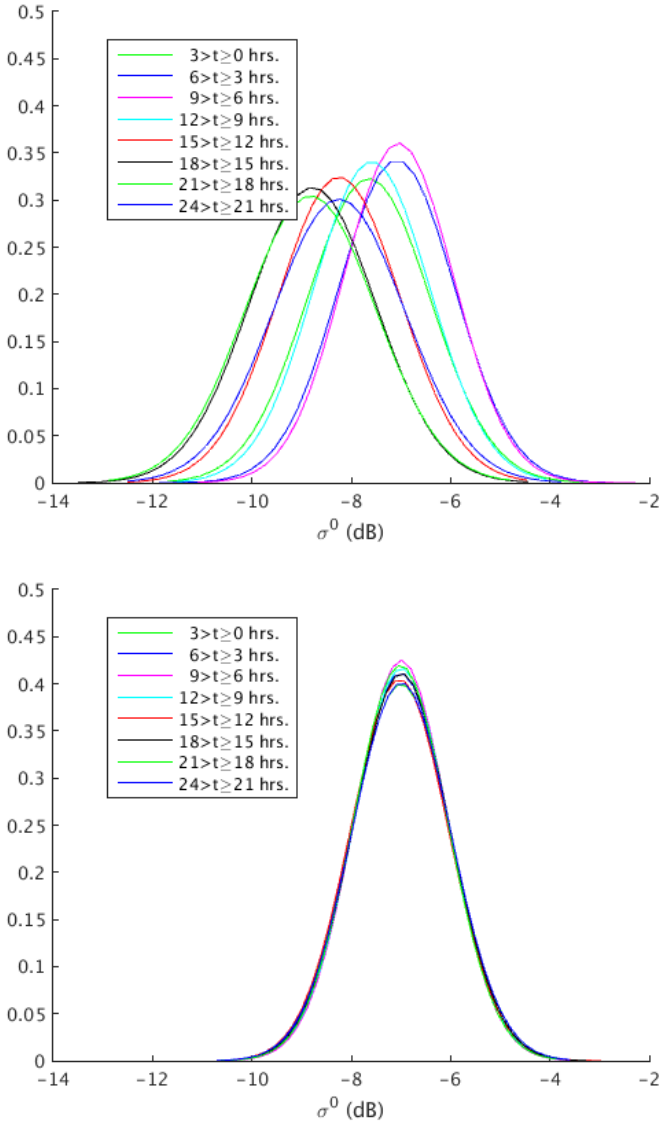

Figure 4.29: Distributions of the LTOD bins for the normalization of σ^0 versus LTOD (see Fig. 4.27). Top: the original distributions for σ^0 versus LTOD. Bottom: the same distributions after normalizing both σ^0 versus LTOD and σ^0 versus incidence angle. Note that the means are aligned in the bottom figure and that the variance is visibly reduced. The means are aligned by normalizing σ^0 to a single LTOD bin, and the variance is reduced by normalizing σ^0 with respect to incidence angle.

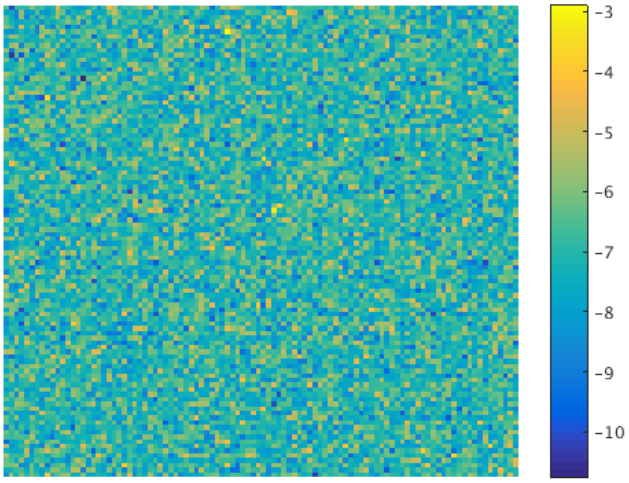

Figure 4.30: Reconstructed image of the normalized measurements for the second simulation scenario. Note that the incidence angle and LTOD variations have been removed.

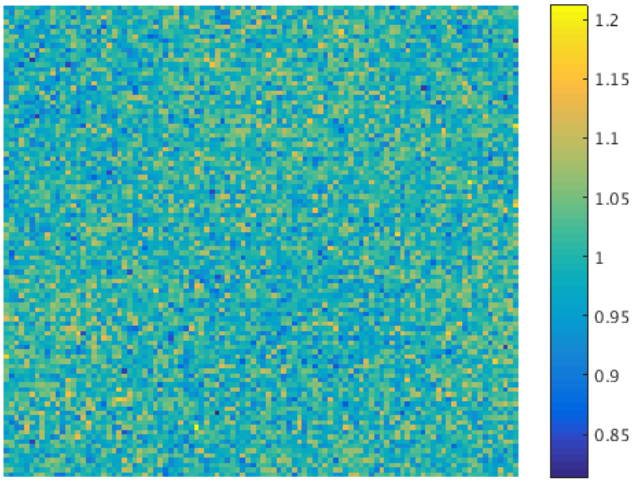

Figure 4.31: Difference between the normalized image (Fig. 4.30) and the ideal image reconstruction (Fig. 4.24). Note the difference in the mean close to 1 dB (caused by measurement variation and the calibration procedure), as well as a variance in the difference, which is mainly due to radar receiver noise ($\sigma^2 = (0.1)^2$).

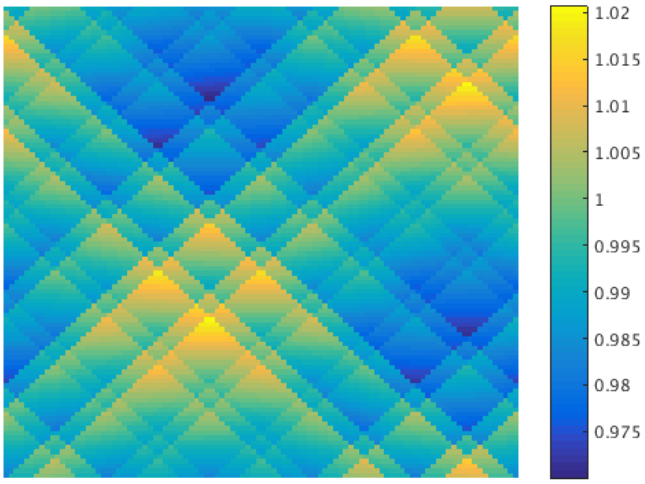

Figure 4.32: Difference between the normalized image without receiver noise and the ideal reconstructed image, shown to illustrate the effects of receiver noise. The mean difference ($\sim$1 dB) is caused by incidence angle and LTOD variations, as well as imperfections in the normalization procedure. The variance in the error is mostly caused by imperfections in the normalization procedure, but these errors are significantly less than the range of the radar receiver noise present in Fig. 4.31.

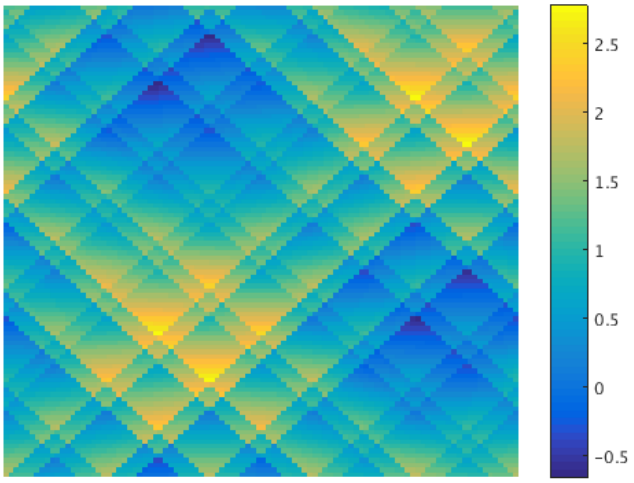

Figure 4.33: Difference between the normalized image (Fig. 4.30) and the unadjusted image (Fig. 4.25), shown to understand the magnitude of the correction. The pixel values are significantly different from the true difference image, but the pattern is similar (see Fig. 4.32). A pattern like this in the difference image and a reduction in pixel variance in the normalized image suggest that incidence angle and LTOD variations have been minimized.

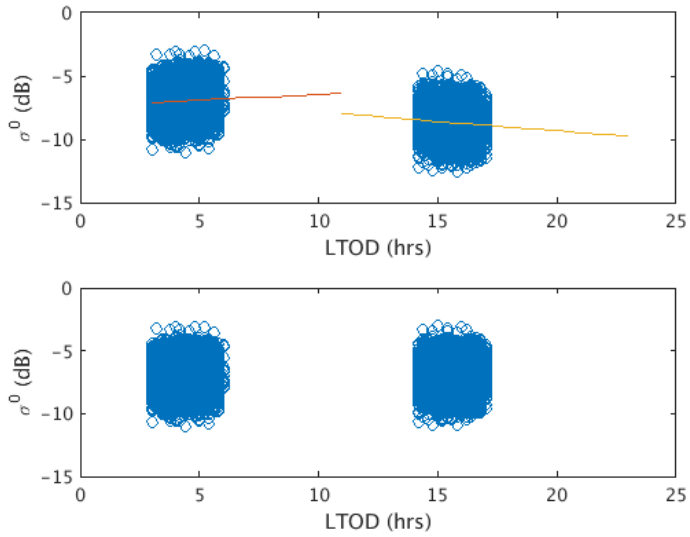

Figure 4.34: Plot of piecewise normalization procedure for LTOD. This is a representation of a normalization of σ^0 dependence for short day ranges.

to inaccurate linear fits. Fig. 4.35 shows that a piecewise linear fit and normalization still yields effective results. The LTOD distribution in Fig. 4.35 that appears to be off-center may be less accurate because the LTOD bin associated with it contains a very small amount of measurement values and so estimates of mean and variance are less accurate.

4.3 Summary

In summary, a normalization procedure is demonstrated in this chapter that is effective at estimating and removing σ^0 dependence on incidence angle and LTOD. It is shown that removing dependence on incidence angle and LTOD also reduces dependence on other significant parameters. In simulation, it is shown that SIR image quality can be affected by RapidScat attitude and orbit variations and that a normalization procedure can reduce variance in these images. In the next chapter, a normalization procedure is applied to real RapidScat data, and the effect on RapidScat SIR images is analyzed.

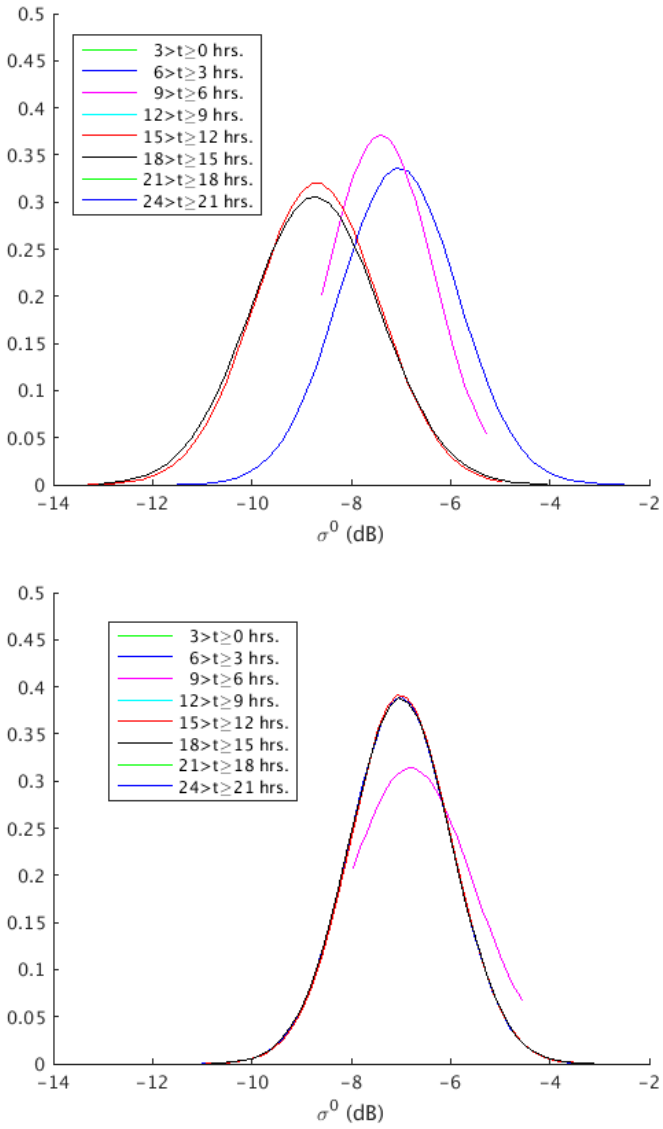

Figure 4.35: Distribution of LTOD bins for a short day range (2–6 days), when data is only available for a few hours of LTOD (see Fig. 4.34). Note that a piecewise first-order polynomial model is quite effective at normalizing σ^0 as seen before (see Figs. 4.14 and 4.29). The incomplete distribution curve represents an LTOD bin with a smaller amount of points and so it is less accurate.

CHAPTER 5. RESULTS

The normalization procedure discussed in the previous two chapters is applied in this chapter to actual RapidScat L1B data to make normalized SIR images. Initially, several SIR setup files are created for a region. SIR setup files contain L1B measurements that are organized into their respective pixel locations within the image. These setup files are used to create large measurement vectors of σ^0 and other significant parameters. These vectors are used to estimate a least-squares model of σ^0 dependence on LTOD, and then this dependence is normalized. Next, a model of σ^0 dependence on incidence angle is estimated from the adjusted σ^0 values, and the dependence on incidence angle is normalized. Finally, the corrected measurements are written to new SIR setup files and used by the SIR algorithm to make radar images. This procedure is used for two separate regions to show the effect of the procedure with actual RapidScat data.

5.1 Amazon Region

First, a normalized SIR image is created over the Amazon to compare with analysis and simulation performed in previous chapters. The original Amazon image can be seen in Fig. 5.1, and the adjusted image can be seen in Fig. 5.2. Fig. 5.3 shows the difference between the normalized image (Fig. 5.2) and the original image (Fig. 5.1). This difference image is used as a reference because there is no visually significant difference between the original and adjusted images. The difference image shows a pattern of incidence angle and LTOD values, as in simulation (see Fig. 4.33). Table 5.1 shows the variance of the pixels in the original and adjusted SIR images over the Amazon (note the reduced variance in the adjusted image). Since these images contain a substantial number of pixels below -30 dB (in the border), a mask is used for the variance calculation (see Fig. 5.4). The normalization procedure reduces the variance beyond the 95% confidence interval of the original estimate for pixels within the border. The fact that the total variance of the

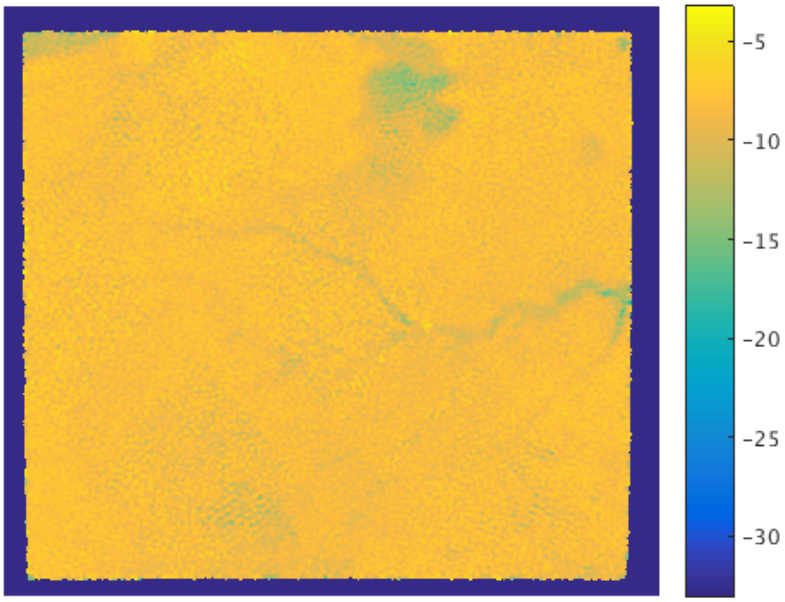

Figure 5.1: Original RapidScat SIR image of a region of the Amazon rainforest for days 101-105, 2016.

Table 5.1: The variance of the Amazon SIR images in Figs. 5.1 and 5.2. Because of a significant number of σ^0 values that are less than -30 dB in the borders, a mask is used for calculating variance (Fig. 5.4). A decrease in variance after the adjustment is evidence of a reduction in pixel variation caused by incidence angle and LTOD. Note that the variance decrease is beyond the 95% confidence interval.

Step	Variance	95% Confidence
Original Image (Fig. 5.1)	0.993	0.989–0.996
After Normalization (Fig. 5.2)	0.978	0.974–0.982

image decreases in a statistically significant way demonstrates that the normalization effectively reduces variability in σ^0 caused by incidence angle and LTOD.

5.2 Arbitrary Region

For further analysis, a SIR image is created over an arbitrary region. The unadjusted SIR image of this region can be seen in Fig. 5.5. This arbitrary region is chosen to show the application of the normalization procedure to a different region with less homogeneous land features. All

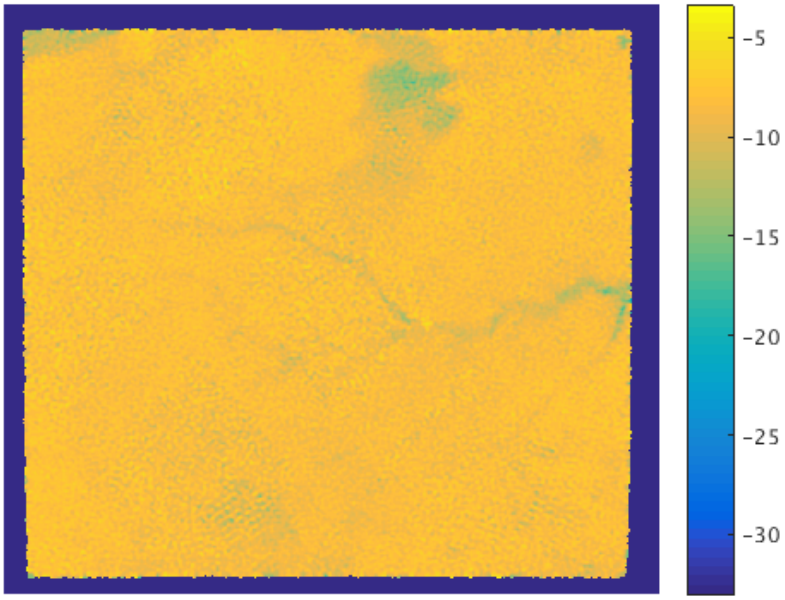

Figure 5.2: Adjusted SIR image of a region of the Amazon rainforest for days 101-105, 2016. Note that there is no significant visual difference between this image and the original (Fig. 5.1). Fig. 5.3 better exhibits the differences that are present between the two.

analysis in previous chapters is done over the Amazon mask in order to ensure homogeneity. In this case, the arbitrary region is small enough to be able to assume some level of homogeneity, though a large amount of variability is still present. The region chosen for this test is in Eastern Africa, which includes parts of Uganda, Kenya, Tanzania, and all of Lake Victoria.

Having a large body of water within the region requires special consideration. Water measurements have a significantly different distribution than land measurements, and the σ^0 dependence on parameters is considerably different over water than land. Combined, the water and land σ^0 measurements create a distribution with multiple modes (see Fig. 5.6), so a data mask is determined for σ^0 adjustments that excludes water measurements (see Fig. 5.7). The mask is designed so that only data centered around the most significant land mode are used.

The mask associated with the most significant mode is determined by an iterative search. The search is initialized with the median of the σ^0 measurements. The new mean value is computed within one standard deviation of the starting value, and then the starting value is replaced by the

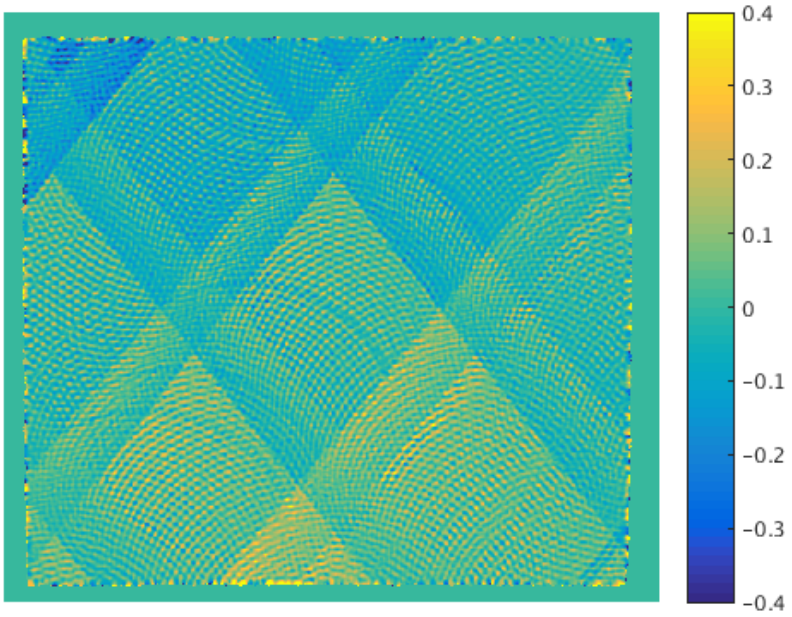

Figure 5.3: Difference between the adjusted (Fig. 5.1) and original (Fig. 5.2) SIR images of a region of the Amazon rainforest. Note that a pattern is shown in this image that is similar to difference images created in simulation (see Fig. 4.33). The spiral cross-hatch pattern is caused by incidence angle variations, and the light and dark regions suggest LTOD variations.

new mean value. This process iterates 100 times. The final value is centered on the largest mode in the distribution of σ^0 measurements.

The mask only includes measurements within the range of one standard deviation of the final value of the iterative search (see Fig. 5.8). The masked data is centered around the σ^0 mode associated with land rather than water. This happens because there are significantly more land measurements than water, and water measurements tend to have much lower σ^0 values than land measurements. Measurements that fall within the mask are used to make a model for LTOD dependence, and then all σ^0 values (including data outside the mask) are adjusted to normalize LTOD dependence. Next, the adjusted σ^0 values that fall within the mask are used to make a model for dependence on incidence angle, and that model is used to normalize dependence on incidence angle for all σ^0 values.

There is no truth data to verify SIR images, but QuikSCAT data has low variance compared to other scatterometers ($\sigma^2 \approx 0.4$ in the Amazon region shown above) and a long mission life, so it

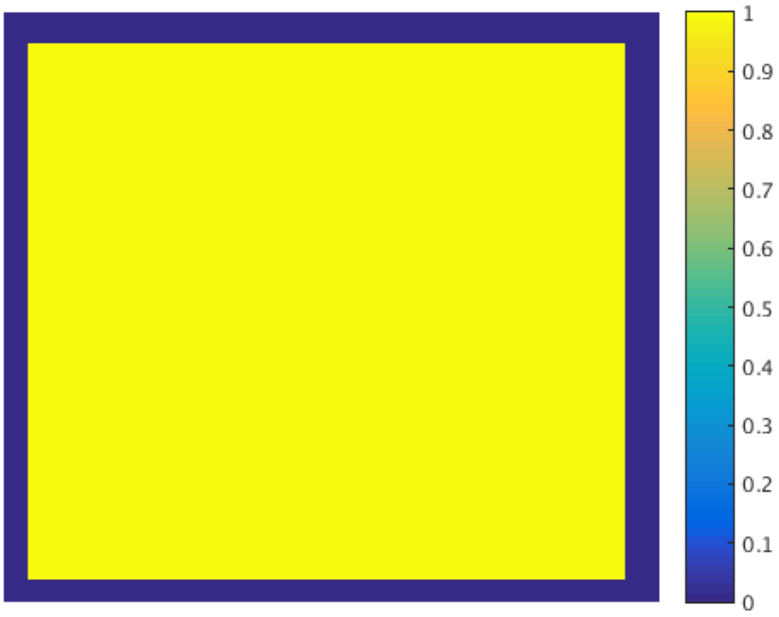

Figure 5.4: The mask used for the variance calculation for the Amazon SIR images. Only light-colored pixel locations from the Amazon images are used to calculate variance estimates. The mask removes the border pixels, which contain very small values. The small border values are an artifact of the SIR algorithm and are not significant to the image of the region.

is a baseline to compare to. Fig. 5.9 shows a QuikSCAT SIR image of the same region as Fig. 5.5. This represents what a "good" SIR image of the region is expected to look like. Note that the noise is much more significant in the RapidScat image. QuikSCAT images look very "smooth," which is a sign of low noise.

The adjusted image (Fig. 5.10) is compared with the QuikSCAT image (Fig. 5.9) by computing a difference image in Fig. 5.11. Incidence angle and LTOD effects are not clearly evident in this difference image. This image shows that there is much more noise present in RapidScat data than just variation caused by incidence angle and LTOD. Since observing this difference image provides limited insight, the differences between the normalized image and the original image are analyzed instead.

The differences between the adjusted RapidScat image (Fig. 5.10) and the original one (Fig. 5.5) are not visually evident, so a difference image is computed. This image is shown in Fig. 5.12. The difference image shows a pattern of measurement swaths. Additionally, the vari-

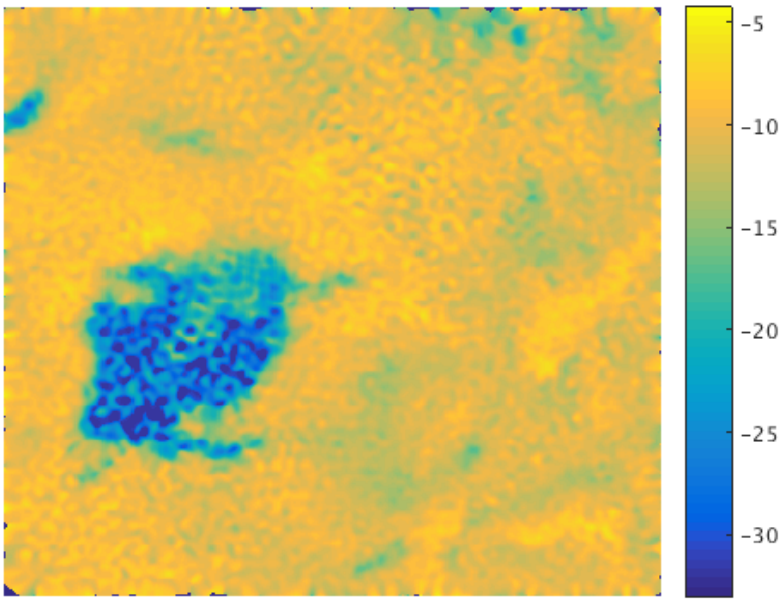

Figure 5.5: RapidScat SIR image of an arbitrary small region of East Africa, including parts of Uganda, Kenya, Tanzania, and all of Lake Victoria. Region covers the area between 4° S to 3° N and 31° E to 38° E. Days 100-105, 2016.

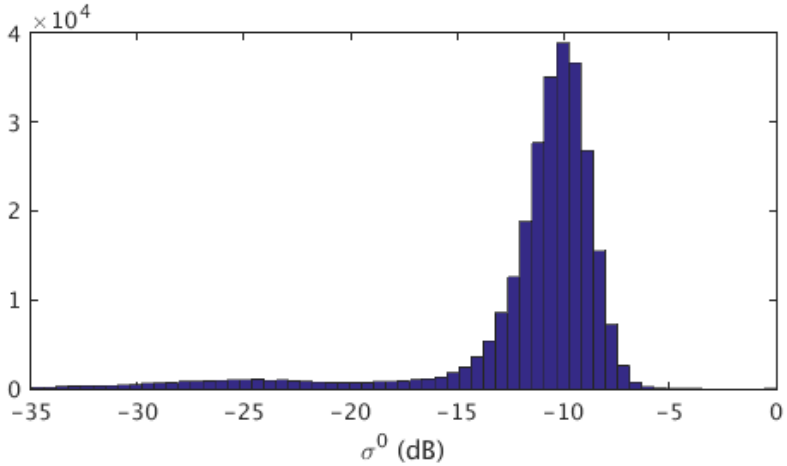

Figure 5.6: Histogram of σ^0 values contained in the East Africa region shown in Fig. 5.5 for days 61-120, 2016. Note most values are centered around the mode close to -10 dB. The values that are lower down are mostly associated with water locations.

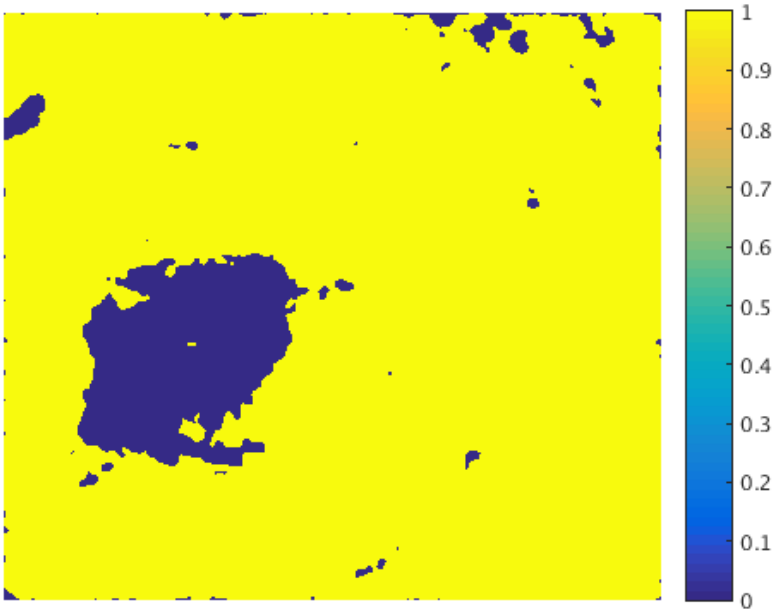

Figure 5.7: Mask of pixel locations in the East Africa SIR image used to calculate normalization. Only light-colored pixels within this region are used to calculate the models for normalization so that it is unaffected by Lake Victoria and other bodies of water.

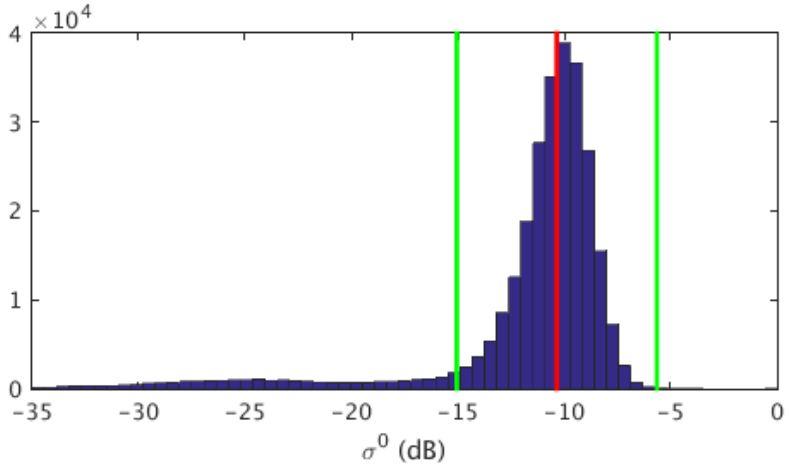

Figure 5.8: Histogram of σ^0 values contained in the East African region shown in Fig. 5.5, including the mean and standard deviation lines used to determine the mask for this region, as seen in Fig. 5.7. Only values between the outer lines are used for model estimation for the normalization procedure. These values are associated with the light-colored regions in Fig. 5.7.

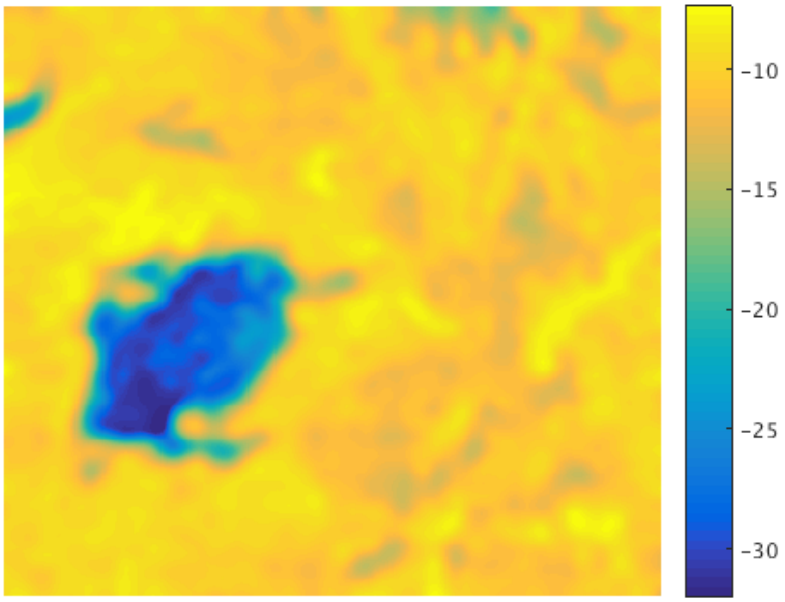

Figure 5.9: QuikSCAT SIR image of the same East African region as in Fig. 5.5. QuikSCAT images appear blurry compared to RapidScat images, which is a mark of low noise (see Fig. 5.5).

ance of the image pixels is reduced after the normalization procedure. Note the bright spot in the difference image over Lake Victoria. Because water and land measurements have significant differences in σ^0 dependence models, a significant error is caused in the water locations by the normalization procedure. The variances of the original and adjusted SIR images are calculated within masked locations of the region that do not include regions with large bodies of water (see Fig. 5.13 for the mask). Table 5.2 shows the variances of the two images. In the case of this 6-day image (Fig. 5.10), the variance is decreased by the normalization procedure to be beyond the 80% confidence interval of the original estimate. The decrease in variance suggests that the normalization procedure is effective at reducing variability in the images caused by σ^0 dependence on incidence angle and LTOD, although the decrease in variance is within the 95% confidence interval of the original estimate.

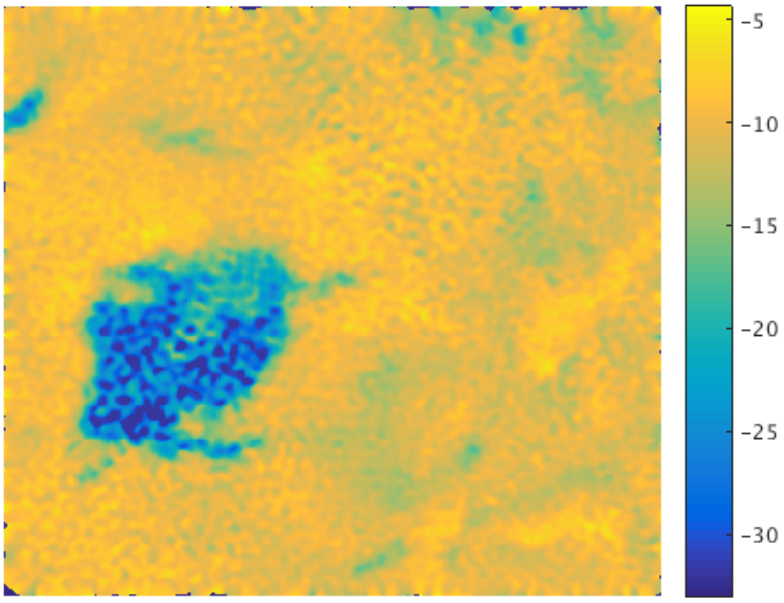

Figure 5.10: RapidScat SIR image of adjusted σ^0 measurements in the same region as Fig. 5.5. There is no marked visual difference between this image and the previous one in Fig. 5.5. A difference image is necessary to see significant differences (see Fig. 5.12).

Table 5.2: The variance of the 6-day East Africa SIR images in Figs. 5.5 and 5.10. Because of low values present in water pixels, a mask is used to remove these pixels for the variance calculation (see Fig. 5.13). Note that the variance decreases beyond the 80% confidence interval after the normalization procedure.

Step	Variance	80% Confidence
Original Image (Fig. 5.5)	3.528	3.509–3.547
After Normalization (Fig. 5.10)	3.504	3.485–3.523

5.2.1 Longer Day Ranges

To expand the analysis, SIR images from longer day ranges are averaged together to see if a larger effect on variance is seen when receiver noise is reduced and LTOD effects are more evident. SIR images are computed for 30 days and 60 days of data. These images are computed by averaging together 6 or 12 five-day images of RapidScat data, respectively. Averaging images helps to reduce measurement noise, which can potentially enable better visibility of the changes due to normalization. These images are shown in Figs. 5.14 and 5.15, respectively.

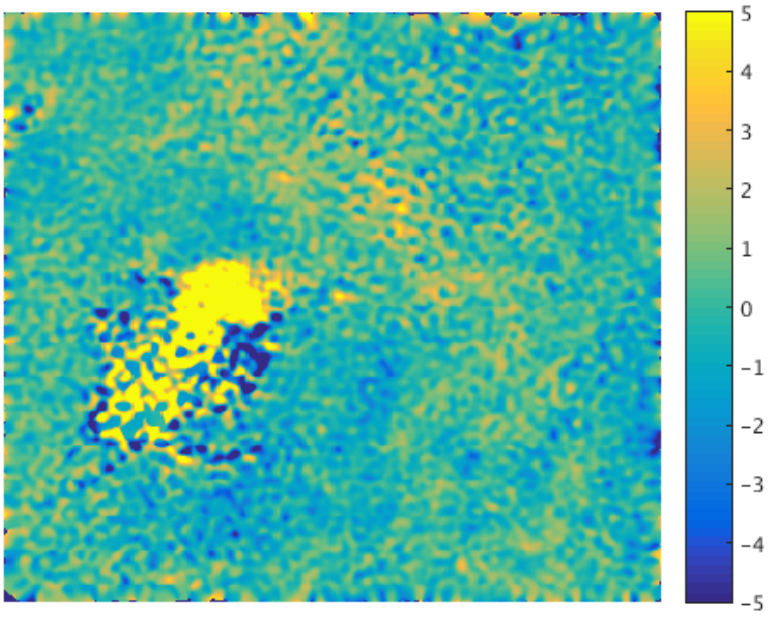

Figure 5.11: Difference of the adjusted SIR image (Fig. 5.10) and the QuikSCAT image (Fig. 5.9). Note that there are still significant differences between RapidScat and QuikSCAT that cannot solely be attributed to incidence angle variation, which makes this difference image impractical for measuring the effect of σ^0 normalization procedures. Also note that the values over Lake Victoria have the largest difference, compared to QuikSCAT. The difference over Lake Victoria is exaggerated because σ^0 measurements of water are normalized with the same dependence models as the land measurements, and the dependence models for land are significantly different than the models for water.

The difference image in Fig. 5.16 shows the difference between the original 30-day image (Fig. 5.14) and the adjusted image (not shown). The original image is not shown in this case because there is no apparent visual difference between it and the adjusted image, as in previous cases. The difference image shows some apparent incidence angle and LTOD variations, and the variance does decrease beyond the 60% confidence interval of the original estimate (see Table 5.3). This suggests the normalization procedure is effective to some degree over 30 days, even though the decrease in variance is within the 95% confidence interval of the original estimate. The effect on variance is not as large as for the 6-day image, for unknown reasons. The larger effect on reducing variance is caused by averaging images together. Note that the variance decreases substantially between the 6-day, 30-day, and 60-day images (see Table 5.4). Also note that the difference pattern

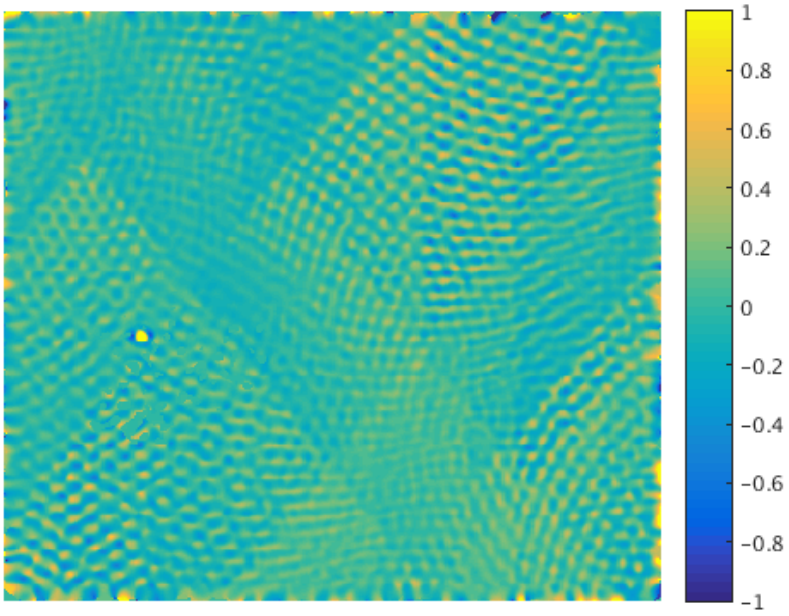

Figure 5.12: Difference of the SIR images in Figs. 5.10 and 5.5. Note that the pattern shown in this image is similar to difference images created in the simulation (see Fig. 4.33). Additionally, note that this image looks like a zoomed-in portion of Fig. 5.3, since the region is smaller than the Amazon region used above. When this pattern is shown and the variance decreases, the normalization procedure is assumed to be effective.

Table 5.3: The variance of the 30-day East Africa SIR images. Because of lower values present in water pixels, a mask is used to remove these pixels for the variance calculation (see Fig. 5.13). Note that the variance decreases beyond the 60% confidence interval after normalization.

Step	Variance	60% Confidence
Original Image	2.191	2.183–2.199
After Normalization	2.182	2.175–2.190

is harder to distinguish in a 30-day image. This is because of a greater number of overlapping measurements that are averaged together.

The difference image in Fig. 5.17 shows the difference between the original 60-day image (Fig. 5.15) and the adjusted image (not shown). Again, the original 60-day image is not shown because there is no visible difference between it and the adjusted image. The expected difference pattern is indiscernible in this case, due to significant swath overlap and pixel averaging. The

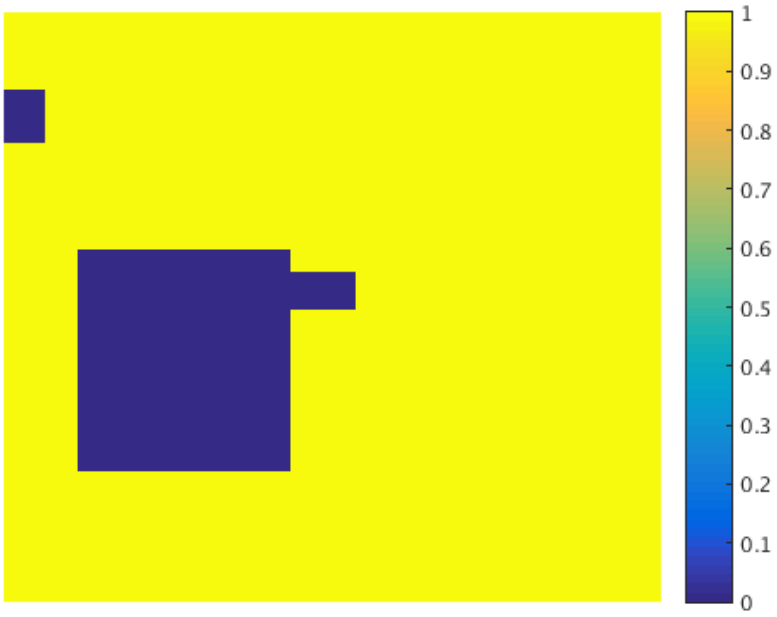

Figure 5.13: Mask for East Africa SIR images used to analyze variance. Only pixels within the light-colored regions are used in order to estimate a variance that is unaffected by Lake Victoria and other bodies of water.

Table 5.4: Variance of the normalized SIR images for the 6-day, 30-day, and 60-day images. Note that the variance decreases with more averaging.

Step	Variance
6-day Image	3.504
30-day Image	2.182
60-day Image	1.926

random regions of light and dark pixels (except over Lake Victoria) may be due to LTOD variations, which is more visible in a 60-day image normalization, due to a full 24 hours of LTOD range being measured. The dark diagonal band in the lower left corner is caused by insufficient data in one of the averaged images. The variance decreases beyond the 95% confidence interval of the original estimate for this case, and the decrease is larger than for the 6-day image or 30-day image. The results suggest that the normalization procedure is effective at reducing the total variance and that other sources of noise (beyond incidence angle and LTOD effects) dominate the image. The

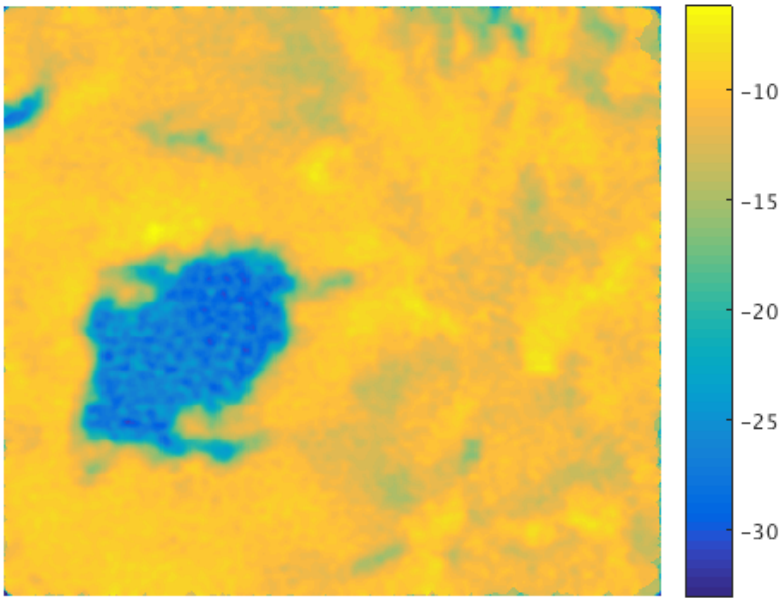

Figure 5.14: RapidScat 30-day adjusted SIR image. This image is made from 6 five-day adjusted SIR images that are averaged together. Note that the image noise is reduced because of the averaging (compare with Fig. 5.10, and see Table 5.4). The original SIR image is not shown, because the differences are not visually evident.

Table 5.5: The variance of the 60-day East Africa SIR images. Because of lower values present in water pixels, these pixels are removed by a mask for the variance calculation (see Fig. 5.13). Note that the variance decreases beyond the 95% confidence interval after the normalization procedure.

Step	Variance	95% Confidence
Original Image	1.967	1.951–1.984
After Normalization	1.926	1.910–1.942

images for 30 days and 60 days become visually more similar to QuikSCAT images, primarily due to additional averaging.

5.3 Summary

In summary, applying the normalization procedure to real RapidScat data shows a pattern of incidence angle and LTOD effects, and the variance of the pixels is reduced over pixels that do

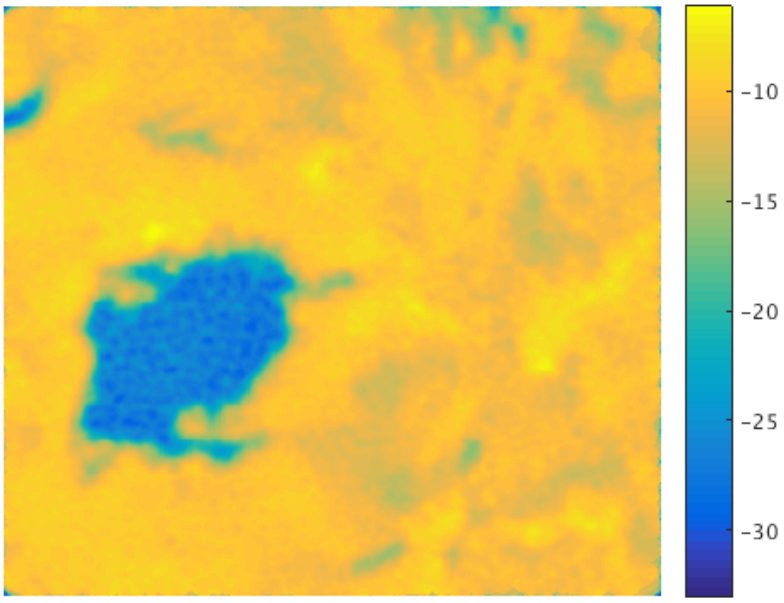

Figure 5.15: RapidScat 60-day adjusted SIR image. This image is made from 12 five-day adjusted SIR images that are averaged together. Note that the image noise is reduced because of the averaging (compare with Figs. 5.10 and 5.14, and see Table 5.4). The original SIR image is not shown, because the differences are not visually evident.

not include bodies of water. This suggests that the normalization is effective at reducing image noise by removing incidence angle and LTOD effects on σ^0.

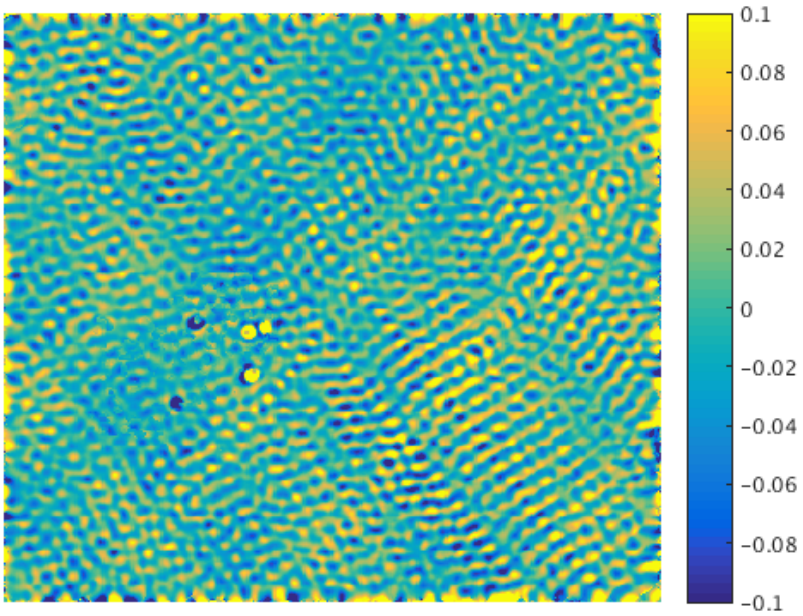

Figure 5.16: Difference of the 30-day adjusted SIR image (Fig. 5.14) and the original 30-day image (not shown). Note that a pattern is shown in this image that is similar to difference images created in the simulation (see Fig. 4.33). The differences here are smaller than for a single 6-day image. Cross-hatch and spiral patterns are evident to some degree, showing incidence angle effects, and light and dark regions suggest LTOD effects.

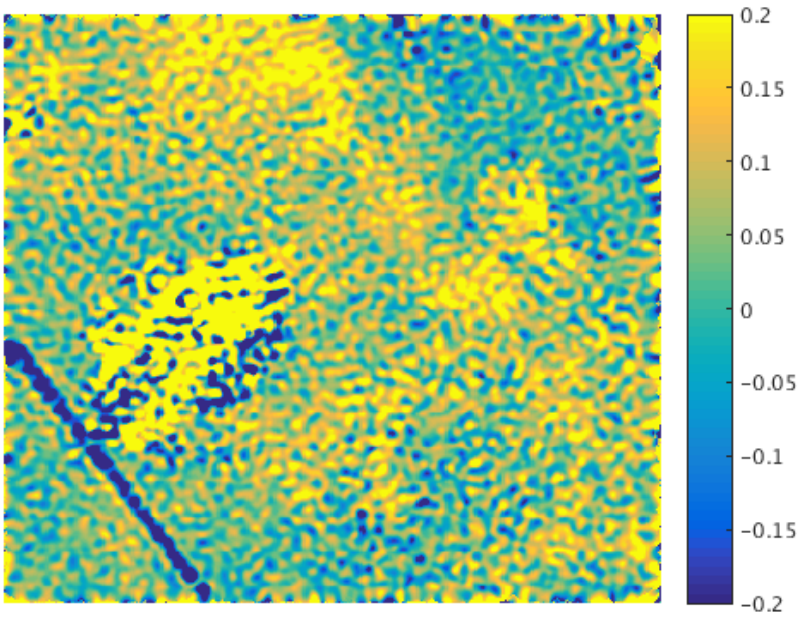

Figure 5.17: Difference of the 60-day adjusted SIR image (Fig. 5.15) and the original 60-day image (not shown). The brighter sections of the image may be due to LTOD changes that are removed. The differences here are smaller than for a single 6-day image.

CHAPTER 6. CONCLUSIONS

In this chapter, the contributions of this work are summarized and suggestions for future work are given. In this thesis, RapidScat σ^0 and attitude measurements are analyzed and adjusted to show that normalized radar images with reduced pixel variance can be created by removing σ^0 dependence on incidence angle and LTOD. Chapter 3 shows that incidence angle variation (caused by attitude changes) and LTOD variation (caused by orbital precession) are significant factors leading to variability in σ^0 measurements. Chapter 4 shows a simulation of a normalization procedure for removing σ^0 dependence on incidence angle, LTOD, and other significant parameters. Simulation results shows that overall pixel variability caused by incidence angle and LTOD can be reduced for radar images. Chapter 5 shows that the normalization procedure can be effectively applied to a standard scatterometer calibration region, such as the Amazon, where land cover is mostly homogeneous, as well as an arbitrary region that is sufficiently small to assume some level of homogeneity. The results of normalizing real data show that the effects of adjustments are relatively small compared to the noise.

6.1 Contributions

Two major contributions are made by this thesis. First, the dependence of σ^0 on various parameters is compared for RapidScat and other spaceborne Ku-band instruments. It is shown that RapidScat and TRMM data have similar models for σ^0 dependence on LTOD over the Amazon, despite functioning at different incidence angle ranges and being designed for different purposes (see Fig. 3.17). Second, a simple normalization procedure for reducing noise in SIR images is shown to be effective (see Chapters 4 and 5). This procedure reduces variability in radar image pixels caused by incidence angle and LTOD variation.

6.2 Future Work

For future work on reducing undesired pixel variability in radar images, several issues can be addressed. First, the process for RapidScat SIR creation can be automated to enable normalization for SIR images in any arbitrary location, as required. Automation requires further generalization of the code developed as part of this thesis, and it requires further integration into the SIR algorithm process. Another possible future development is to use the models in this thesis to adjust the SIR values of all Ku-band scatterometers to match a common mean, effectively normalizing SIR images for every instrument to have the same incidence angle and LTOD. Having a common mean between SIR image makes the features in the images more comparable between datasets. Additionally, a significant project that can improve the analysis of LTOD effects and errors in RapidScat's measurement geometry is to design and launch another Ku-band pencil-beam scatterometer in an equatorial orbit on a stable platform. Such a project can assist in discovering other causes of image variability in SIR images. Finally, further data analysis can be performed on current data to understand errors in RapidScat σ^0 measurements, including exploring coupled multidimensional analysis of dependence between multiple parameters and σ^0, and including analysis of log-normal noise distributions, rather than assuming normality.

REFERENCES

[1] "Scatterometer Climate Record Pathfinder," 2018. [Online]. Available: http://scp.byu.edu/gallery.html

[2] Q. P. Remund and D. G. Long, "Sea Ice Extent Mapping Using Ku Band Scatterometer Data," *Journal of Geophysical Research: Oceans*, vol. 104, no. C5, pp. 11 515–11 527, 1999. [Online]. Available: http://dx.doi.org/10.1029/98JC02373

[3] M. R. Drinkwater and D. G. Long, "Seasat, ERS-1/2 and NSCAT Scatterometer Observed Changes on the Large Ice Sheets," in *Geoscience and Remote Sensing Symposium Proceedings, 1998. IGARSS '98. 1998 IEEE International*, vol. 4, Jul 1998, pp. 2252–2254 vol.4.

[4] W. Wagner, G. Lemoine, and H. Rott, "A Method for Estimating Soil Moisture from ERS Scatterometer and Soil Data," *Remote Sensing of Environment*, vol. 70, no. 2, pp. 191 – 207, 1999. [Online]. Available: http://www.sciencedirect.com/science/article/pii/S003442579900036X

[5] D. S. Early and D. G. Long, "Image Reconstruction and Enhanced Resolution Imaging from Irregular Samples," *IEEE Transactions on Geoscience and Remote Sensing*, vol. 39, no. 2, pp. 291–302, Feb 2001.

[6] D. G. Long, "Comparison of SeaWinds Backscatter Imaging Algorithms," *IEEE Journal of Selected Topics in Applied Earth Observations and Remote Sensing*, vol. 10, no. 5, pp. 2214–2231, May 2017.

[7] "Missions: RapidScat." [Online]. Available: https://winds.jpl.nasa.gov/missions/RapidScat/

[8] N. M. Madsen and D. G. Long, "Calibration and Validation of the Rapidscat Scatterometer Using Tropical Rainforests," *IEEE Transactions on Geoscience and Remote Sensing*, vol. 54, no. 5, pp. 2846–2854, May 2016.

[9] S. L. Durden and D. Perkovic-Martin, "The RapidScat Ocean Winds Scatterometer: A Radar System Engineering Perspective," *IEEE Geoscience and Remote Sensing Magazine*, vol. 5, no. 3, pp. 36–43, Sept 2017.

[10] F. T. Ulaby, D. G. Long, W. J. Blackwell, C. Elachi, A. K. Fung, C. Ruf, K. Sarabandi, H. A. Zebker, and J. Van Zyl, *Microwave Radar and Radiometric Remote Sensing*. University of Michigan Press, 2014.

[11] J. Graf, C. Sasaki, C. Winn, W. Liu, W. Tsai, M. Freilich, and D. G. Long, "NASA Scatterometer Experiment," *Acta Astronautica*, vol. 43, no. 7, pp. 397 – 407, 1998. [Online]. Available: http://www.sciencedirect.com/science/article/pii/S009457659700180X

[12] F. T. Ulaby, R. K. Moore, and A. K. Fung, *Microwave Remote Sensing, Volume II*. Addison-Wesley Pub. Co., Advanced Book Program/World Science Division, 1982.

[13] M. Satake and H. Hanado, "Diurnal Change of Amazon Rain Forest σ^0 Observed by Ku-band Spaceborne Radar," *IEEE Transactions on Geoscience and Remote Sensing*, vol. 42, no. 6, pp. 1127–1134, June 2004.

[14] D. G. Long, P. J. Hardin, and P. T. Whiting, "Resolution Enhancement of Spaceborne Scatterometer Data," *IEEE Transactions on Geoscience and Remote Sensing*, vol. 31, no. 3, pp. 700–715, May 1993.

[15] J. C. Barrus, "Intercalibration of QuikSCAT and OSCAT Land Backscatter," Master's thesis, Brigham Young University, 2013.